Experimental and Theoretical Studies of Unstable Dynamics of Caltech's Plasma Jet: X-rays, Ultraviolet, and Visible Light

Thesis by
Yi Zhou

In Partial Fulfillment of the Requirements for the
Degree of
Doctor of Philosophy

CALIFORNIA INSTITUTE OF TECHNOLOGY
Pasadena, California

2023
Defended May 23, 2023

Yi Zhou
ORCID: 0000-0001-5315-9101

ACKNOWLEDGEMENTS

This thesis would not have been possible without the excellent mentorship of my advisor, Prof. Bellan. He introduced me to the discipline of plasma physics and has provided me with unwavering encouragement, patience, and support throughout my time at Caltech. He helped conceptualize many research ideas in this thesis. He also secured the necessary resources for the projects leading to the two publications documented in this thesis. Many chapters in this thesis are based on manuscripts carefully scrutinized by him. I would also like to express my appreciation to other members of my thesis and candidacy committees—Prof. Fultz, Prof. Troian, Prof. Hillenbrand, and Prof. Hallinan for their valuable expertise and helpful suggestions. I must also thank the generous financial support from Caltech, the Department of Energy, the Air Force Office of Scientific Research, the National Science Foundation, and the Advanced Research Projects Agency. I would like to extend my sincere thanks to X-Spectrum GmbH, Zap Energy, and LANL for collaboration opportunities.

Words cannot express my gratitude to my colleagues in the Bellan group for their substantial assistance with this work. I particularly enjoyed working with Seth Pree on imaging X-rays from the Caltech plasma jet experiment. His guidance and advice on setting up various X-ray measurements cannot be overestimated. I am grateful to my peers, Yang Zhang, André Nicolov, and Joshua Morgan, for many productive discussions. Their unique perspectives are invaluable to improving the quality of this work. I would also like to thank my past colleagues, Byonghoon Seo, Magnus Haw, Ryan Marshall, Young Dae Yoon, Pakorn Wongwaitayakornkul, and Dave Felt, for their patient efforts in teaching me various skills and knowledge that are critical for carrying out my research. They answered my questions and concerns as a beginning graduate student thoughtfully and gave constrictive critiques to help me improve. I would like to acknowledge the administrative assistance of Connie Rodriguez, Jennifer Blankenship, Kevin Cooper, and Christine Jenstad. Their work has allowed me to focus on my research.

I gratefully acknowledge the entertainment and emotional support from many community members of Caltech and my friends. Lastly, I am extremely grateful to my parents for their unconditional love and firm belief in my abilities.

ABSTRACT

The Caltech plasma jet experiment launches a laboratory plasma jet that is analogous to an astrophysical jet. Even though the temperature of the plasma jet is around 2 eV, 6 keV X-rays and 20–60 eV extreme ultraviolet (EUV) radiation were detected when the plasma jet was perturbed by magnetohydrodynamic instabilities. How charged particles in a plasma are accelerated to suprathermal energy has been a key question in plasma physics, solar physics, and astrophysics. Studying these surprisingly energetic radiations from Caltech's plasma jet can help answer this question. Toward this goal, this thesis contains an experimental study of the X-rays and a theoretical study of the EUV radiation.

In the experimental study, a PIN-diode-based 1D X-ray camera has been developed to spatially, temporally, and spectrally resolve the transient, low-intensity, and suprathermal X-rays detected to be simultaneous with magnetohydrodynamic instabilities that disrupt the plasma jet. This X-ray camera has high detection efficiency over the 5–10 keV X-ray band, an over 20-degree field of view (FOV), and the capability to produce more than 50 time-resolved frames with a submicrosecond time resolution. The X-ray images are formed by a pinhole or by a coded aperture placed outside the vacuum chamber in which the plasma jet is launched. The 1D imaging shows that the location of the X-ray source is either a few centimeters away from an inner disk electrode or near a spatially translatable metal frame that is 30–40 cm away from the electrode.

In the theoretical study, we propose a collisional two-fluid model which involves a novel two-stream instability that is indifferent to collisions, even though collisions have been traditionally presumed to damp the two-stream instability. This model is used to explain previously observed localized dimming of visible light and a simultaneous, localized burst of EUV radiation from a plasma jet the cross section of which is constricted by a kink-instigated Rayleigh-Taylor instability. On being triggered by the constriction of the plasma cross section, the proposed two-stream instability produces a region of low density where an electric double layer leads to localized electron heating. The low-density region is consistent with and so likely explains the visible light dimming, and the localized electron heating is consistent with and likely explains the EUV radiation. The numerical solution of the collisional two-fluid model demonstrates good agreement with the apparent electron velocity and density profiles in the plasma jet.

PUBLISHED CONTENT AND CONTRIBUTIONS

[1] Y. Zhou and P. M. Bellan. "Two-stream instability with a growth rate insensitive to collisions in a dissipative plasma jet". In: *Physics of Plasmas* 30 (2023), p. 052101. DOI: 10.1063/5.0146806.
Y. Zhou developed the plasma physics model presented in the paper, performed analytical analysis on the model, solved the model numerically, reviewed the relevant literature, and wrote the manuscript.

[2] Y. Zhou, S. Pree, and P. M. Bellan. "Imaging suprathermal x-rays from a laboratory plasma jet using PIN-diode-based and scintillator-based 1D pinhole/coded aperture cameras". In: *Review of Scientific Instruments* 94 (2023), p. 013504. DOI: 10.1063/5.0122760.
Y. Zhou participated in the conception of the project, designed, developed, and assembled the PIN-diode-based X-ray camera, tested and calibrated the camera, collected the majority of the X-ray image data, analyzed and visualized the X-ray image data, and wrote the manuscript.

[3] M. J. Falato et al. "Plasma image classification using cosine similarity constrained convolutional neural network". In: *Journal of Plasma Physics* 88 (2022), p. 895880603. DOI: 10.1017/S0022377822000940.
Y. Zhou contributed image data to the total data set, helped develop a program to render grayscale images in false color, advised on how to label the image data for supervised learning, and reviewed the manuscript.

[4] C. Noel et al. "Electric-field noise from thermally activated fluctuators in a surface ion trap". In: *Physical Review A* 99 (2019), p. 063427. DOI: 10.1103/PhysRevA.99.063427.
Y. Zhou programmed the FPGA of the digital-to-analog converter to create potential wells for trapping ions, participated in collecting the experimental data, and reviewed the manuscript.

TABLE OF CONTENTS

LIST OF ILLUSTRATIONS

LIST OF TABLES

Chapter 1

INTRODUCTION

1.1 Background

Plasmas are high-temperature ionized gases. Examples of plasmas include lightning, aurora, Earth's ionosphere, solar wind, and fluorescent lights. A plasma consists of positively charged ions and negatively charged electrons. These charged particles can interact with each other via long-range electromagnetic forces. A plasma can also interact with external electromagnetic fields.

Under the effects of these electromagnetic interactions, plasmas can exhibit many unique and interesting dynamics that regular gases do not exhibit. For example, the Coulomb attraction between ions and electrons can act as a restoring force to cause electrons to oscillate around their equilibrium positions. When a voltage drop is applied across a plasma by a power supply, electrons and ions will be accelerated in opposite directions, and the relative motion between electrons and ions forms a current. Such a current-carrying plasma can create a magnetic field according to the right hand rule, and the magnetic field can cause the current channel of the plasma to kink and coil up (see Figure 1.1).

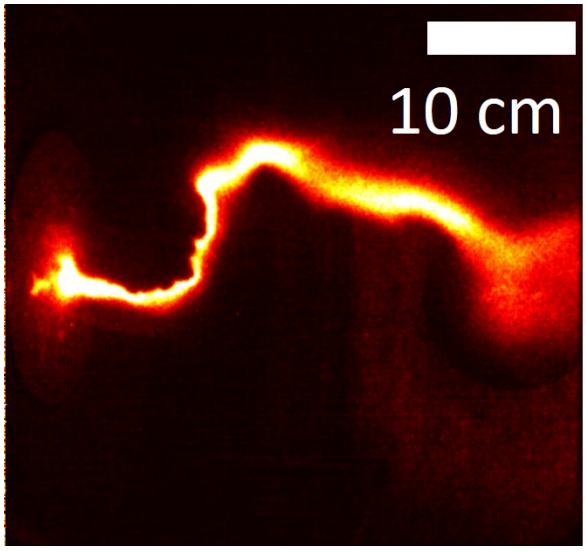

Figure 1.1: A kinked current-carrying plasma jet created in the Caltech experiment. False color is applied to this image.

The dynamics of a plasma can be modeled accurately by simultaneously tracking the trajectory of every particle and accounting for the contribution of every particle the electromagnetic fields. However, this approach is impractical to because the number of particles in a plasma is on the order of Avogadro's number.

A more practical approach is to model the collective interaction between a large number of particles and the electromagnetic fields. Over the past 100 years, plasma physicists have developed three primary theoretical models of this kind: the Vlasov model, the two-fluid model, and the magnetohydrodynamics (MHD) model. Key equations of these models are listed in Appendix A of this thesis for reference.

The Vlasov model [1] has the most detailed and complex description of the three models. This model characterizes all particles within a small phase space volume near a location $\mathbf{x}$ and a velocity $\mathbf{v}$ at a given time t with a distribution function $f(\mathbf{x}, \mathbf{v}, t)$. The time evolution of this distribution function is described by the Vlasov equation. The Vlasov model is best at describing the damping or growth of small perturbations to a plasma [2, 3].

The two-fluid model breaks a plasma into an electron fluid and an ion fluid. The time evolution of the densities, velocities, and energies of these fluids is described by hydrodynamic-like equations. Compared to the Vlasov model, the two-fluid model is considerably easier to analyze and understand because the two-fluid model is based on quantities in real space instead of phase space. The elegant Clemmow-Mullaly-Allis (CMA) description of plasma waves is based on this model [4].

Of the three models, the MHD model has the simplest but coarsest description. This model describes the plasma as one current-carrying fluid that is charge-neutral. The time evolution of this fluid is also described by hydrodynamic-like equations. The MHD model excels at efficiently describing the macroscopic dynamics of a plasma in a complex 3D geometry, where it is difficult to use the Vlasov model or the two-fluid model. The MHD model is prevalently used to model large-scale dynamics of solar and astrophysical plasmas and is highly relevant for the magnetic confinement of fusion plasmas. Important results based on this model include the discoveries of Alfvén waves [5] and the Woltjer-Taylor relaxation principle that plasmas relax to a minimum energy state while preserving the twistiness of magnetic field topology [6, 7].

Understanding plasma dynamics is important for solving many unsolved physics problems. Examples of these unsolved problems include the powering mechanism

of an astrophysical jet, the generation of the Sun's magnetic field, and the heating of the solar corona. Studying plasma dynamics also has many practical applications such as the field confinement of fusion plasmas, the fabrication of semiconductor devices, the design of high-performance particle accelerators, the production of high-intensity pulses of radiation, and the propulsion of spacecraft.

1.2 Overview of the Thesis

This thesis mainly investigates previously unresolved issues related to the unstable dynamics of plasmas created in the Caltech plasma jet experiment. The plasma jet experiment was originally designed to study the Woltjer-Taylor relaxation principle that can lead to formation of a spheromak [8, 9]. It was later identified that the experiment could also be used to study dynamics related to astrophysical jets due to the scalability of MHD [10, 11, 12, 13]. Chapter 2 of this thesis gives an overview of the experiment, describes the experimental apparatus and available plasma diagnostics, and discusses some photos that clearly show the unstable dynamics of interest.

These unstable dynamics manifest themselves as exponential growth of small perturbations to the plasma jet because the perturbations tend to drive the plasma jet into a lower energy state. Previous studies have identified that the the initial phases of these dynamics agree with the MHD theory [14, 15, 16]. When the perturbations have grown to large amplitudes in later phases, the plasma current channel is quickly (< 1 μs) constricted to a very small radius (from several centimeters to less than 1 centimeter) and eventually breaks apart (see Figures 2.19 , 2.20, and 5.1). Non-MHD processes contained in the microscopically-oriented Vlasov and two-fluid models are believed to be important for dynamics at the constricted region [10, 17]. During the 1 μs of constriction and breaking apart, energetic events such as 20–60-eV extreme ultraviolet (EUV) and 6 keV X-ray bursts, ion heating, electron heating, and whistler wave emission have been observed [16, 18, 19, 20].

The first unresolved issue is related to the 6 keV X-rays. Because the temperature of the plasma in the Caltech experiment is only around 2 eV, the X-ray energy is 3 orders of magnitude higher than the average kinetic energy of an particle. Similarly energetic X-rays have also been observed in many other plasmas, both in nature and in laboratory [21, 22, 23]. How charged particles in a plasma can be accelerated to such high energy to emit energetic X-rays has been an open question under active research. To understand the acceleration process in the Caltech plasma jet, a novel

coded aperture X-ray camera has been designed to track the locations and trajectories of energetic charged particles. Chapter 3 of this thesis describes the design of the X-ray camera. Chapter 4 illustrates how the X-ray camera was utilized to identify the locations of X-ray sources and to measure the X-ray energy. Although one would naturally expect that the X-rays were emitted from the constricted region of the plasma, the X-ray images show that these X-rays were primarily produced near two metal objects that are on opposite ends of the plasma jet. This new information suggests that charged particles inside the plasma are accelerated in two opposite directions.

The second unresolved issue is related to the 20–60 eV EUV radiation. A previous study [19] has identified that the EUV radiation was emitted from the constricted region of the plasma jet. In addition, the constricted region was simultaneously observed to become dim in visible light. It has been unclear why the EUV brightening and the visible light dimming should occur. Chapter 5 of this thesis presents a plasma physics model that is consistent with the EUV brightening and visible light dimming. This model extends a fundamental collisionless plasma behavior known as the two-stream (Buneman) instability [3, 24, 25] to a high-collision regime. This instability can cause current dissipation, excite plasma waves, evacuate or bunch up charged particles, and create large and localized electric fields. Previous studies on this instability have argued that collisions in a plasma suppress the instability [26, 27, 28, 29, 30, 31]. Our plasma physics model, on the other hand, shows that a specific mode of the two-stream instability is indifferent to collisions. This indifference to collisions enables the instability to grow in an extremely collisional plasma, such as the Caltech plasma jet.

Two appendices have been included. Appendix A provides a list of key equations for modeling plasma dynamics. This appendix is particularly relevant for the discussion regarding the two-fluid equations in Chapter 5. Appendix B reviews the relevant semiconductor physics for understanding the amplifier circuit of the X-ray camera described in Chapter 3. This appendix also describes the amplifier circuit in more detail so that readers who are interested can reproduce and improve the circuit.

Chapter 2

CALTECH PLASMA JET EXPERIMENT

2.1 Overview of the Experiment

The Caltech plasma jet experiment uses pulsed power technology to generate a plasma jet driven by magnetohydrodynamic (MHD) forces. The plasma jet is created inside the large cylindrical vacuum chamber shown in Figure 2.1. The length of this chamber is 2 m, and the diameter of this chamber is 1.5 m.

The plasma jet generated in this experiment lengthens from several centimeters to tens of centimeters in 20–30 μs. Smaller scale (∼ 1cm) features such as ripples due to Rayleigh-Taylor instability can also be observed. Some characteristic parameters of this plasma jet are summarized in Table 2.1. The parameters in this table are mostly based on experimental measurements: The electron density of this plasma is determined from a plasma-induced phase shift measured by a heterodyne interferometer [32, 33]. The interferometer measurements are consistent with density measurements obtained from Stark broadening of spectral lines [19, 34]. The plasma jet is assumed to be quasi-neutral, so the ion density is roughly the same as the electron density. The ∼ 3 eV electron temperature is determined from relative spectral line intensities [34]. This electron temperature can increase to ∼ 10 eV in the region where the cross section of the plasma jet is constricted [19]. The ion temperature is determined from Doppler broadening of spectral lines [16, 19]. The

Table 2.1: Characteristic plasma parameters for Caltech's argon plasma jet. How these parameters are determined are explained in detail in section 2.1

Parameter	Symbol	Value
Electron density	n_e	10^{21}–10^{22} m^{-3}
Ion density	n_e	10^{21}–10^{22} m^{-3}
Electron temperature	T_e	∼ 3 eV – 10 eV
Ion temperature	T_i	∼3–17 eV
Magnetic field strength	$\|B\|$	∼ 0.1–1 T
Plasma beta	β	∼ 0.016–1.6
Electron/ion mass ratio	m_e/m_i	1.4×10^{-5}
Electron-ion collision frequency	ν_{ei}	$\sim 1 \times 10^{11}$ s^{-1}
Electron plasma frequency	ω_{pe}	$\sim 6 \times 10^{12}$ s^{-1}
Ion plasma frequency	ω_{pi}	$\sim 2 \times 10^{10}$ s^{-1}

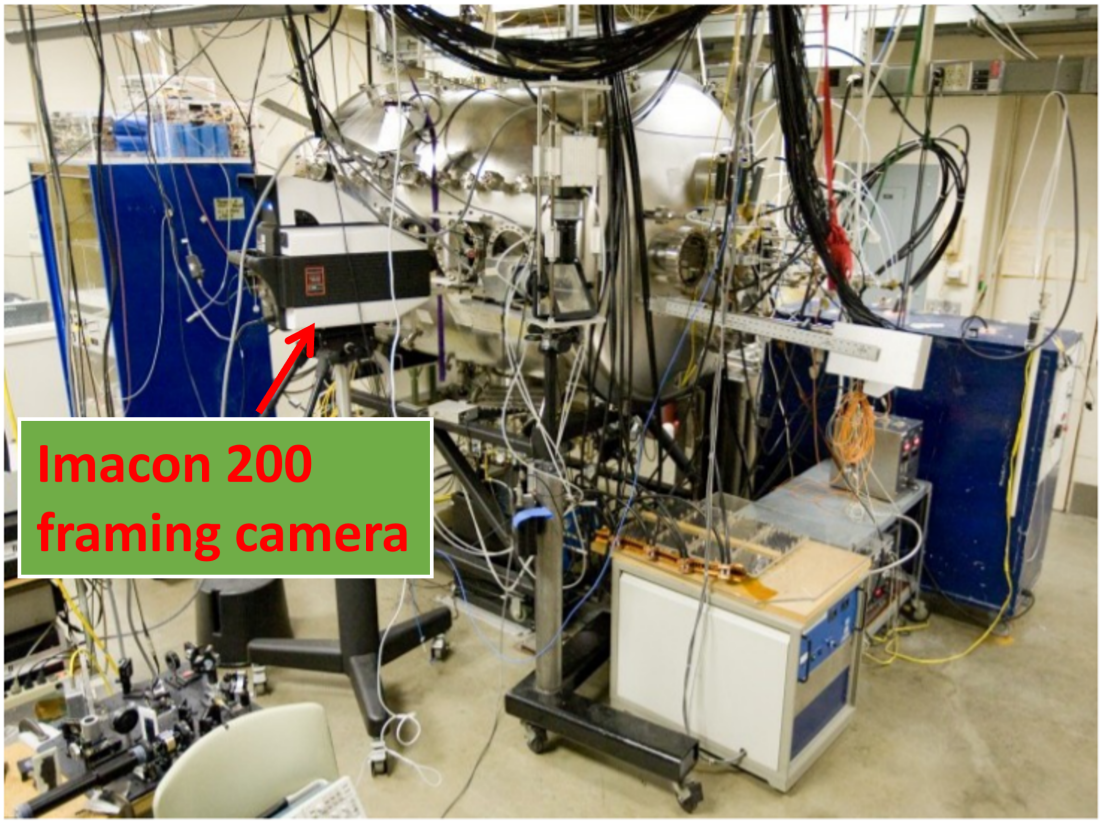

Figure 2.1: Photo of the Caltech plasma jet experiment. The length of the vacuum chamber in the photo is 2 m, and the diameter is 1.5 m. The camera (DRS HADLAND Imacon 200) shown in the photo is a powerful fast framing camera that can take 14 frames of grayscale images per plasma shot.

ion temperature can be as hot as ~ 17 eV due to changes in magnetic field topology converting magnetic energy to kinetic energy of ions (magnetic reconnection) [16, 19]. The magnetic field can be measured by a magnetic probe array [35]. The magnetic field is strong near the axis of the plasma jet and weak away from the axis of the plasma jet. An order of magnitude calculation for the magnetic field near the axis of the plasma jet can be done using

$$|B| = \mu_0 I / 2\pi r, \tag{2.1}$$

where $I \approx 70$ kA is the current carried by the plasma jet and $r \approx 2$ cm is the radius of the plasma jet. The result of this calculation is $|B| \approx 0.7$ T. The plasma beta is defined as the ratio of the thermal pressure to the magnetic pressure. Assuming the electron density and the ion density are the same, the plasma beta can be calculated with

$$\beta = 2\mu_0 n_e \kappa (T_e + T_i) / B^2. \tag{2.2}$$

Using $n_e \approx 10^{22}$ m^{-3}, $T_e \approx T_i \approx 2$ eV$\approx 2.3 \times 10^4$ K, $B \approx 0.1$–1 T, we get a plasma beta that ranges from 0.016 to 1.6. The electron/ion mass ratio is calculated using the atomic mass of an argon atom. The electron-ion collision frequency is calculated using the formula

$$\nu_{ei} = \frac{e^{5/2}}{2 \times 3^{3/2} \pi \varepsilon_0^2 m_e^{1/2}} \frac{n_i \ln \Lambda}{T_e^{3/2}}, \tag{2.3}$$

where T_e is in units of electron volts and $\ln \Lambda$ is the Coulomb logarithm. With $n_i \approx 10^{22}$m^{-3}, $\ln \Lambda \approx 10$, and $T_e \approx 2$ eV, we get a collision frequency on the order of 10^{11} s^{-1}. The electron or ion plasma frequency is calculated using

$$\omega_{p\sigma} = \sqrt{\frac{n_\sigma e^2}{\varepsilon_0 m_\sigma}}, \tag{2.4}$$

where $\sigma = i$ or e denotes the particle species and $n_\sigma = 10^{22}$ m^{-3} is used.

An astrophysical jet is an energetic, continuous, collimated outflow of plasmas commonly observed to emanate from a massive central body surrounded by an accretion disk [36]. The massive central body could be a young stellar object, an active galactic nuclei, or a compact star, As shown in Figure 2.2, the combination of the collimated plasma jet and the planar electrode setup in the experiment is analogous to an astrophysical jet launched from an accretion disk.

It is generally accepted that the MHD equations describe the dynamics of these astrophysical jets [37, 38, 39]. However, because diagnostics of these astrophysical jets are limited, many aspects of these jets are poorly understood. Fortunately, the macroscopic behaviors of the well-diagnosed plasma jet in the Caltech experiment is also governed by the MHD equations [40]. Because both the laboratory plasma jet and the astrophysical jet can be described by the MHD equations, observations made in the Caltech experiment can be readily related to astrophysical jets following the MHD scaling relations [10, 11, 12, 13]. This scaling argument allows us to gain many useful insights on an astrophysical jet by studying the laboratory plasma jet.

Through twenty years of research, a great deal of discoveries regarding many aspects of this laboratory plasma jet have been achieved. These discoveries include the collimation of the plasma flux tube [41], flow of the plasma jet [42], instabilities the plasma jet experiences [14, 15, 16], magnetic field fluctuations [20], and high-energy radiation [19, 18, 43] . A good summary of most of these discoveries is given by Bellan [11].

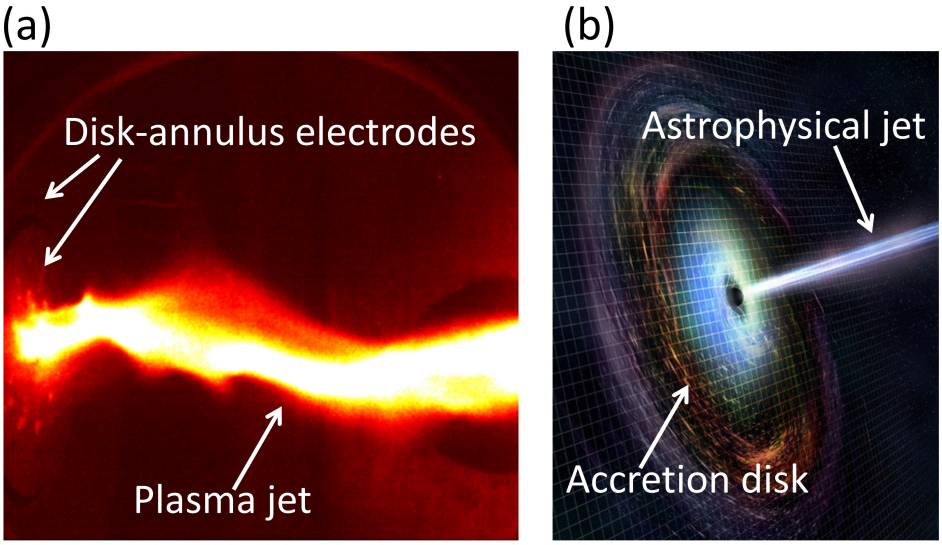

Figure 2.2: (a) shows a false color image of a collimated plasma jet launched from disk-annulus electrodes in the Caltech experiment. (b) shows an artist's impression of an astrophysical jet emanating from the center of a accretion disk (image credit: NASA/CXC/M.Weiss). The macroscopic behaviors of both the laboratory plasma jet and the astrophysical jet can be described by MHD equations because MHD equations do not have an intrinsic scale. Therefore, many observations in the experiment can be scaled to astrophysical situations.

2.2 Experimental Apparatus

This section describes the hardware for the plasma jet experiment.

Coaxial Electrodes

The plasma jet is launched from a pair of coplanar and concentric disk-annulus copper electrodes shown in Figure 2.3. The diameter of the inner disk electrode is roughly 20 cm, and the outer diameter of the annulus electrode is around 50 cm. The inner disk electrode and the annulus electrode are separated by a 6 mm gap so that the two electrodes can be at different electrostatic potentials. The annulus electrode is grounded, and the inner disk electrode is connected to capacitor banks that are typically charged to -5 kV. The large voltage difference between these two electrodes breaks neutral gas down into a plasma.

Timing System

To create the plasma jet, a timing system is programmed to generate optical pulses to sequentially initiate the high-voltage power supplies for a magnetic flux system, a gas injection system, and a plasma breakdown system. The use of optical pulses

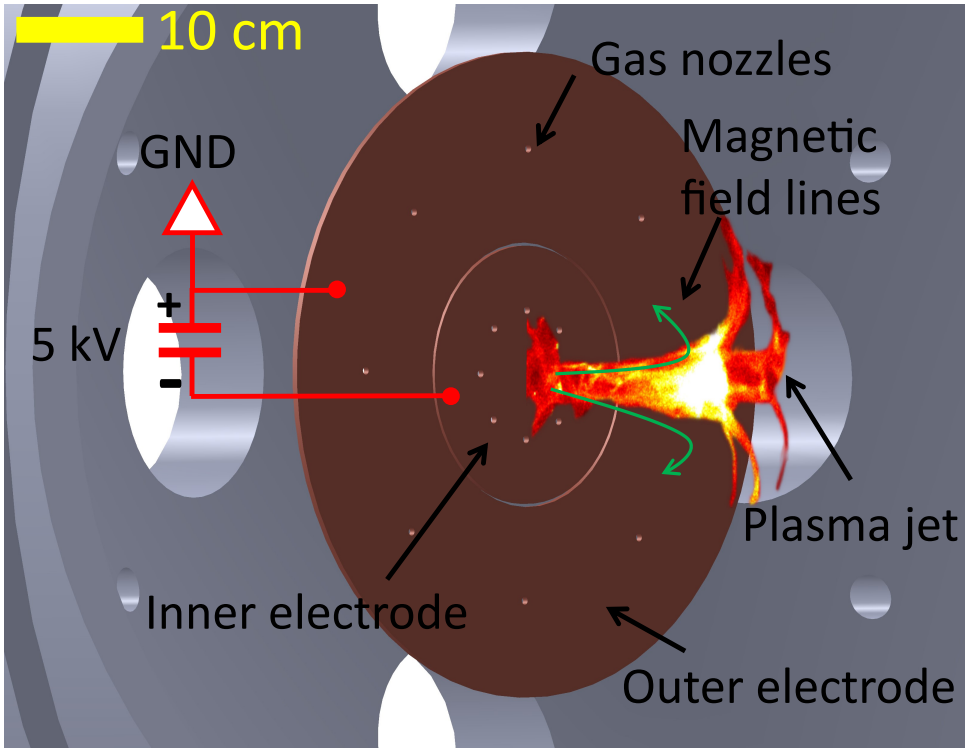

Figure 2.3: Setup of the Caltech plasma jet experiment with a photo of a collimated plasma jet superimposed. A pair of coplanar, concentric electrodes inside a large vacuum chamber launch the collimated plasma jet shown in the photo. The green magnetic field lines are created by a coil located behind the inner electrode. Neutral gas puffs are injected through eight pairs of gas nozzles evenly spaced on the electrodes, and then a capacitor bank charged to -5 kV is switched across the inner and outer electrodes to break down the neutral gas. Initially, eight plasma arches that follow the magnetic field lines form. These eight arches then merge into the collimated plasma jet shown in the photo.

avoids having ground loops. Figure 2.4 illustrates various components of this timing system. To initiate the plasma creation sequence, the red button on the pulser is pressed to deliver a pulse to trigger an 8-channel timing generator (Berkeley Nucleonics, Model 565). Different channels on this timing generator then generate several voltage pulses independently. The time intervals between these voltage pulses are set by a LabView program. These voltage pulses are delivered to a electro-optical pulse doubler (developed by Dave Felt) and converted to optical pulses. These optical pulses then activate various high-voltage power supplies to create the plasma jet.

Let $t = 0$ be the time the power supply for the plasma breakdown system is activated.

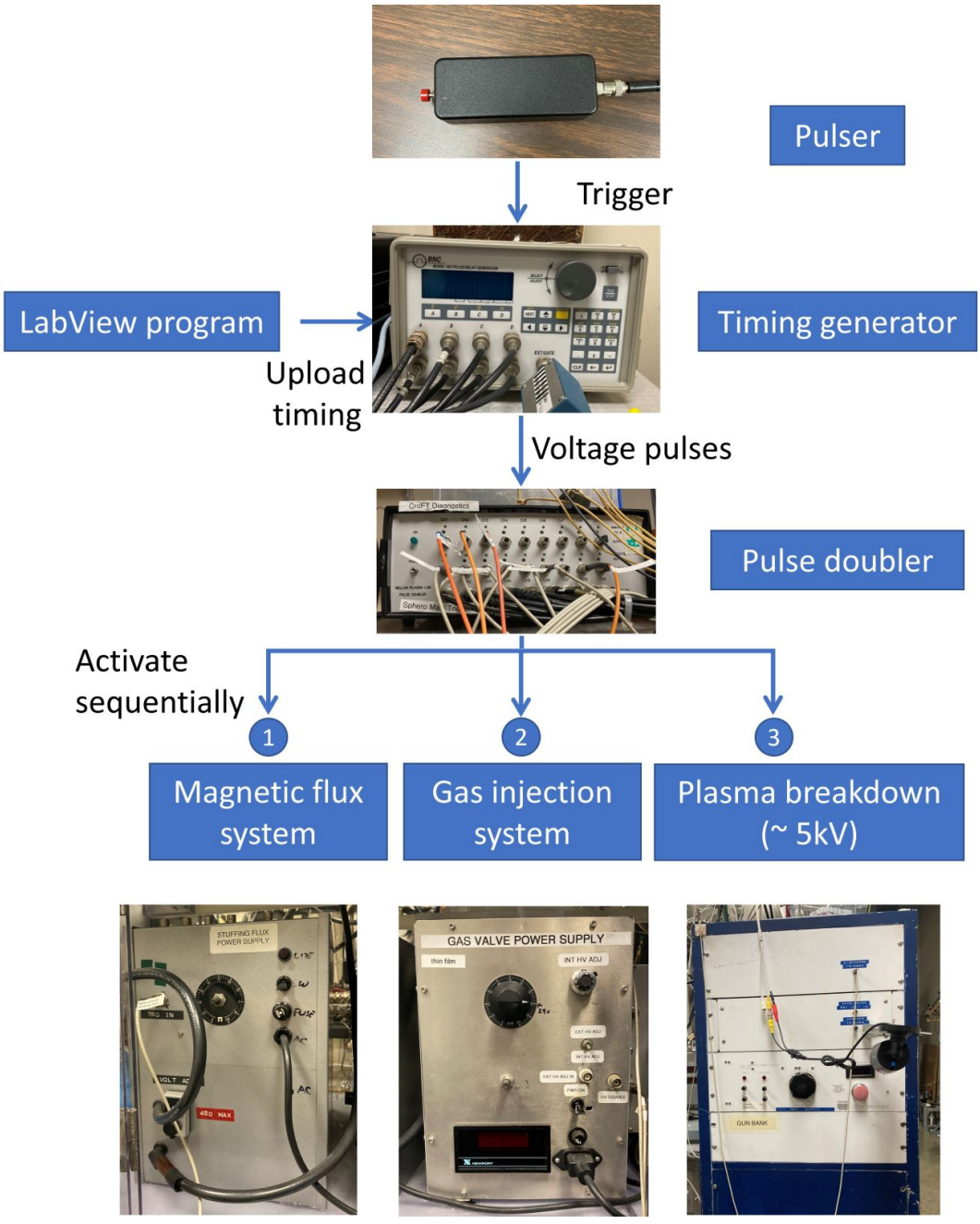

Figure 2.4: The timing generator generates several voltage pulses upon receiving a trigger signal from the pulser. The timing of these voltage pulses are set by a LabView program. Voltage pulses from the timing generator are converted to optical pulses by the pulse doubler. These optical pulses then sequentially activate the power supplies, shown in the bottom three photos, for a magnetic flux system, a gas injection system, and a plasma breakdown system.

Typically, the magnetic flux system is activated at $t = -10$ ms, and the gas injection system is activated between $t = -5$ ms and $t = -1$ ms depending on the mass of gas being injected. It is important to activate the magnetic flux system and the gas injection system several milliseconds before the plasma breakdown system to ensure the magnetic flux and the neutral gas density in front of the electrodes are near maximum when plasma breakdown occurs.

Many plasma diagnostics, such as the fast framing camera shown in Figure 2.1, are also triggered, upon plasma breakdown, by this timing system in a similar way. The only difference is that initial pulse that triggers the timing generator is provided by the strong light emission simultaneous with the plasma breakdown. This optical trigger method is necessary for synchronizing the plasma diagnostics with the plasma breakdown because the time of plasma breakdown jitters from shot to shot.

Magnetic Flux System

The power supply for the magnetic flux system is a capacitor bank typically charged to 20–200 V. The discharge of this capacitor bank drives a transient current through a magnetic field coil coaxial with and located immediately behind the inner disk electrode. This coil generates dipole-like background magnetic field lines that thread the inner disk electrode as shown in Figure 2.3. (In an accretion disk-astrophysical jet system, poloidal magnetic field lines threading the center of the accretion disk also exist [37].) The current through the magnetic coil varies on a time scale of milliseconds, so the magnetic field generated by the coil is essentially constant over the duration of the plasma jet (tens of microseconds). The magnetic flux through the inner electrode increases linearly with the power supply voltage V_{bias}. This linear relationship is given by [44]

$$\psi \approx 0.01 V_{\text{bias}} \quad \frac{\text{mWb}}{\text{Volt}}. \tag{2.5}$$

Previously, Hsu and Bellan [14] have identified that varying the background magnetic flux generated by the system while keeping other experimental parameters the same can generate three distinct plasma configurations: (I) "stable column," (II) "kinked column," and (III) "detached plasma." Photos of the these three distinct plasma configurations can be found in Figure 3 of Hsu and Bellan [14]. The focus of this thesis is on two plasma configurations that are similar but not identical to the "detached plasma" configuration and the "kinked column" configuration. The two plasma configurations that are studied in this thesis are named as the low-flux (LF) configuration and the high-flux (HF) configuration based on the amount of

background magnetic flux generated by the magnetic coil. Photos of these two plasma configurations will be shown and described in detail in Section 2.4.

Gas Injection System

The gas injection system is designed to inject a small amount of neutral gas puffs through 16 gas nozzles evenly spaced on the disk-annulus electrodes right before plasma breakdown (see Figure 2.1). In situ fast ion gauge measurements indicate that the density of the neutral gas injected by this system is on the order of 10^{19} m^{-3} [44]. This density is about 2 to 3 orders of magnitude lower than the peak plasma particle density inferred from spectroscopic measurements [41, 34] and interferometric measurements [33, 32]. Therefore, additional particles must have been injected from the gas nozzles into the plasma by MHD forces [41]. The diagram in Figure 2.5 illustrates how different components of the gas injection system are connected. The system mainly consists of 6 compressed gas cylinders connected to 4 fast gas valves via two independent gas lines, labeled as "Gas A" and "Gas B" in Figure 2.5. The gas pressure in these two lines is typically regulated to 70 psi. The gas species that feeds each of these two lines can be selected via a six-way valve shown in Figure 2.6. In the experiments discussed in this thesis, argon gas is selected to feed both the gas A and gas B lines. This selection makes a pure argon plasma jet.

Each of the 4 fast gas valves is connected to 4 gas nozzles and can be set to inject either gas A or gas B through these gas nozzles. Depending on the locations of the gas nozzles that are connected to the fast gas valves, the 4 fast gas valves are labeled as outer left (OL), inner left (IL), inner right (IR), and outer right (OR). For example, the OL fast gas valve is connected to the 4 gas nozzles on the left half plane of the outer annulus electrode. The OL and OR fast gas valves share one power supply, and the IL and IR fast gas valves share another power supply. Each power supply drives a current pulse through a magnetic coil inside a fast gas valve, and the magnetic force generated by the coil opens the valve transiently to inject pressurized gas into the vacuum chamber. The amount of gas injected can be controlled by voltages (typically > 400 V) on the power supplies.

Plasma Breakdown System

The plasma breakdown system consists of a 120 μF high-voltage capacitor bank connected across the inner and outer electrodes. Detailed electrical characterization of this discharge system can be found in Deepak Kumar's thesis [45]. This capacitor

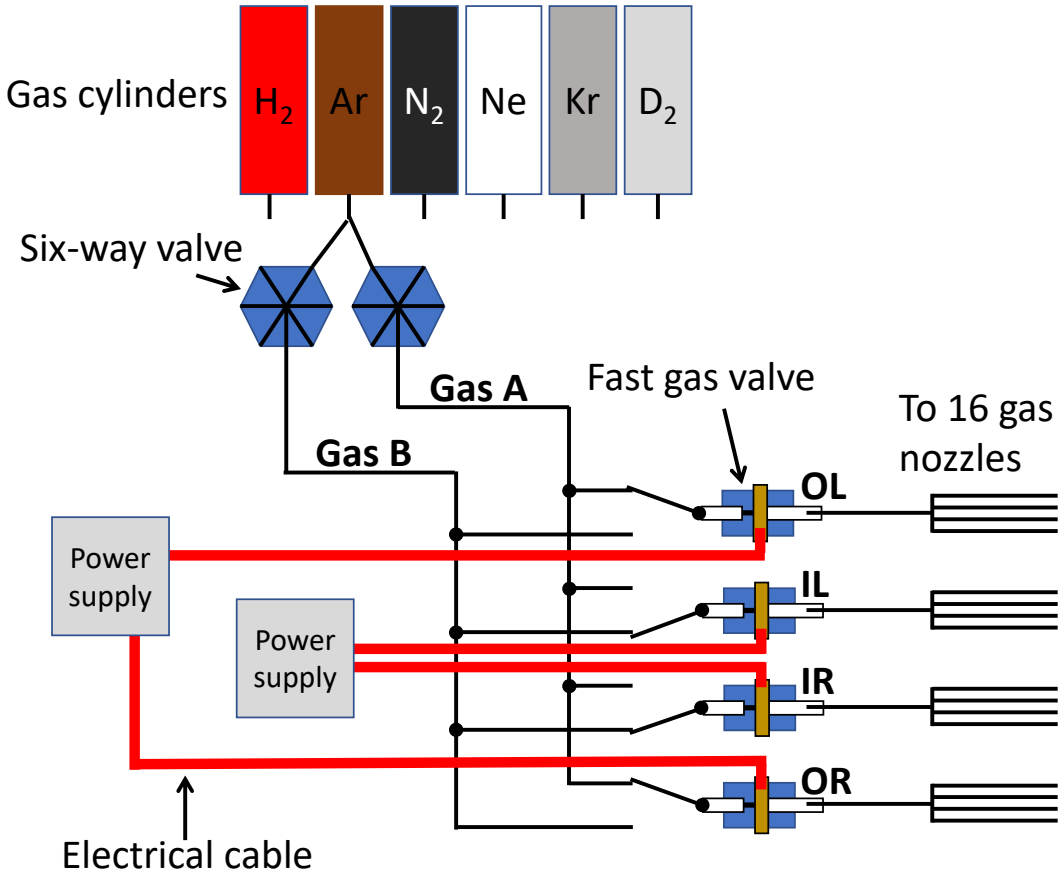

Figure 2.5: This diagram illustrates how six compressed gas cylinders are connected to gas nozzles via two independent gas lines labeled as "Gas A" and "Gas B." The gas that feeds each gas line is selected via a six-way valve, and the gas line pressure is typically regulated to $\sim$ 70 psi. The two gas lines are connected to four fast gas valves that control the amount of gas injected into the vacuum chamber. The four fast gas valves are labeled as outer left (OL), inner left (IL), inner right (IR), and outer right (OR), depending on the locations of the four gas nozzles that are connected to each fast gas valve. For example, the IR fast gas valve is connected to four gas nozzles on the right half plane of the inner disk electrode. The opening of these fast gas valves is controlled by $>$ 400 V pulsed power supplies.

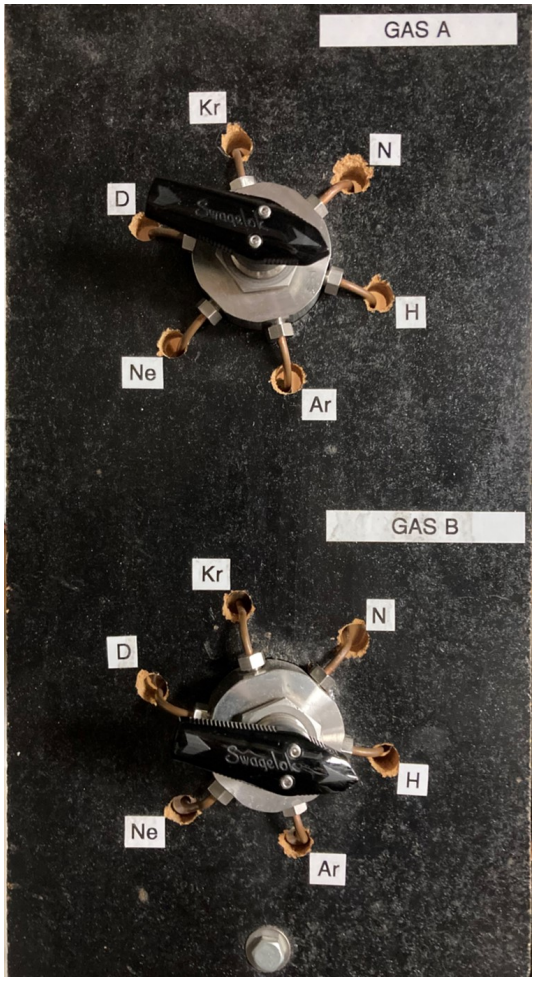

Figure 2.6: Two six-way valves that select gas species feeding the gas A and gas B lines.

bank is typically charged to -5 kV by a capacitor charging power supply (Maxwell General Atomics CCDS 310-P-1-208). Upon receiving a trigger signal, the charged capacitor bank is switched by an ignitron and applies the -5 kV voltage drop across the electrodes to break the injected neutral gas puffs into plasma. The breakdown voltage satisfies a condition known as the Paschen's law, which describes the voltage required for plasma breakdown as a function of gas pressure p times discharge path length d. In addition to breaking down the neutral gas into plasma, the high-voltage capacitor bank also continues to drive a pulsed current (see orange curve in Figure 2.8) through the plasma to sustain the plasma jet for 10–20 μs.

Figure 2.7: The pulse-forming network designed to extend the duration of the plasma jet.

Pulse-Forming Network

A pulse-forming network (PFN) can be used to drive a longer duration current through the plasma jet to extend its life time from 10–20 μs to 40–50 μs. This PFN consists of a set of capacitors and inductors connected in a transimission line topology. Figure 2.7 shows a photo of the PFN machine. The capacitor bank inside the PFN machine, typically charged to -5 kV, is triggered to discharge right after plasma breakdown. After the PFN machine is fired, the significant increase in current duration can be seen in Figure 2.8. Details about the design, construction, and testing of the PFN are documented in Auna Moser's thesis [44].

Vacuum Pumps

Figure 2.9 shows the vacuum pumps used to pump down the large vacuum chamber. The dry scroll pump (Edwards nXDS15i) is used as a roughing pump to decrease the pressure inside the large vacuum chamber to $\sim 1 \times 10^{-2}$ torr. Then a cryopump (Marathon CP-12) further lowers the pressure to $< 1 \times 10^{-6}$ torr. This cryopump creates vacuum by solidifying gases onto cryopanels that are cooled by a helium

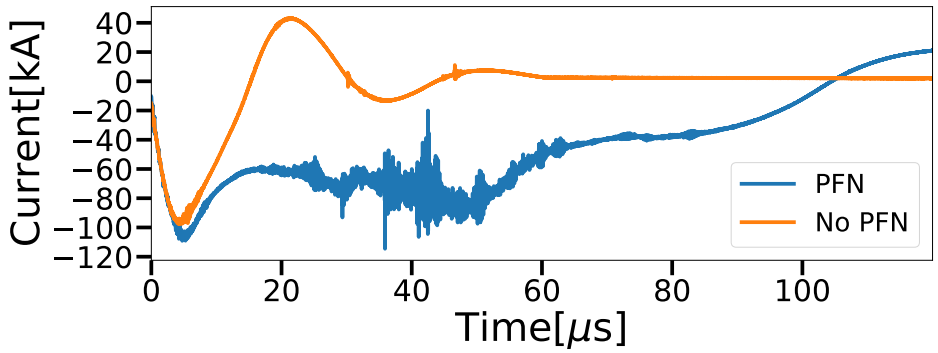

Figure 2.8: Curves that show the currents flowing through the plasma jet experiment. These currents are measured by a Rogowski coil coaxial with the inner electrode. The orange curve represents a current pulse driven by the high-voltage capacitor bank of the plasma breakdown system. The duration of this pulsed current is < 20 µs. The blue curve represents a current pulse further sustained by a pulse-forming network (PFN).

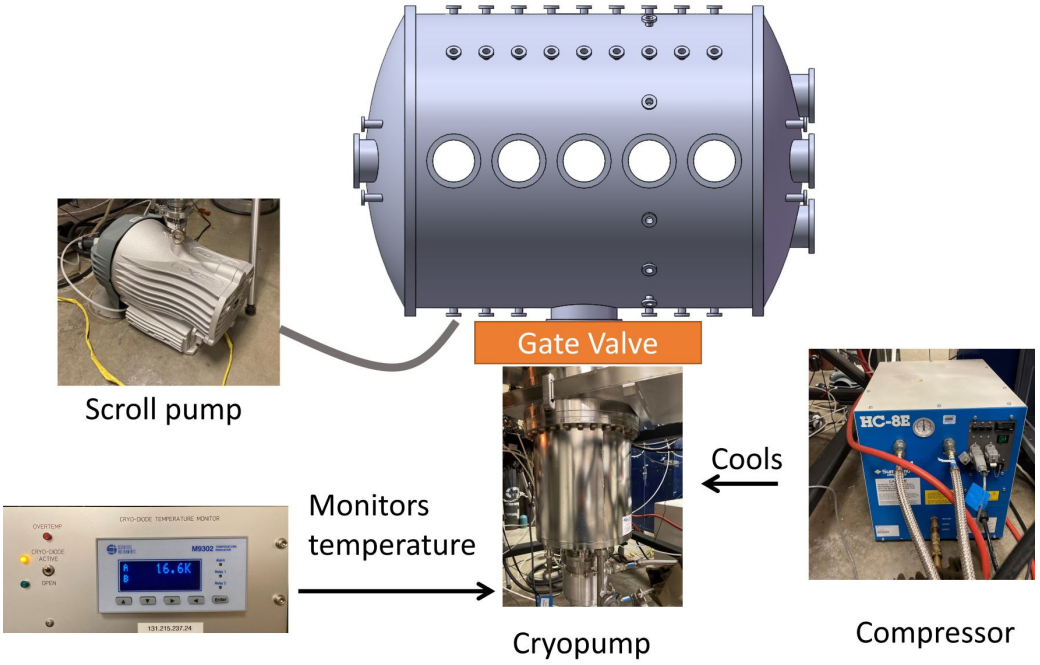

Figure 2.9: A scroll pump is used as a roughing pump to lower the pressure inside the vacuum chamber to around 1×10^{-2} torr. A cryopump then further lowers the pressure to below 1×10^{-6} torr. The gate valve between the cryopump and the vacuum chamber closes automatically when the temperature reading on the temperature monitor becomes greater than 25 K.

Table 2.2: Available plasma diagnostics for the plasma jet experiment.

Diagnostic	Properties measured	Reference
High-voltage probe	Voltage	
Rogowski coil	Current	[46]
Scintillator-Photomultiplier X-ray detector	X-ray time and intensity	[18, 47]
Scintillator-Based X-ray camera	X-ray intensity, time, and location	[43]
PIN-Diode-Based X-ray camera	X-ray intensity, time, and location	[43] and this thesis
Fast framing camera	Macroscopic dynamics in visible light	
Spectroscopy system	Visible light spectrum	[34, 46]
Extreme ultraviolet (EUV) imaging system	EUV intensity, time, and location	[19, 48]
Magnetic probe array	Magnetic field vectors	[44, 35]
Quadruple wave probe	Magnetic field vectors	[20, 49]
Translatable interferometer	Electron density	[33, 32]

compressor (Sumitomo HC-8E4) to $\sim$ 10 K. The temperature inside the cryopump is sensed by a delicate cryogenic temperature silicon diode (Scientific Instruments Si410). The voltage across this diode is monitored and converted to a temperature reading by a cryogenic temperature monitor (Scientific Instruments M9302). When the temperature reading becomes greater than 25 K, the gate valve between the large vacuum chamber and the cryopump automatically closes to isolate the large chamber from the cryopump.

2.3 Plasma Diagnostics

This section briefly summarizes each of the available plasma diagnostics for the plasma jet experiment. These diagnostics have provided many high-quality measurements that result in new discoveries. Relevant references for these plasma diagnostics are provided in Table 2.2.

High Voltage Probe

A $\times$1000 high-voltage oscilloscope probe (Tektronix P6013A) is connected to the inner disk electrode to measure voltage difference across the disk-annulus electrodes. The output of this voltage probe is designed to drive a 1 MΩ oscilloscope input channel. A buffer circuit is connected to the output of this probe, so the output can drive a 50 Ω digitizer input channel.

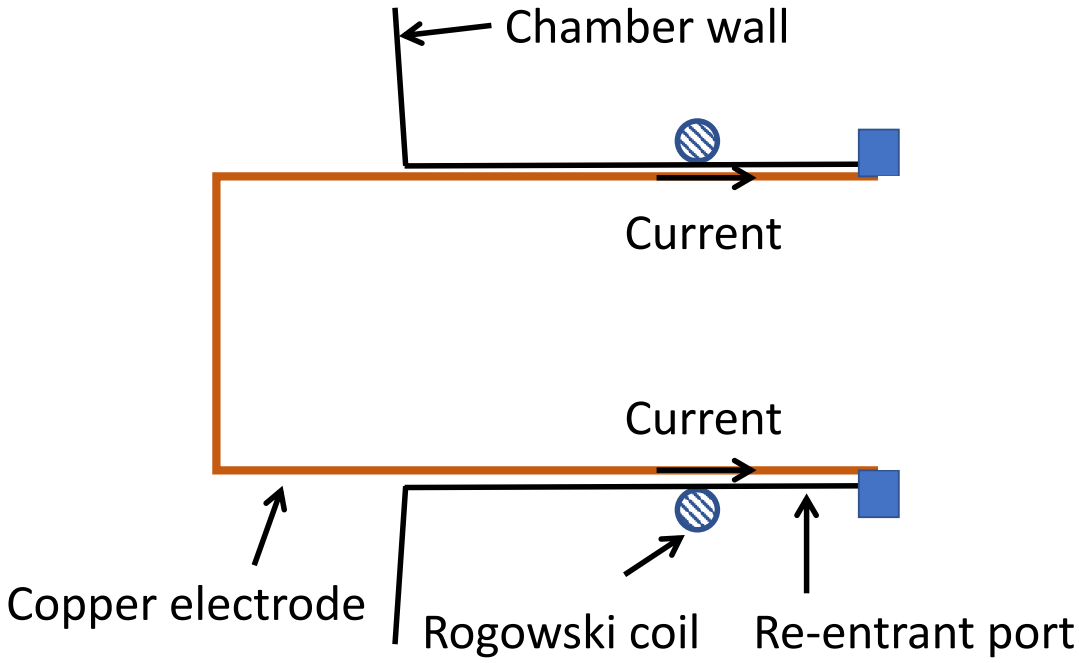

Figure 2.10: This side view diagram illustrates the position of a Rogowski coil that is wrapped around a re-entrant port on which the inner electrode is mounted. The inner electrode is insulated from the grounded chamber wall by a ceramic break.

Rogowski Coil

A Rogowski coil is used to measure the pulsed current flowing through the plasma jet. The torus core of this coil surrounds a re-entrant port that is coaxial with the inner disk electrode (see Figure 2.10). Figure 2.11 shows that the AC current flowing through hole of the torus generates a time-varying magnetic flux through the coil of wire that wraps around the torus. This time-varying magnetic flux then generates a voltage, which is proportional to the time derivative of the current, across the two ends of the wire. The voltage is integrated by a passive RC integrator coupled to the coil to give a current measurement.

Scintillator-Based X-ray Detector

A seven-channel scintillator-based X-ray detector (developed by Ryan Marshall [18, 47]) is mounted inside the vacuum chamber to detect transient X-ray bursts. This detector uses seven plastic scintillators (Eljen Technology EJ-200) to convert X-ray photons into visible light photons. These visible light photons are carried by seven 10 m plastic optical fibers to seven photomultipliers (Hamamatsu H10721). The photomultipliers (PMTs) convert visible light photons into electrical signals which

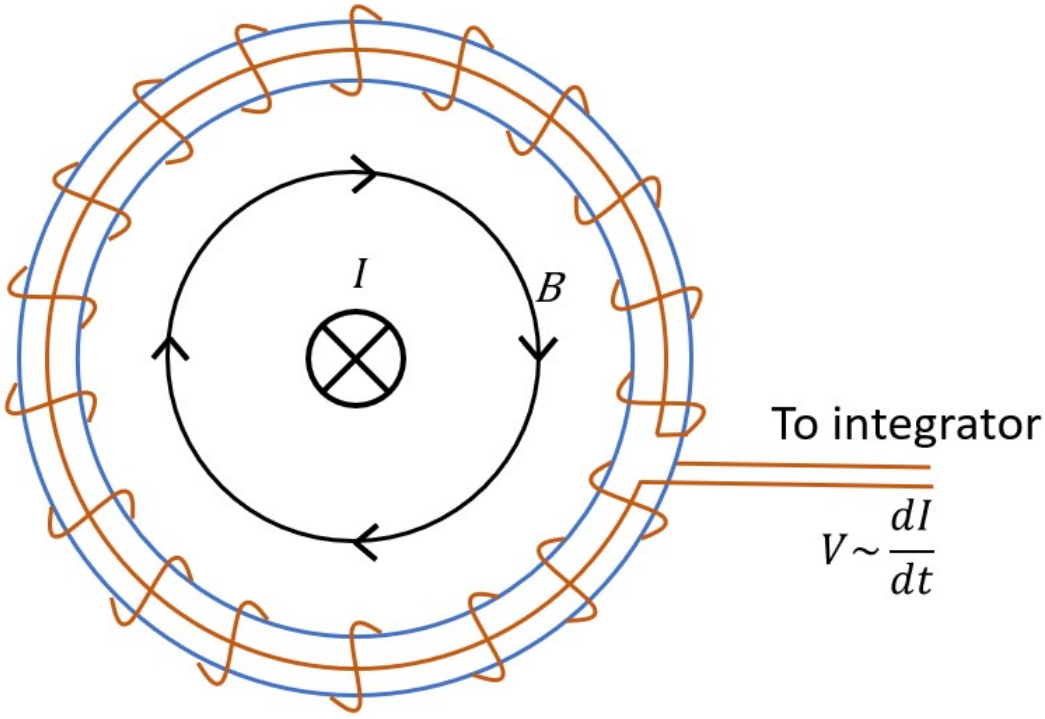

Figure 2.11: A Rogowski coil that measures the AC current flowing through the hole of the torus. The voltage across the coil of wire is proportional to the time derivative of the current. An integrator integrates the signal from the coil to give a current measurement.

are recorded by seven input channels of a digitizer. Figure 2.12 illustrates how the components of the scintillator-photomultiplier X-ray detector are connected to each other.

Compared to other X-ray diagnostics, this detector is the closest to the plasma jet (around 40 cm from the plasma jet). Thus, the X-ray intensity the detector sees is the largest. This X-ray detector does not have the capability to resolve X-rays spatially.

Scintillator-Based X-ray Camera

A scintillator-based X-ray camera (developed by Seth Pree [43]) placed outside the vacuum chamber has been used to locate the X-ray sources. Figure 2.13 shows the major components of this camera. The X-rays from the plasma jet experiment pass through a custom-made Kapton window and reach a pinhole or a coded aperture mask outside the vacuum chamber. The X-ray images formed by the mask are recorded by a 128-channel scintillator-based X-ray sensor array.

The array is composed of 128 LYSO(Ce) scintillators on a 1 mm pitch coupled via

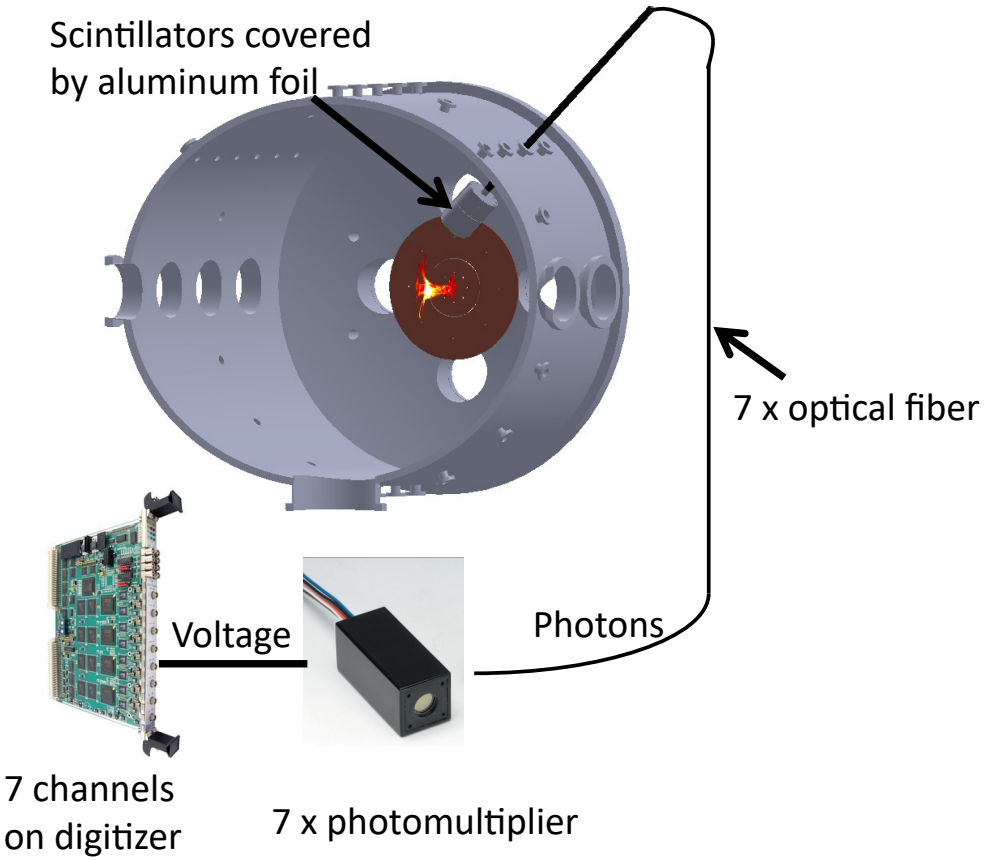

Figure 2.12: The components of the scintillator-photomultiplier X-ray detector are shown in this diagram. The scintillators inside the vacuum chamber convert X-rays from the plasma jet experiment to visible light photons. These photons are delivered to photomultipliers outside the vacuum chamber by ten-meter-long optical fibers. The photomultipliers convert the visible light photons to electrical signals. These signals are recorded by a digitizer.

a 12-meter plastic fiber (Eska CK-30) array to 128 fast photomultipliers arranged as four 32-channel modules (Hammamatsu H7260-100). Each scintillator has a 0.64 mm^2 active area that converts X-rays to visible light. The PMTs and associated electronics then convert the visible light to ~40 ns wide voltage pulses which are recorded by a 128-channel, 125 MHz digitizer (CAEN R5560).

PIN-Diode-Based X-ray Camera

A PIN-diode-based X-ray camera (developed by Yi Zhou [43]) that is similar to the scintillator-based X-ray camera has been developed. The main difference is that PIN-diode-based X-ray Camera uses PIN diodes instead of scintillators as the X-ray detector. The PIN diodes absorb X-ray photons and release electron-hole pairs.

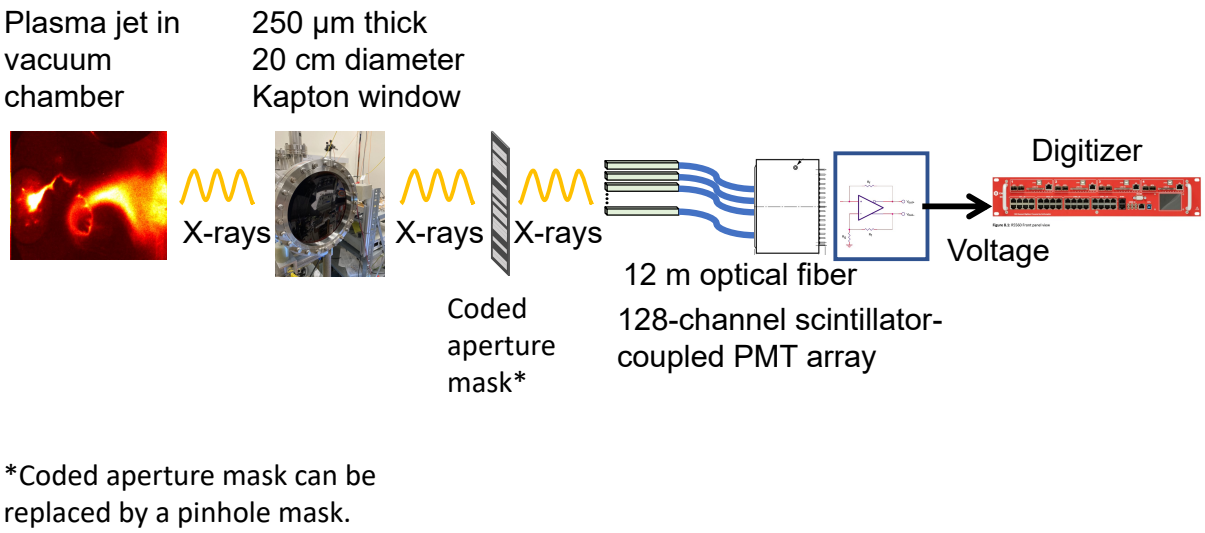

Figure 2.13: This diagram illustrates the major components of the scintillator-based X-ray camera. X-rays from the plasma jet experiment go through a Kapton window and reach a coded aperture mask outside the vacuum chamber. The X-ray images formed by the mask are recorded by a 128-channel scintillator-based X-ray sensor array. The output signals of the array are recorded by 128 input channels of a digitizer.

These charge carriers are converted to $\sim$ 1 μs voltage pulses by charge-sensitive preamplifiers (CSPs) coupled to the PIN diodes. The design and implementation of this camera will be described in detail in later chapters.

Both the PIN-diode-based camera and the scintillator-based camera have high detection efficiency over a broad X-ray band, a wide field of view, and the capability to produce $>$ 50 time-resolved frames with $\leq$ 1 μs time resolution. However, there are some differences between the the two X-ray sensors. The LYSO(Ce) scintillators' efficiency peaks when absorbing 1 MeV photons [50] whereas the PIN diodes are only efficient at fully absorbing photons with energy $<$ 30 keV [51].

The detection mechanisms of the two X-ray sensors also differ. The scintillator converts X-rays to visible light photons, so an extra photodetector is required to convert the visible light photons to an electrical signal. The scintillator-based sensor uses a PMT, which has the advantage of very large gain. Because the PMT is coupled to the scintillator via a 12-meter-long fiber, the PMT and associated electronics can be placed far away from the electrically noisy plasma experiment so that unwanted electromagnetic interference is minimized. In comparison, the PIN diode converts X-rays directly to an electrical signal, so an extra photodetector is

Table 2.3: Key differences between the PIN-diode-based X-ray sensor and the scintillator-based X-ray sensor.

	PIN-diode-based sensor	Scintillator-based sensor
Efficient detection energy	< 30 keV	5 keV–1 MeV
Conversion	X-ray to photocurrent	X-ray to visible light photons
Photodetector	Direct conversion of x-rays to current	Requires an additional photodetector
Amplifier	CSP	PMT
Time resolution	1 μs	40 ns
Use case	Imaging < 30 keV X-rays; Experiments on a 10 μs time scale	Imaging > 30 keV X-rays; Experiments on a 100 ns time scale

not required. Since the PIN diode itself does not have any gain mechanism, a CSP is needed to amplify the signal to a detectable level. Since the CSP is closely coupled to the PIN diode via a pin header, extra effort is needed to shield the CSP from the electromagnetic interference from the plasma experiment.

The differences between the two sensors result in distinctions in their performances; the scintillator-based sensor has a faster time resolution (40 ns vs 1 μs) and greater efficiency for detecting > 30 keV X-rays compared to the PIN-diode-based sensor. Therefore, the scintillator-based sensor is ideal for imaging > 30 keV X-rays from experiments with a fast time scale on the order of 100 ns. On the other hand, the PIN-diode-based sensor is appropriate for imaging < 30 keV X-rays from experiments with a time scale on the order of 10 μs. A summary of the key differences between the two X-ray sensors is in Table 2.3.

Fast Framing Camera

Photographs of the plasma jet are taken via a fast framing camera (DRS HADLAND Imacon 200). This powerful intensified charge-coupled device (ICCD) camera can take 14 frames of grayscale images with an adjustable interframe time. The minimum interframe time is 5 ns. For the plasma jet experiment, the interframe time is typically set to 0.5–1 μs. Thus, the 14 frames show a time evolution of the plasma plasma jet over 7–14 μs. These images provide valuable information regarding the macroscopic dynamics of the plasma jet.

It is generally believed that the pixel value on a grayscale image of a plasma is

proportional to particle density squared. Therefore, the fast framing camera also quantitatively measures the particle density of the plasma jet.

Spectroscopic System

The spectroscopic system (developed by Gunsu Yun [34, 46]) consists of a camera lens, a 12-channel fiber array, a concave mirror, a 1-meter- long spectrometer (HORIBA Jobin Yvon SPEX 1000m), and an ICCD camera (Andor iStar). Figure 2.14 shows the setup of the system. The 12-channel fiber array consists of 12 optical fibers with input ends arranged in a linear pattern. This fiber array allows the spectroscopic system to simultaneously view plasma emission at 12 evenly spaced locations along the axial direction of the plasma jet. The spacing between these locations is around 2 cm. The light emission from these 12 locations is fed into the spectrometer and split into emission lines of different wavelengths. These lines are recorded by the ICCD camera. Shifts, broadening, and intensity ratios of emission lines can be used to infer various plasma parameters such as the flow velocity, density, and temperature.

Extreme Ultraviolet Imaging System

20–60 eV extreme ultraviolet (EUV) radiation from the plasma jet can be imaged by the EUV imaging system (developed by Kil-Byoung Chai [19, 48]) illustrated in Figure 2.15. The optics of this system include a Mo:Si multilayer mirror, a YAG:Ce scintillator coated with a 200 nm aluminum film, and two mirrors. All the optics are mounted inside the large vacuum chamber of the plasma jet experiment to prevent EUV radiation from being attenuated by air. The multilayer mirror consists of alternating layers of Mo and Si that are separated by $d \approx 18$ nm. EUV radiation with wavelength λ and incident angle θ that satisfy the Bragg condition

$$n\lambda = 2d \sin\theta, \tag{2.6}$$

where n is an integer that corresponds to the order of reflection, can be focused by the multilayer mirror. The EUV image formed by the multilayer mirror is projected onto the scintillator screen and converted to a visible light image. The two mirrors of the system direct the visible light image toward a fast framing camera outside the vacuum chamber.

Magnetic Probe Array

The magnetic field in the experiment is measured by a 60-channel magnetic probe array developed by Carlos Romero-Talamás [44, 35]. The array consists of 20

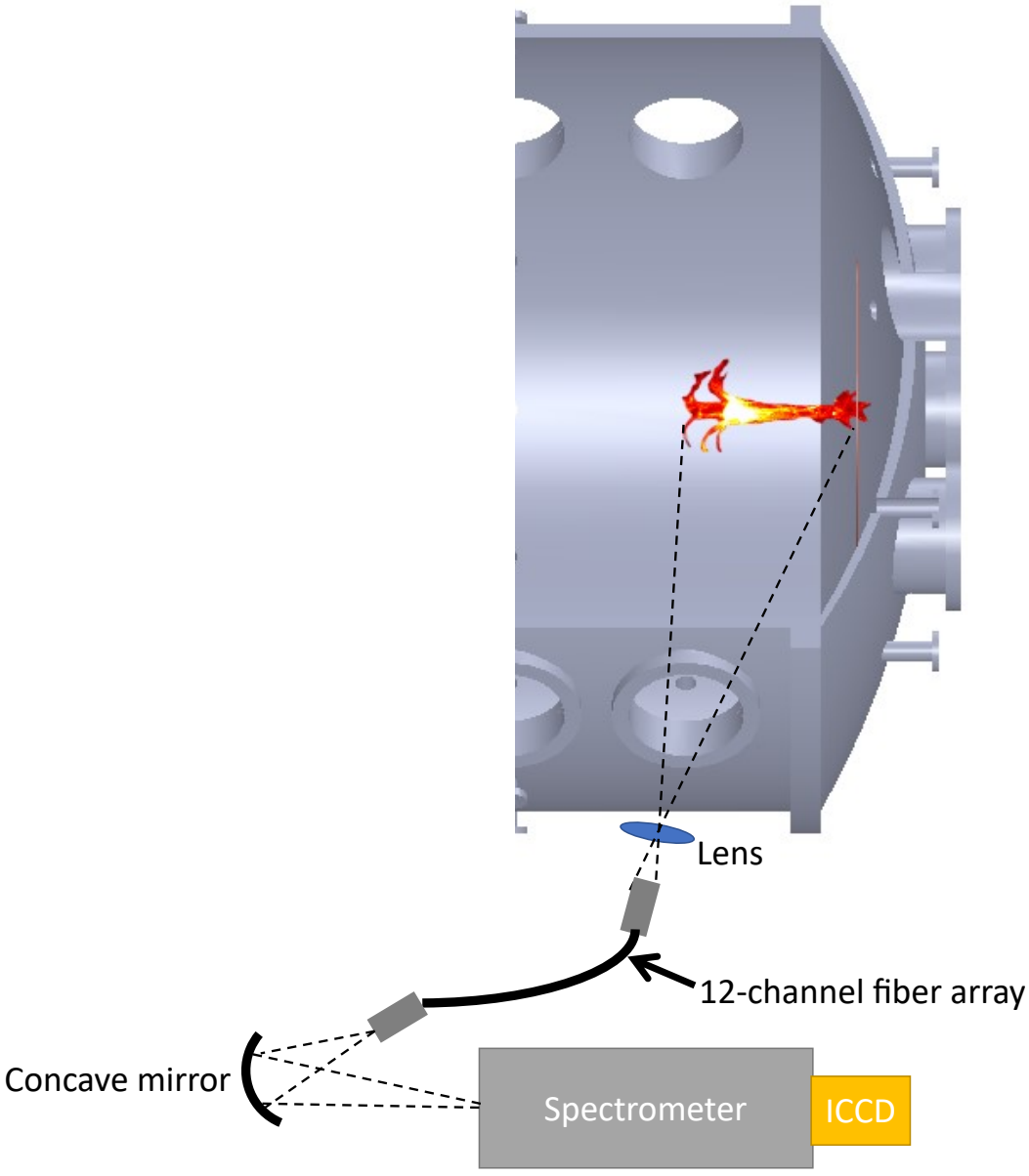

Figure 2.14: The setup of the spectroscopic system for the plasma jet experiment (top view). Visible light emission from 12 different locations of the plasma jet is focused by a lens onto the input of a 12-channel fiber array. The light is fed into a spectrometer by a concave mirror. The spectrum is recorded by an intensified charge-coupled device (ICCD) camera.

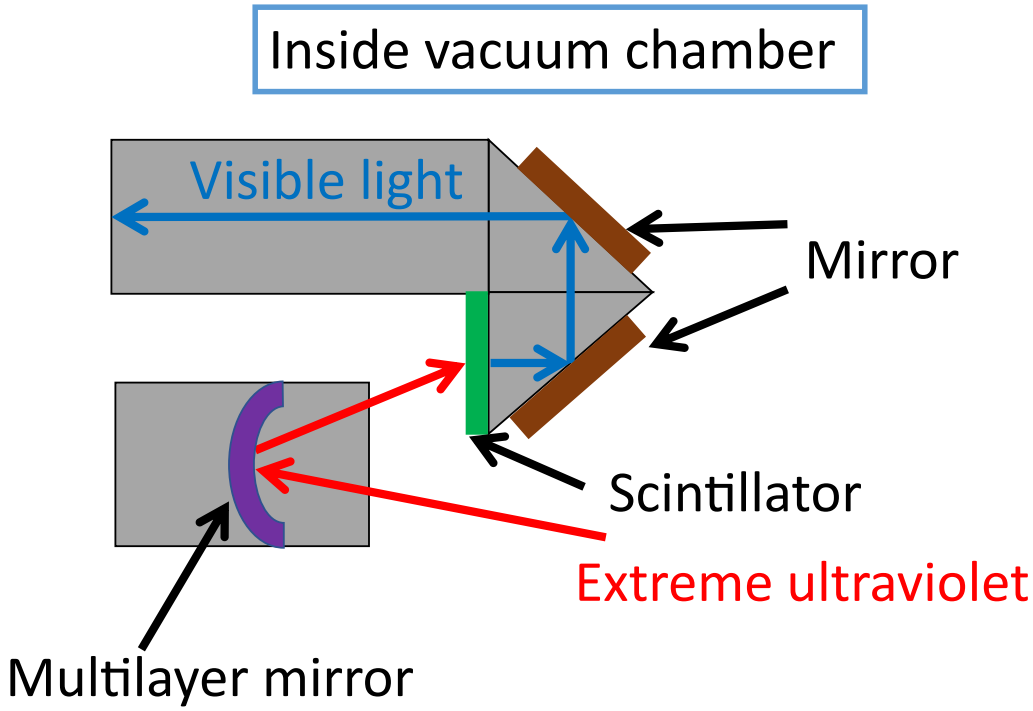

Figure 2.15: This diagram shows the optics of the extreme ultraviolet (EUV) imaging system used to image 20–60 eV EUV radiation. The optics include a Mo:Si multilayer mirror, a YAG:Ce scintillator coated with a 200 nm thick aluminum film, and two mirrors. Because EUV is highly attenuated by air, the entire setup is inside a vacuum chamber. The multilayer mirror can focus EUV radiation onto the scintillator. The scintillator converts the EUV image formed by the multilayer mirror into a visible light image. The visible light is reflected by the two mirrors toward a fast framing camera outside the vacuum chamber.

clusters of three RF inductors (Coilcraft 1008CS-472XGBB) inside quartz tubing. These clusters are arranged in a linear array with a inter-cluster spacing of 2 cm. The three inductors in each cluster are oriented in three orthogonal directions. The change in magnetic flux through each of these inductors generate a voltage across the inductor according to Faraday's law. Therefore, the magnetic probe array can measure all three components of magnetic field vectors at 20 distinct locations.

Figure 2.16 shows the location of magnetic probe array relative to the plasma jet. The magnetic probe array is mounted inside the vacuum chamber and oriented in the radial direction of the plasma jet (see Figure 2.16 for directions of the coordinate system). The array can be shifted linearly along the z direction and also rotated in the θ direction. The output voltages generated by the array are recorded by 60

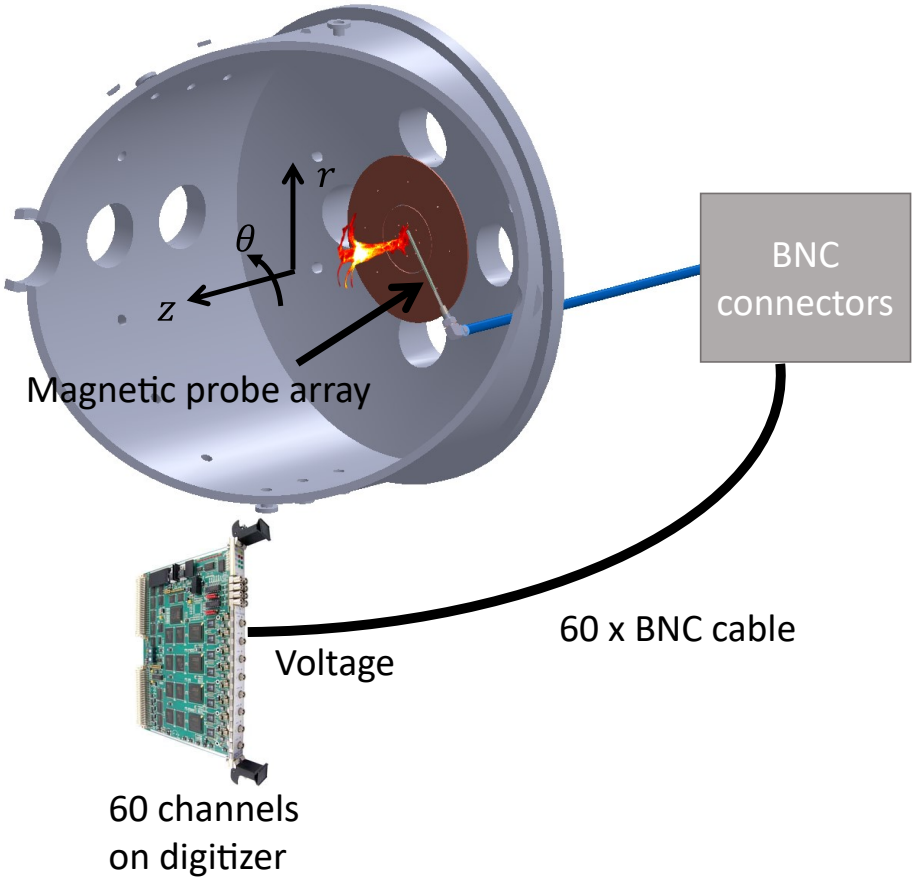

Figure 2.16: This diagram shows the position of the magnetic probe array. The magnetic probe array is along the radial direction of the plasma jet and can be translated linearly along the z direction and rotated along the θ direction. The output voltages of the array are recorded by a digitizer outside the vacuum chamber. These recorded voltages are numerically integrated to give magnetic field measurements.

individual digitizer channels. These output voltages are then integrated numerically to give magnetic field measurements.

Quadruple Wave Probe

Magnetic field fluctuations excited by the plasma jet can be measured by a quadruple wave probe developed by Magnus Haw [20, 49]. This probe consists of 4 clusters of 3 wire loops that are perpendicular to each other. The 3 wire loops in each cluster can measure 3 orthogonal components of a magnetic field vector. The 4 clusters are arranged in a regular tetrahedron geometry so that the spatial variation of the magnetic field vector can be sampled to calculate the current density via Ampère's

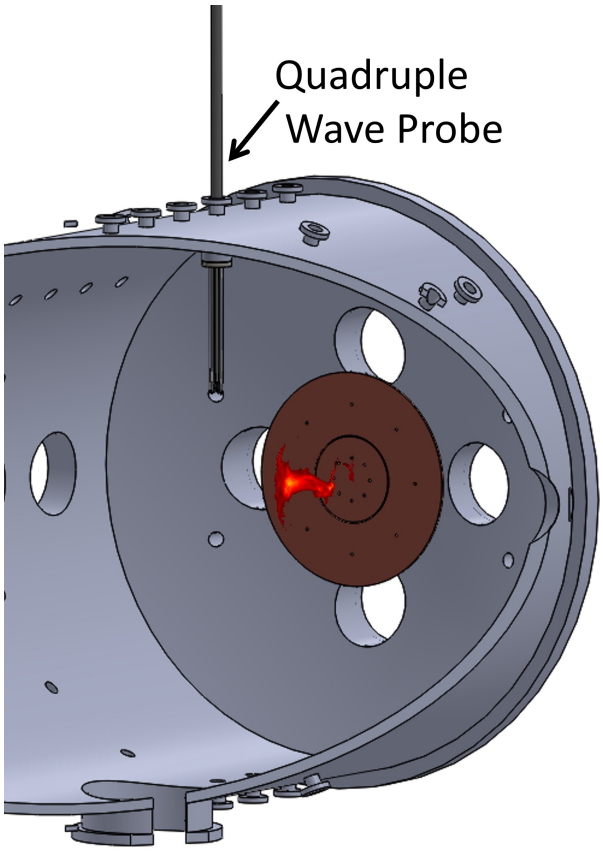

Figure 2.17: This figure shows the position of the quadruple wave probe relative to the plasma jet.

law, i.e.,

$$\nabla \times \mathbf{B} = \mu_0 \mathbf{J}. \tag{2.7}$$

Figure 2.17 shows the location of the probe.

Translatable Interferometer

A spatially translatable interferometer, first developed by Deepak Kumar then upgraded by Byonghoon Seo [33, 32], can be used to measure the line-integrated electron density in the plasma jet. The laser beam (He-Ne laser) in Figure 2.18 shows the line of measurement. The entire setup can be shifted along the axial direction of the plasma jet.

The laser beam bounces between the two mirrors mounted on the metal frame inside the vacuum chamber and propagates through the plasma jet twice. During this

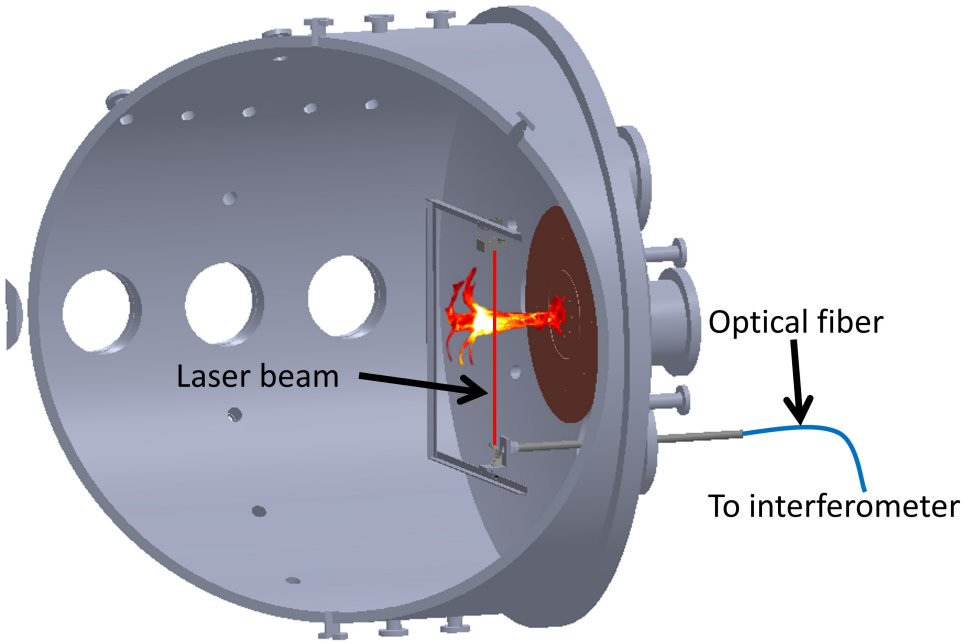

Figure 2.18: This diagram illustrates how a laser beam intercepts the plasma jet. The plasma jet induces a phase shift in the laser beam. The line-integrated electron density can be inferred from this phase shift.

propagation, a phase shift $\Delta\phi$ is induced by the plasma according to the equation

$$\Delta\phi = \frac{e^2\lambda_0}{2\pi c^2 m_e \varepsilon_0} \int n \, \mathrm{d}x, \tag{2.8}$$

where $\lambda_0 = 632.8nm$ is the He-Ne laser wavelength and the density integral is over the length of the plasma traversed by the laser beam. This laser beam is then coupled to an optical fiber and delivered to a interferometer outside the vacuum chamber. Through interference with a reference beam that has not propagated through the plasma, the plasma-induced phase shift can be resolved. The line-integrated electron density can then be determined from the plasma-induced phase shift.

2.4 Typical Plasma Evolution

This section describes the LF and the HF plasma configurations that are studied in this thesis. Figure 2.19 shows a reproducible time sequence of false color images for a plasma in the LF configuration. This configuration is called the LF (low-flux) configuration because the background magnetic flux generated by the magnetic flux

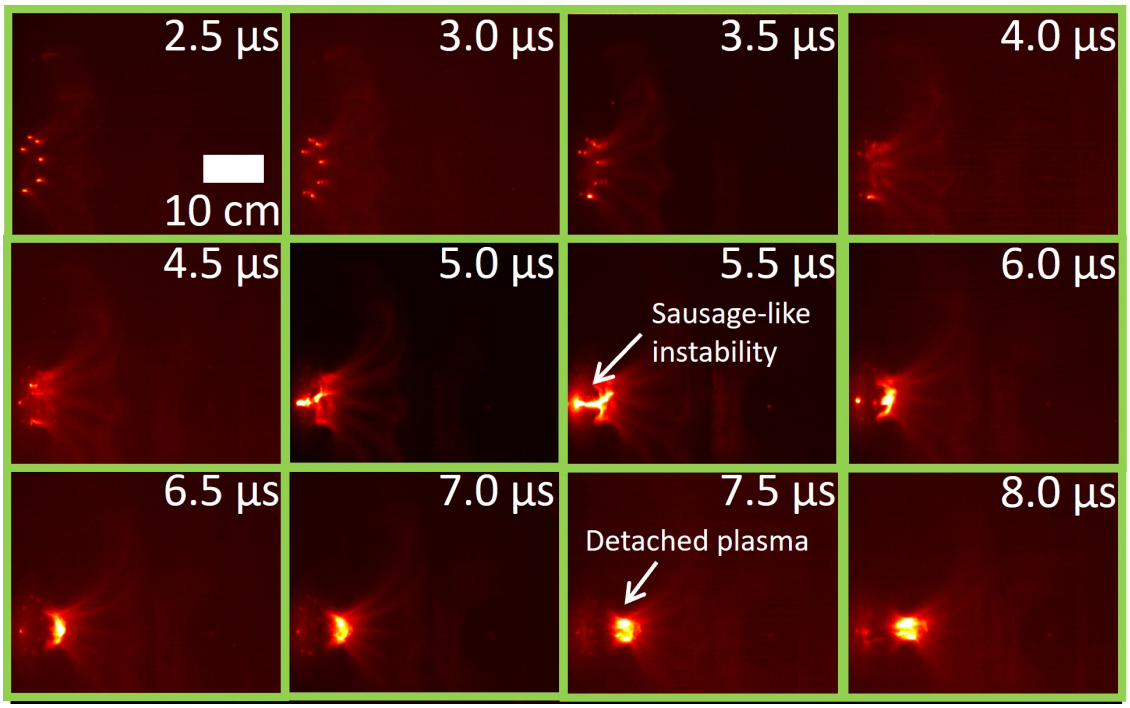

Figure 2.19: False color images showing the time evolution of a plasma in the low-flux configuration (shot 29863). The plasma detaches from the electrode due to a sausage-like pinching effect.

system is relatively low (around 0.2 mWb). In this typical sequence, spider-leg like plasma arches that follow the background magnetic field lines (see Figure 2.3) form roughly t = 2.5 µs after plasma breakdown. Because these plasma arches carry parallel current, they attract each other and merge into a single plasma column at t = 5 µs. The plasma column is then quickly pinched off from the electrode by a sausage-like instability [16] at t = 5.5 µs. The detached plasma jet then continues to propagate forward as a self-contained sphere for around 10 µs.

Figure 2.20 shows a typical sequence for a plasma in the HF configuration. The background magnetic flux in this configuration is significantly higher (around 1.8 mWb). This higher magnetic flux stabilizes the sausage-like instability so that the plasma column does not get pinched off from the electrode. Instead, the plasma column lengthens and becomes a collimated plasma jet. The pulse-forming network sustains this plasma jet so that it can last around 40 µs. At t = 22 µs, the plasma jet has lengthened from several centimeters to tens of centimeters and starts to develop a Kruskal-Shafranov kink instability [14]. This instability causes the plasma jet column to become helical. Since the kinking is a rapid exponential growth of a

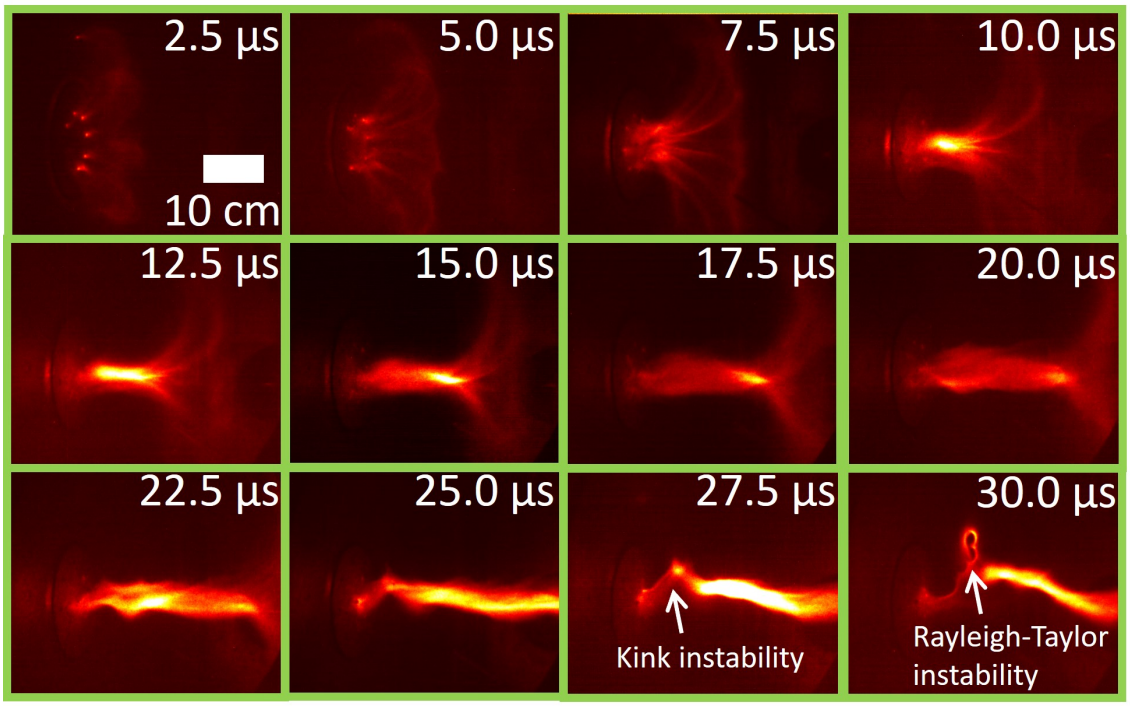

Figure 2.20: False color images showing the time evolution of a plasma in the high-flux configuration (shot 29446). The plasma undergoes kink and Rayleigh-Taylor instabilities.

corkscrew shape, this kinking produces a strong lateral acceleration of each segment of the plasma jet away from the initial axis of the jet. This lateral acceleration, as illustrated in Figure 2.21, provides a large effective gravity (10^{10} – 10^{11} m s^{-2}) that causes a secondary instability called the Rayleigh-Taylor (RT) instability [15]. As the RT instability grows, finger-like ripples constrict the cross section of the plasma jet as can be seen in the last image in Figure 2.20. Chai, Zhai, and Bellan have observed EUV radiation and visible light dimming at the constriction location. Chapter 5 will present an interesting plasma physics model that is consistent with these two observations.

Figure 2.22 shows the timelines of the plasma evolution in two the different experimental configurations.

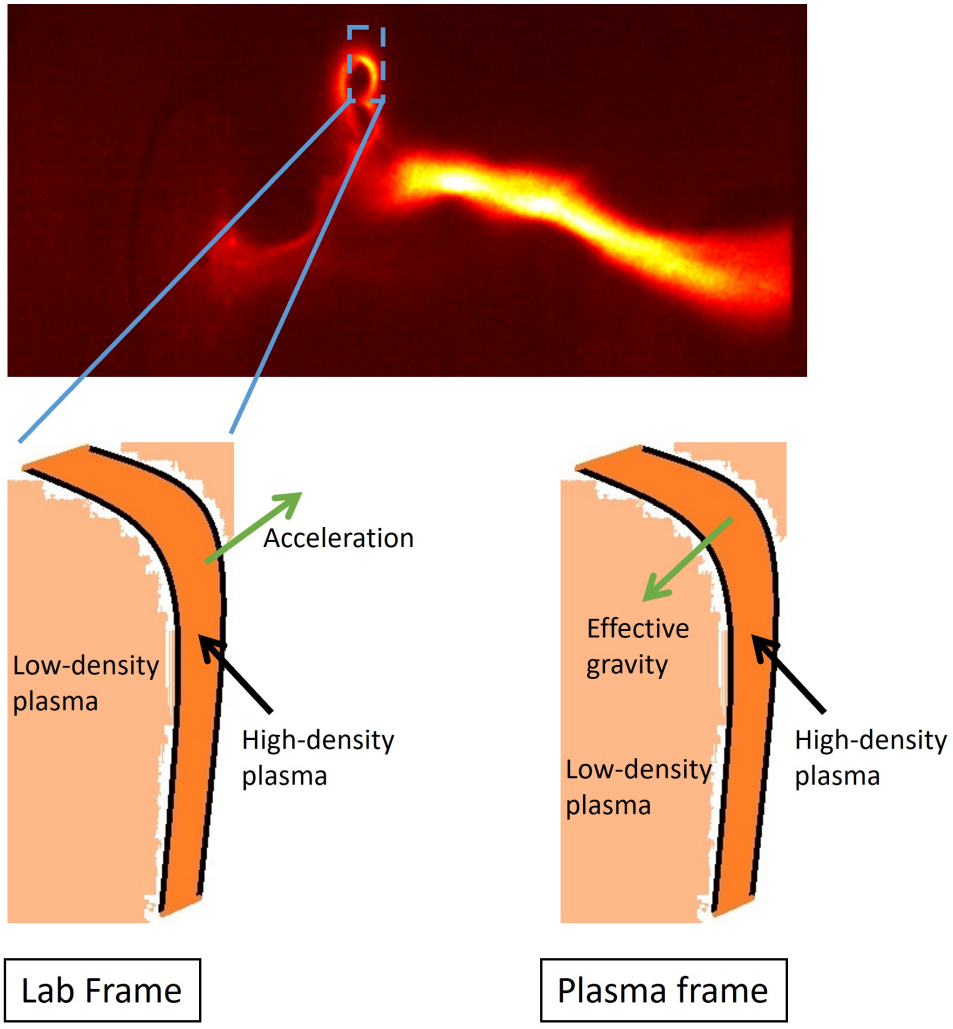

Figure 2.21: The kinking of the plasma jet accelerates the plasma segment inside the dashed box away from the axial direction of the plasma jet. In a frame that moves together with the plasma segment, this acceleration acts as an effective gravity. Because of this gravity, the high-density plasma effectively lies on top of a lighter low-density plasma on the trailing side the plasma jet. This configuration is unstable because the location exchange of the high-density plasma and the low-density plasma reduces the overall gravitational potential energy in the plasma frame. Therefore, small ripples of high-density plasma penetrate into the low-density plasma at the interface between the two plasmas.

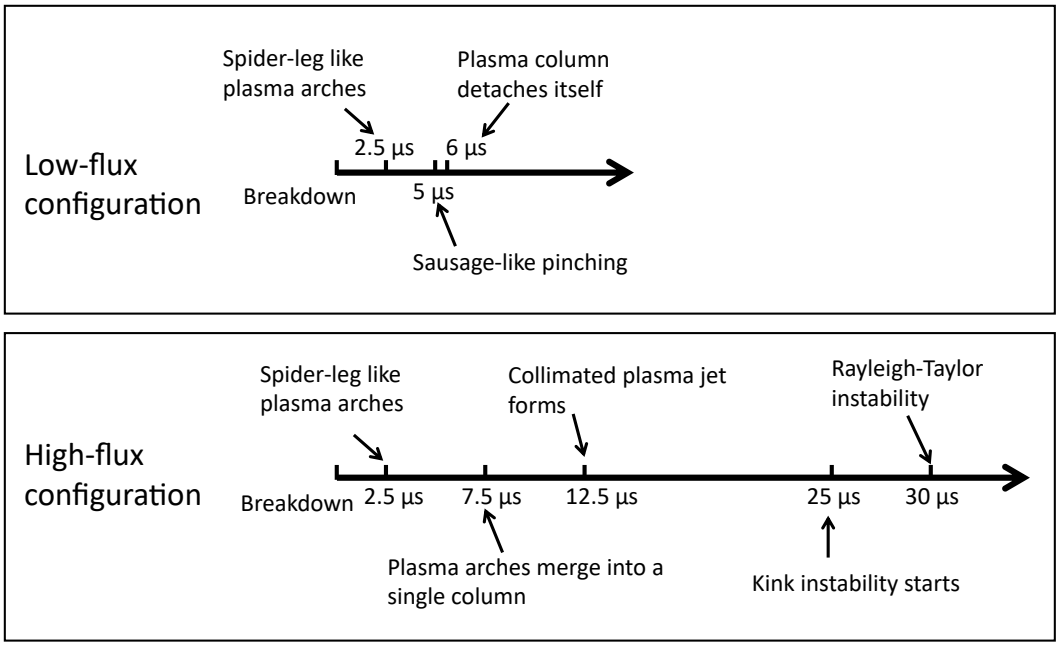

Figure 2.22: Timelines that summarize key events in the low-flux configuration and the high-flux configuration.

Chapter 3

DESIGN OF THE PIN-DIODE-BASED X-RAY CAMERA

[1] Y. Zhou, S. Pree, and P. M. Bellan. "Imaging suprathermal x-rays from a laboratory plasma jet using PIN-diode-based and scintillator-based 1D pinhole/coded aperture cameras". In: *Review of Scientific Instruments* 94 (2023), p. 013504. DOI: 10.1063/5.0122760.

3.1 Introduction

X-rays observed from astrophysical plasmas contain information regarding the energy and trajectory of highly energetic particles. Such energetic particles are indicative of nonequilibrium or unstable plasma dynamics, and there has been sustained interest in their study in order to discover and understand exotic plasma dynamics. Similarly, laboratory experiments designed to simulate astrophysical phenomena have been shown to produce suprathermal X-rays. Studying X-rays in laboratory plasmas is a promising route to understanding the dynamics which lead to extreme particle acceleration. Toward that goal, time-resolved X-ray imaging is an especially desirable method.

In the Caltech plasma jet experiment, transient (1 μs duration), low-intensity (a few photons per mm^2 at 1 m), suprathermal X-rays with a broad energy spectrum ($\Delta E \approx$ 4 keV) centered around 6 keV have been detected when magnetohydrodynamic (MHD) instabilities disrupt a cold (2 eV) plasma jet [16, 18]. These X-rays appear sporadically in a 20 μs time window. Detection of these X-rays is surprising because particles in the plasma jet are not expected to accelerate from $\sim$ 2 eV to $\sim$ 6 keV due to the collisional mean free path ($\sim$ 1 μm) being several orders of magnitude shorter than the 10 cm characteristic length scale of the plasma jet. Studying where and how these unexpected X-rays are generated may provide insight into X-ray generation mechanisms in solar and astrophysical contexts due to the scalability of the Caltech experiment [10, 11, 12, 13]. To locate the source of X-rays and clarify whether and how the simultaneous MHD instabilities facilitate the generation of these X-rays, X-ray imaging is necessary.

Special methods are required to manipulate X-rays to form images because conventional lenses and mirrors are not suitable. X-ray imaging methods successfully implemented to date include grazing-incidence reflection [52], Bragg-reflection [53],

Fresnel zone plate [54], compound refractive lens [55], pinhole [56], and coded aperture [57]. Even though the grazing-incidence reflection, Bragg-reflection, Fresnel zone plate, and compound refractive lens methods can form high-resolution X-ray images, these methods can only focus X-rays with a very specific angle of incidence or energy. For example, the Bragg-reflection method used by Sinars et al. [53] only had a <0.5 eV spectral bandpass and only focused X-rays with an angle of incidence equal to the Bragg angle. Hence, these focusing methods are not appropriate for imaging broad-band, low-intensity X-rays that have a wide range of incident angles, such as the X-rays from the Caltech plasma jet experiment. In comparison, pinhole and coded aperture methods are both appropriate because they form images over a broad range of X-ray energies and angles of incidence.

Although pinhole imaging is the simplest method for producing X-ray images, its photon-collection efficiency is low. This low efficiency often results in an image with an insufficient signal-to-noise ratio (SNR). Coded aperture imaging improves the photon-collection efficiency by using a large number (N) of pinholes arranged in a specific pattern to collect incident X-rays. The improved collection efficiency gives an increased SNR that can be on the order of $\sqrt{N}$ times the SNR from a single pinhole [58]. An improvement in SNR is particularly useful for imaging the X-rays from the Caltech experiment because the intensity of the X-rays is very low. The raw image projected by the coded aperture, however, does not resemble the original X-ray source due to the overlapping of individual pinhole images, so a decoding algorithm is needed to reconstruct the image of the X-ray source [59, 60, 61]. The coded aperture method has been used on spacecraft to image astrophysical X-ray sources [62, 63, 64]. It has also been used in laboratory to produce time-integrated images of stationary radioactive sources [57, 65, 66]. However, it has not previously been used to produce time-resolved images of transient, low-intensity, and suprathermal X-rays from laboratory plasma experiments.

Given that the X-rays in the Caltech plasma jet experiment have a low intensity, a broad energy spectrum, uncertainties in when and where they can appear, and a short duration, a useful X-ray camera is required to have high detection efficiency over the 4–8 keV spectral band, a wide FOV to cover X-rays with a wide range of angles of incidence ($\Delta\theta \approx 30°$), $\sim$ 1 cm spatial resolution, and the capability to produce at least 50 time-resolved frames with $\leq$ 1 μs time resolution. A commercial X-ray camera that meets all the requirements above is not readily available. In this chapter, we describe the design and testing of a 1D PIN-diode-based coded aperture/pinhole

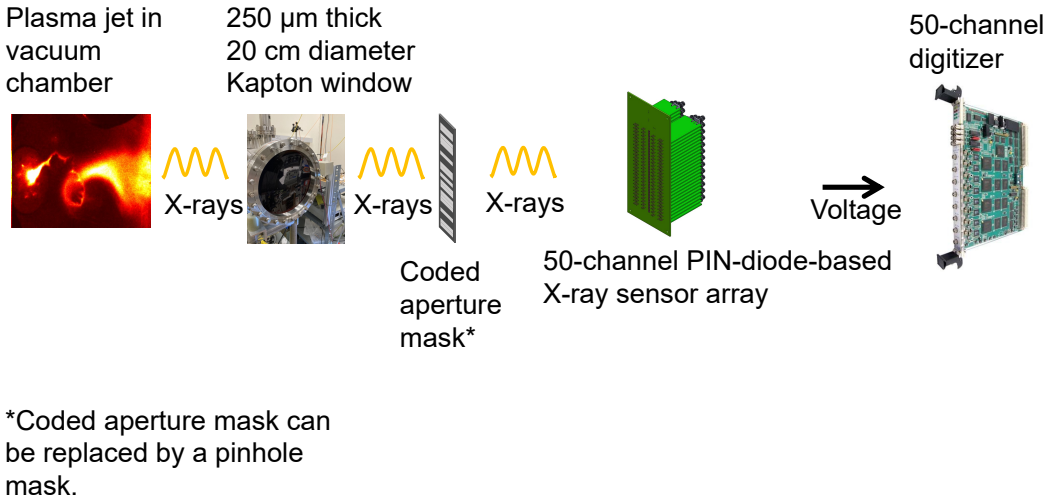

Figure 3.1: Principal parts of the X-ray camera. X-rays from the inside of a vacuum chamber pass through a Kapton window and form an image via a coded aperture mask outside the vacuum chamber. The X-ray image formed is projected onto a PIN-diode-based X-ray sensor array. The output signal from the sensor array is digitized by a fast digitizer.

X-ray camera that is capable of performing time-resolved, wide-field, broad-band imaging on the transient, low-intensity, and suprathermal X-rays from the Caltech plasma jet experiment.

3.2 X-ray Camera Components

The X-ray camera is similar in principle to a 1D visible light coded aperture camera that had been previously implemented on the Caltech plasma jet experiment by Haw and Bellan [61] as a proof-of-concept. The principal parts of the the X-ray camera are shown in Figure 3.1. These parts include a large Kapton vacuum window, a coded aperture or pinhole mask, a 50-channel, PIN-diode-based, one-dimensional X-ray sensor array covered by 18 μm thick aluminum foil, and a fast digitizer. The aluminum foil blocks visible light from the plasma jet. The X-ray sensor array is enclosed in an aluminum box (Hammond Manufacturing 1590Z162, not shown in Figure 3.1) which shields electromagnetic interference from the high-voltage power supplies of the plasma jet experiment. X-rays from the plasma jet experiment pass through the Kapton vacuum window and form an image either via a coded aperture or pinhole mask outside a vacuum chamber. The X-ray image formed is projected onto the X-ray sensor array typically located 40 cm from the Kapton window. The output signal from the X-ray sensor array is digitized and stored in a data repository server. An additional program is used to convert the stored data to X-ray images. In

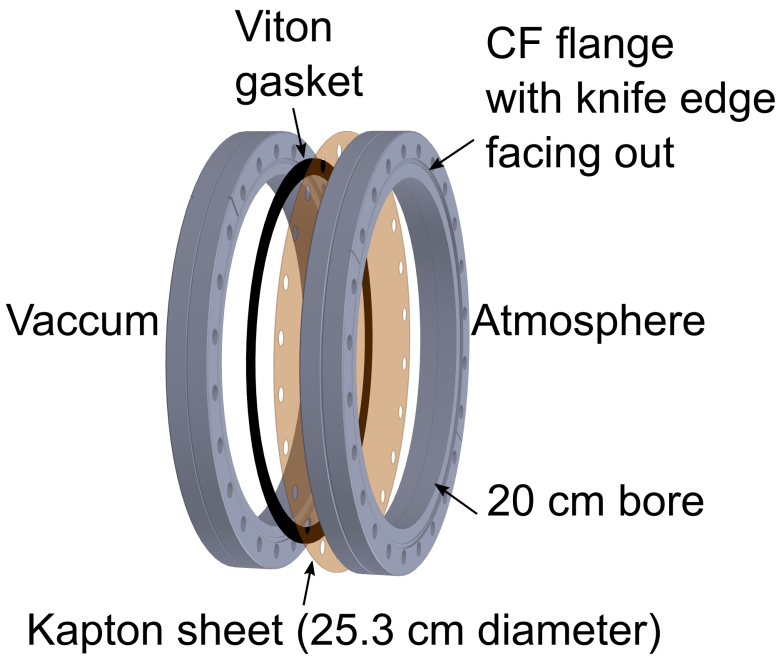

Figure 3.2: Drawing of the Kapton window assembly. The Kapton sheet is placed between a Viton gasket and a ConFlat flange. The knife edge of the flange is facing away from the Kapton sheet so that the sheet is not damaged by the knife edge.

the following sections, each principal part of the camera is described in detail.

3.3 Kapton Window

In order to utilize the entire length of the PIN-diode-based X-ray sensor array, the diameter of the Kapton window is 20 cm. The Kapton window was constructed by placing a 250 μm thick Kapton sheet between a molded Viton gasket (Kurt J. Lesker VZVIT200) and the flat side of a ConFlat flange as shown in Figure 3.2. Care was taken to avoid pressing the knife edge of the ConFlat flange directly onto the Kapton sheet since the knife edge can cut through the Kapton sheet. Holes matching the bolt holes of the flange were laser cut in the Kapton sheet so that it could be easily mounted and fastened by the bolts used for the flange. Even though the Kapton window deforms substantially when subject to a 1 atmosphere pressure differential [67], it performs reliably (see Figure 3.3 for a deformed window). After the Kapton window was installed on the vacuum chamber of the plasma jet experiment, the rate of pressure increase rose from $\sim$ 3 mtorr/hr to 5–6 mtorr/hour as measured by a thermocouple gauge with all vacuum pumps off.

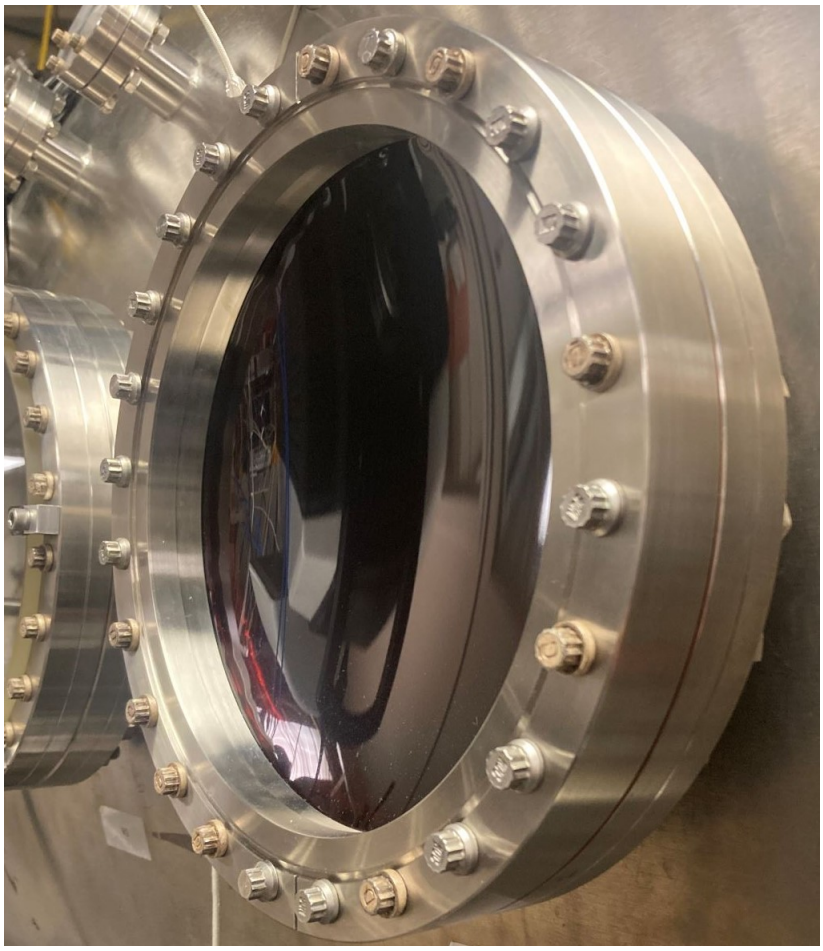

Figure 3.3: The Kapton window installed on the vacuum chamber of the jet experiment. The inner diameter of the window is around 20 cm. Notice that the knife edge of the Conflat flange is facing away from the Kapton sheet. The surface of the Kapton curves inward due to atmosphere pressure.

3.4 Coded Aperture Masks

The coded aperture masks used to form X-ray images were fabricated from 1.6 mm thick aluminum or stainless steel sheets because these metal sheets can effectively block $\sim$ 6 keV X-rays. Rectangular pinholes on these masks are laser cut and arranged in a linear pattern based on a pseudo noise (PN) sequence [61, 68]. The sequence is called the pseudo noise sequence because it is similar to random noise but can be generated in a deterministic manner. More details about how this pattern is designed will be given in a later section. Figure 3.4 shows the drawing of a coded aperture mask designed for the PIN-diode-based X-ray camera.

The imaging and decoding processes with these coded aperture masks can be modeled as matrix multiplications. Let an n-dimensional vector $\mathbf{S}$ represent the intensity

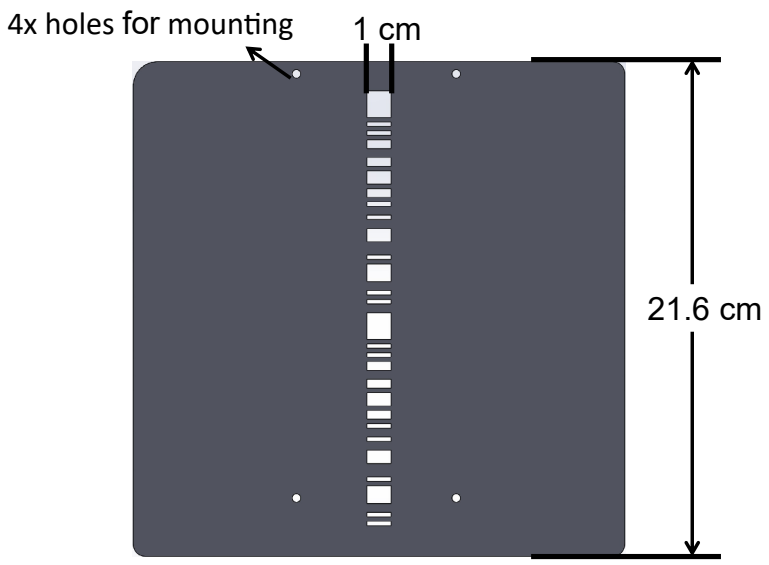

Figure 3.4: Drawing of a 99-element coded aperture mask used for the 50-channel PIN-diode-based X-ray sensor array. The 1 cm wide pinhole pattern in the middle is designed based on a pseudo noise sequence. The size of the mask element is roughly 1.7 mm (see Equation [3.4] and Figure 3.6.

samples of a distributed X-ray source. After the X-rays from this source go through the pinholes on a coded aperture mask, an X-ray image is cast onto an X-ray sensor array. Let an n-dimensional vector $\mathbf{R}$ represent the intensity samples of the recorded image. $\mathbf{R}$ can be related to $\mathbf{S}$ through the matrix multiplication

$$\mathbf{R} = \mathbf{MS}, \tag{3.1}$$

where $\mathbf{M}$ is an $n \times n$ matrix whose components are determined by the pattern on the coded aperture mask. The components of $\mathbf{M}$ are either 1 or 0. A 1 corresponds to a transparent element, and a 0 corresponds to an opaque element.

Figure 3.5 illustrates how the mask matrix components are defined by the mask pattern. In Figure 3.5(a), a 4-element X-ray source which is only bright in its first element projects the first 4 elements of a coded aperture mask onto a 4-element X-ray sensor array. The X-rays that go through a transparent mask element can light up a sensor element. The X-rays that are blocked by a opaque mask element will cast a shadow on a sensor element. If we represent a shadow by 0 and a lit up sensor element by 1, then the X-ray image projected onto the X-ray sensor array is $(1, 1, 0, 1)^T$.

Since the source vector $\mathbf{S}$ that represents the X-ray source is $(1, 0, 0, 0)^T$, the matrix

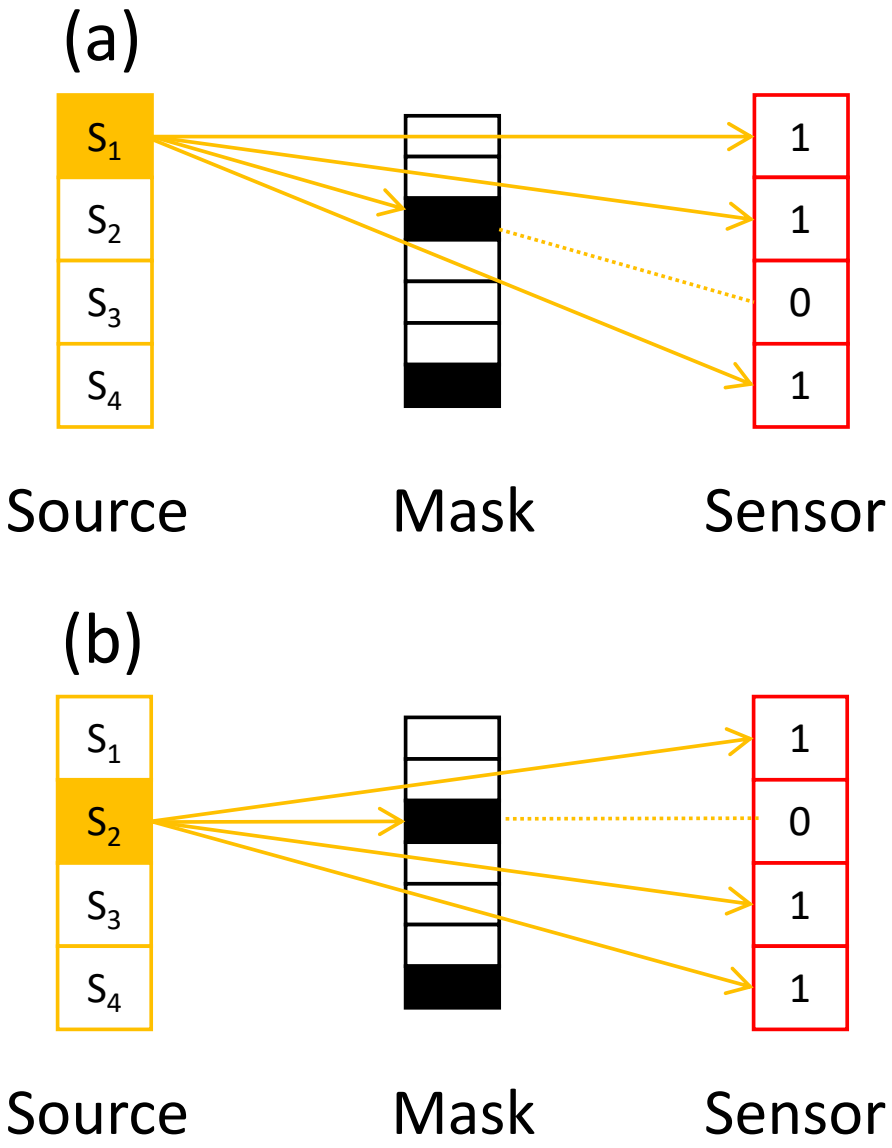

Figure 3.5: Diagrams illustrating how a four-element X-ray source projects a mask pattern onto a four-element X-ray sensor array. From these two diagrams, we can see how the columns of a 4×4 mask matrix $\mathbf{M}$ are defined by the mask pattern. (a) The first element of the X-ray source projects the first four mask elements onto the X-ray sensor array. If we represent the source vector as $\mathbf{S} = (1, 0, 0, 0)^T$, then the matrix multiplication $\mathbf{MS}$ simply extracts the first column of $\mathbf{M}$. Thus, the first column of $\mathbf{M}$ is $(1, 1, 0, 1)^T$. (b) The second element of the X-ray source projects $(1, 0, 1, 1)^T$ onto the X-ray sensor array. Thus, the second column of $\mathbf{M}$ is $(1, 0, 1, 1)^T$.

multiplication **MS** simply extracts the first column of **M**. Therefore, the first column of **M** must be $(1, 1, 0, 1)^T$. Similarly, Figure 3.5(b) shows that the second element of the X-ray source projects 1, 0, 1, and 1 onto the sensor array, so the second column of **M** must be $(1, 0, 1, 1)^T$. By repeating this procedure, we can construct all 4 columns of **M** as

$$\mathbf{M} = \begin{pmatrix} 1 & 1 & 0 & 1 \\ 1 & 0 & 1 & 1 \\ 0 & 1 & 1 & 1 \\ 1 & 1 & 1 & 0 \end{pmatrix}. \tag{3.2}$$

It is worth noting that the matrix formulation above reduces to pinhole imaging if **M** is a backward identity matrix, i.e.,

$$\mathbf{M} = \begin{pmatrix} 0 & 0 & 0 & 1 \\ 0 & 0 & 1 & 0 \\ 0 & 1 & 0 & 0 \\ 1 & 0 & 0 & 0 \end{pmatrix}. \tag{3.3}$$

In this case, the matrix multiplication **MS** simply flips **S** to produce an inverted image vector **R**.

In order to properly record the projected image as an n-element vector **R**, an n-element X-ray sensor array has to be placed at an appropriate distance to ensure a one-to-one correspondence between the components of **R** and the X-ray sensors. Figure 3.6 shows that, if the X-ray sensor array is too close to the mask, the X-ray image will only be cast onto a fraction of the array. On the other hand, if the X-ray sensor array is too far from the mask, the array will not be long enough to record the entire X-ray image. If we represent the source-to-mask distance with a, the mask-to-sensor distance with b, the length of a mask element with m, and the length of a sensor element with d, then simple geometry shows that

$$\frac{m}{d} = \frac{a}{a+b} \tag{3.4}$$

has to be satisfied to ensure the X-ray sensor array is at a proper distance [61].

In order to reconstruct an image of **S**, the mask matrix **M** needs to be easily invertible. An image of **S** can be reconstructed by applying a decoding matrix **D**, which is simply the inverse of **M**, to the recorded **R**:

$$\mathbf{S} = \mathbf{M}^{-1}\mathbf{R} \equiv \mathbf{D}\mathbf{R}. \tag{3.5}$$

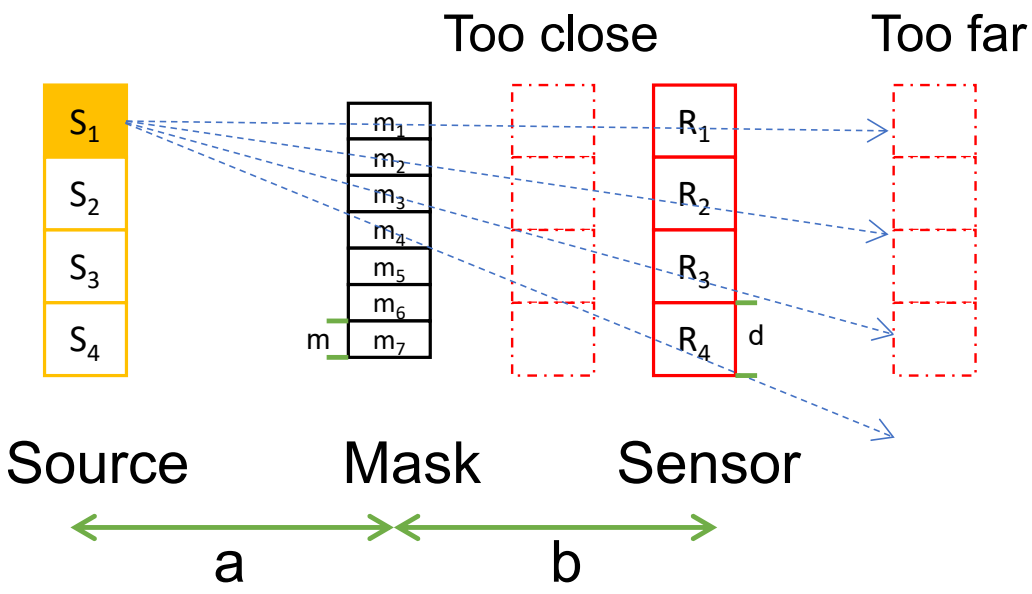

Figure 3.6: This diagram illustrates that the X-ray sensor array has to be at a specific distance from the mask to ensure a one-to-one correspondence between a sensor element and a component of $\mathbf{R}$. a represents the source-to-mask distance. b represents the mask-to-sensor distance. m represents the length of a mask element. d represents the length of a sensor element. Since the triangle $S_1 m_1 m_4$ and the triangle $S_1 R_1 R_4$ are similar, $m/d = a/a+b$ needs to be satisfied to ensure the 1-to-1 correspondence [61].

SNR of an X-ray Image

In practice, the output signal of an X-ray sensor contains noise, so we can only obtain a noisy recorded image. If we denote the noise with a n-dimensional vector $\mathbf{e}$, the noisy image recorded by the X-ray sensor array practically should be $\mathbf{R}+\mathbf{e}$. When we apply the decoding matrix to such a noisy recorded image, we reconstruct a noisy estimate of the source vector $\mathbf{S}$ as

$$\hat{\mathbf{S}} = \mathbf{D}(\mathbf{R}+\mathbf{e}) = \mathbf{S}+\mathbf{De}. \tag{3.6}$$

From the equation above, we can define an SNR as the ratio of the magnitude of signal vector to the root mean square (rms) of the noise vector $\sqrt{\langle \|\mathbf{De}\|^2 \rangle}$:

$$\text{SNR} = \frac{\|\mathbf{S}\|}{\sqrt{\langle \|\mathbf{De}\|^2 \rangle}}. \tag{3.7}$$

For pinhole imaging, $\mathbf{M}$, as shown in Equation (3.3), is a backward identity matrix, so the inverse of $\mathbf{M}$ is also a backward identity matrix. Therefore, the noise vector

is simply

$$\mathbf{De} = \mathbf{M}^{-1}\mathbf{e} = \begin{pmatrix} e_n \\ e_{n-1} \\ \vdots \\ e_2 \\ e_1 \end{pmatrix}. \tag{3.8}$$

If we assume $e_1, e_2, e_3, \cdots, e_n$ are independent and identically distributed random variables with zero mean and σ^2 variance, then the rms of the noise vector is given by

$$\sqrt{\langle \|\mathbf{De}\|^2 \rangle} = \sqrt{n}\sigma. \tag{3.9}$$

Therefore, the SNR for pinhole imaging is simply

$$\mathrm{SNR}_p = \frac{\|\mathbf{S}\|}{\sqrt{n}\sigma}. \tag{3.10}$$

In general, the SNR improvement of a coded aperture mask over a pinhole can be quantified by the ratio below:

$$\frac{\mathrm{SNR}}{\mathrm{SNR}_p} = \frac{\sqrt{n}\sigma}{\sqrt{\langle \|\mathbf{De}\|^2 \rangle}}. \tag{3.11}$$

How to Design a Coded Aperture Mask

We now present a method we followed to design the coded aperture mask. This method was first proposed by Nelson and Fredman [68] for designing a mask pattern that maximizes the SNR ratio in Equation (3.11). More discussions on this method can be found in papers by Haw and Bellan [61], Miyamoto [59], Sloane and Harwit [69], and the references within the three papers above. This method first generates a PN sequence $\{p_1, p_2, p_3, \cdots, p_n\}$ of length $n = 2^k - 1$, where n is the number of sensor elements and k is an integer. The first k elements of this PN sequence are arbitrarily chosen (they have to be either 1 or 0), and the remaining $n - k$ elements are calculated from

$$p_{m+k} = \mod 2 \left(\sum_{i=1}^{k} a_{i-1} p_{m+i-1} \right) \quad (1 \le m \le n-k), \tag{3.12}$$

where a_i is the ith order coefficient of a primitive polynomial (mod 2) of degree k. A table of primitive polynomials (mod 2) for every degree k between 1 and 100 was complied by E.J. Watson [70].

Once the PN sequence with a length of n is obtained, the coded aperture mask pattern is constructed by concatenating 2 periods of the sequence with the last element of the second period omitted. This method results in a mask pattern with $2n$-1 elements. A mask pattern constructed this way will always produce an $n \times n$ mask matrix $\mathbf{M}$ whose first column is the PN sequence. The remaining columns of $\mathbf{M}$ are upward cyclic shifts of the first column vector (for example, $\mathbf{M}$ in Equation [3.2] has this cyclic property).

As an example, we explicitly generate a PN sequence of length $3 = 2^2 - 1$, use the sequence to construct a 5-element mask pattern, and determine the 3×3 mask matrix as follows:

1. We choose the first 2 elements of the sequence to be $p_1 = 1$ and $p_2 = 0$.
2. We identify the coefficients of $x^2 + x + 1$, a primitive polynomial (mod 2) of degree 2, as $a_2 = 1$, $a_1 = 1$, and $a_0 = 1$.
3. Using Equation (3.12), we calculate the third element of the sequence to be $p_3 = 1$. Therefore, the entire PN sequence is $\{1, 0, 1\}$.
4. The corresponding 5-element mask pattern obtained from 2 periods of the PN sequence is $\{1, 0, 1, 1, 0\}$.
5. Placing the PN sequence in the first column of $\mathbf{M}$ and then cyclically shifting the first column upward give us the mask matrix

$$\mathbf{M} = \begin{pmatrix} 1 & 0 & 1 \\ 0 & 1 & 1 \\ 1 & 1 & 0 \end{pmatrix}. \tag{3.13}$$

A cyclic mask matrix $\mathbf{M}$ generated this way is closely related to a Hadamard matrix. A Hadamard matrix is a matrix whose components are either 1 or -1 and whose columns are mutually orthogonal. Because of this relationship, the inverse matrix $\mathbf{D}$ can be obtained by taking the transpose of $\mathbf{M}$ and replacing each 1 with $2/n + 1$ and each 0 with $-2/n + 1$ [59, 68]. Using this method, one can easily calculate and verify that the inverse of the matrix in Equation (3.13) is indeed

$$\mathbf{D} = \frac{1}{2}\begin{pmatrix} 1 & -1 & 1 \\ -1 & 1 & 1 \\ 1 & 1 & -1 \end{pmatrix}. \tag{3.14}$$

The main advantage of using the PN sequence to generate the mask matrix is that the components of **D** can be obtained without any numerical errors associated with matrix inversion.

Since the absolute value of every component of **D** equals $2/n + 1$, we can explicitly calculate the noise vector as

$$\mathbf{De} = \frac{2}{n+1}\begin{pmatrix} \sum_i \pm e_i \\ \sum_i \pm e_i \\ \vdots \\ \sum_i \pm e_i \end{pmatrix}, \tag{3.15}$$

where the plus and minus signs depend on the signs of the components of **D**, but these signs will not affect the rms calculation. One can verify that the rms of the noise vector is

$$\sqrt{\langle \|\mathbf{De}\|^2 \rangle} = \frac{2n\sigma}{n+1}. \tag{3.16}$$

Therefore, the SNR improvement of this mask over a single pinhole is

$$\frac{\mathrm{SNR}}{\mathrm{SNR}_p} = \frac{n+1}{2\sqrt{n}}. \tag{3.17}$$

For a large n, the signal-to-noise improvement roughly equals $\sqrt{n}/2$. For example, if $n = 63$, then the SNR improvement is roughly 4.

Unfortunately, the PIN-diode-based X-ray sensor arrays has $n = 50$ X-ray sensor elements, so we need a 50-element sequence. Because $50 \neq 2^k - 1$, the procedure presented above cannot be directly applied. To construct a 50-element sequence, we first constructed a PN sequence with $2^6 - 1 = 63$ elements. We then took the first 50 elements of the PN sequence to construct a coded aperture mask pattern with $2 \times 50 - 1 = 99$ elements. For reference, we explicitly type out the 50-element sequence here:

$$\{1, 1, 1, 1, 1, 1, 0, 1, 0, 1, 0, 1, 1, 0, 0, 1, 1, 0, 1, 1, 1, 0, 1, 1, 0,$$
$$1, 0, 0, 1, 0, 0, 1, 1, 1, 0, 0, 0, 1, 0, 1, 1, 1, 1, 0, 0, 1, 0, 1, 0, 0\}.$$

This sequence will result in a 50×50 mask matrix **M** that is still cyclic, but the components of its inverse no longer have the same absolute value. Thus the inverse matrix needs to be calculated numerically. The SNR improvement ratio of this matrix calculated numerically from Equation (3.11) is roughly 2. This is a factor of 2 lower than the maximum improvement guaranteed by Equation (3.17).

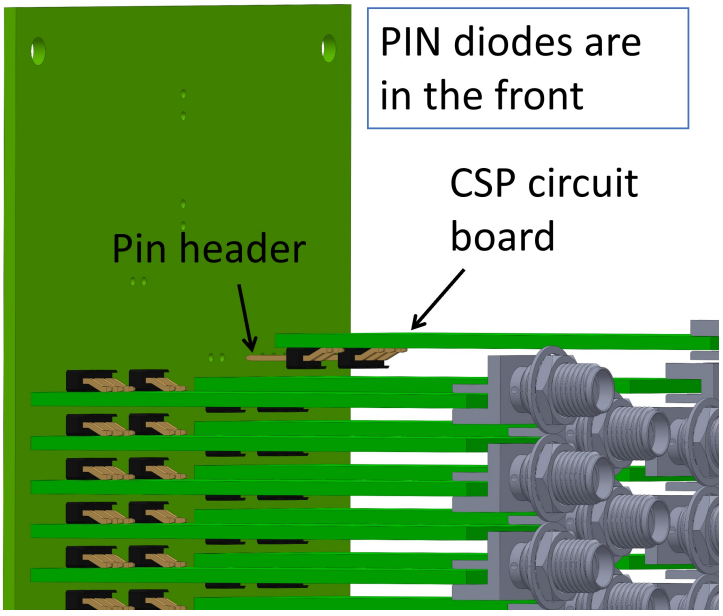

Figure 3.7: This figure shows that a charge-sensitive preamplifier (CSP) circuit board is connected to the front circuit board via pin headers.

3.5 PIN-Diode-Based X-ray Sensor Array

The PIN-diode-based X-ray sensor array is composed of 50 reverse-biased PIN diodes (OSRAM SFH 2700), originally intended for visible light detection, on a 2.54 mm pitch. Each PIN diode has a radiant sensitive area of 0.35 mm^2 that can absorb the energy of an incident X-ray photon and release electron hole pairs with a conversion ratio of 3.6 eV/pair [71, 72]. These electron hole pairs are accelerated by an electric field in the depletion region of the PIN diode and produce a photocurrent.

These PIN diodes are coupled via pin headers to 50 charge-sensitive preamplifiers (CSPs), as shown in Figure 3.7. Since the CSPs are located near the noisy plasma jet experiment, a heavy-duty aluminum box is used to shield the CSPs from the unwanted electromagnetic interference from the plasma jet experiment.

A simplified circuit diagram of the CSP is shown in Figure 3.8. The charge carriers generated by a PIN diode accumulate onto the feedback capacitor of the CSP. This feedback capacitor converts the input charge to a voltage signal. The second-stage shaping amplifier then amplifies and reshapes the voltage signal to a detectable voltage pulse. The width of this voltage pulse is typically less than 1 µs, and the amplitude of this voltage pulse is proportional to the charge accumulated onto the feedback ca-

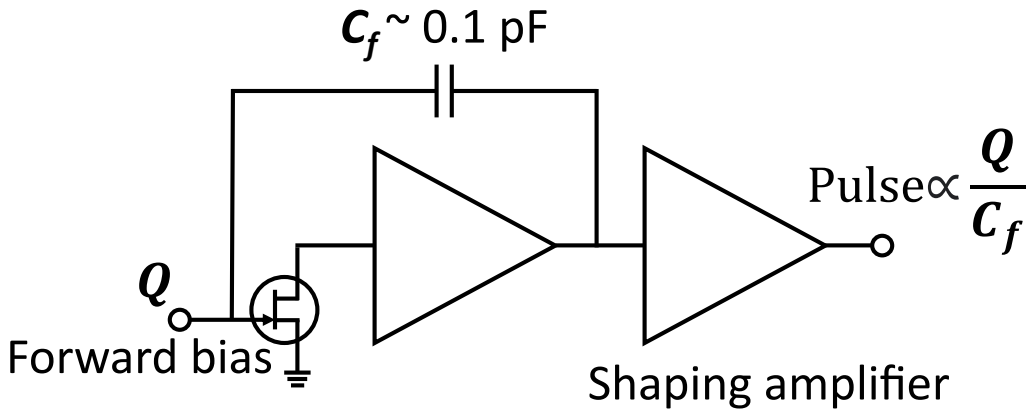

Figure 3.8: A simplified circuit diagram of the charge-sensitive preamplifier. This circuit consists two stages. The first stage uses a feedback capacitor to convert an input charge signal to a voltage signal. The second stage amplifies the voltage signal and reshapes the signal to a fast voltage pulse. The amplitude of the pulse is proportional to the input charge and inversely proportional to the feedback capacitance. The gate-source junction of the input JFET is slightly forward biased so that the feedback capacitor can discharge through this junction. The novelty of this discharge mechanism is that it does not require a feedback resistor.

pacitor and inversely proportional to the feedback capacitance. Unlike conventional CSPs that use a large feedback resistor to discharge the feedback capacitor, this novel CSP discharges the feedback capacitor through a slightly forward-biased gate-source junction of the input n-channel JFET. This discharge mechanism eliminates the unwanted noise associated with a large feedback resistor. Appendix B contains more details about the CSP circuit for readers who are interested in understanding how the circuit works.

The PIN-diode-based X-ray sensors have been tested to be sensitive to individual 6 keV photons from a radioactive ^{55}Fe source as shown in Figure 3.9.

Figure 3.10 shows a simplified circuit of the 50-channel PIN-diode-based X-ray sensor array. The CSPs are placed in left-and-right pattern so that CSPs connected to successive PIN diodes, such as D_1 and D_2, do not touch each other. This left-and-right pattern enables us to pack 50 sensor pixels (only 25 sensor pixels can be packed if all CSPs are simply stacked in a single column on the left or right) in a 5-inch 1D X-ray sensor array. More sensor pixels are particularly useful for producing X-ray images with a good spatial resolution. For reference, Figure 3.11 shows the front and the back of a SolidWorks model of the X-ray sensor array.

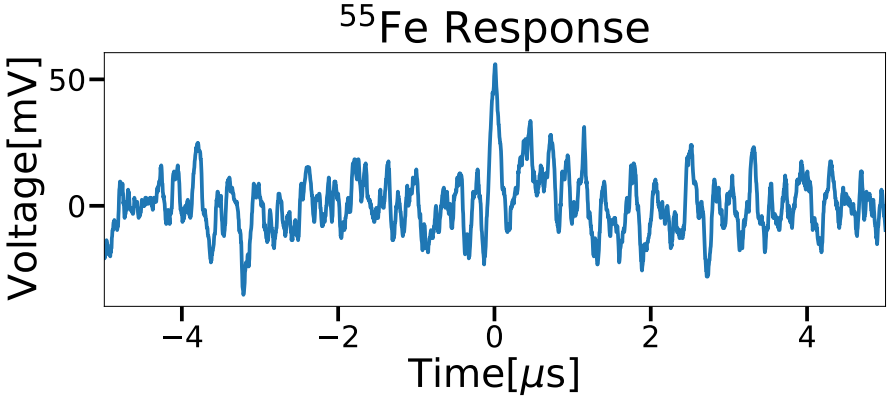

Figure 3.9: Output voltage trace of the charge-sensitive preamplifier circuit measured by an oscilloscope. The voltage spike at 0 µs corresponds a single 6 keV photon from a ^{55}Fe radioactive source.

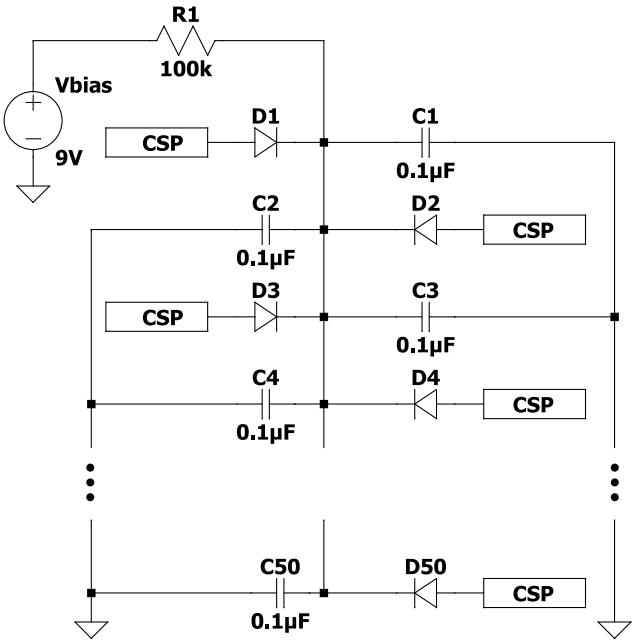

Figure 3.10: Simplified circuit for the 50-channel PIN-diode-based X-ray sensor array. The charge-sensitive preamplifiers (CSPs) are placed in a left-and-right pattern so that the vertical distance between CSPs connected successive PIN diodes, such as D_1 and D_2, can be as close as possible. This left-and-right pattern allows packing twice as many CSPs as a simple linear pattern does in a given vertical range.

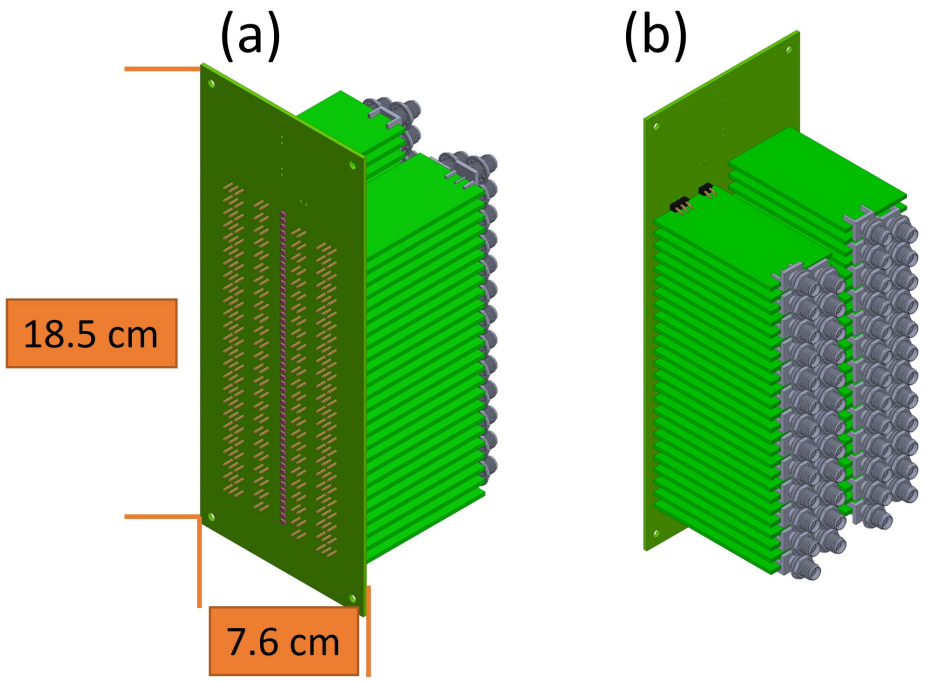

Figure 3.11: (a) and (b) show the front and the back of a SolidWorks model of the PIN-diode-based X-ray sensor array respectively.

A bypass capacitor, such as C_1, is connected to each PIN diode, such as D_1, to provide a low-impedance path to ground for AC signal from the bias voltage source V_{bias}, resulting in a clean DC bias voltage. V_{bias} is provided by a 9V battery. Applying a 9 V reverse bias voltage noticeably reduces the output voltage noise of each X-ray sensor. For example, Figure 3.12 shows that the 9 V reverse bias voltage lowers the standard deviation of the output voltage of channel 1 of the X-ray sensor array from 14 mV to 9 mV.

Uniformity in Responsivity

The responsivity for each channel of the PIN-diode-based X-ray sensor array is defined as the ratio of the amplitude of the output voltage pulse to the intensity of incident radiation. When these channels receive the same amount of incident radiation, each channel should ideally generate the same voltage pulse. Thus, each channel should ideally have identical responsivity. Figure 3.13 shows the relative responsivity of each channel to an ^{241}Am radioactive source. From the figure, we can see that each channel has a similar responsivity. The 50 discrete data points (one for each channel) in Figure 3.13 are connected by solid lines solely for the ease of viewing. To generate these 50 data points, an average voltage trace for each

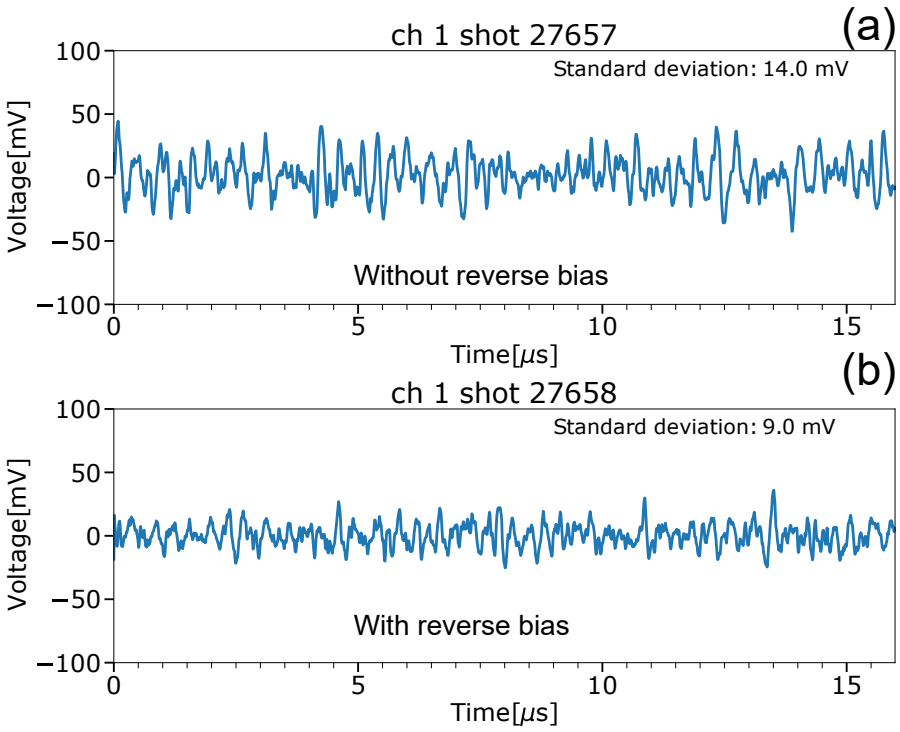

Figure 3.12: (a) shows the output voltage noise of channel 1 of the X-ray sensor array without any reverse bias voltage. (b) The output voltage noise is reduced after the 9 V reverse bias voltage is applied.

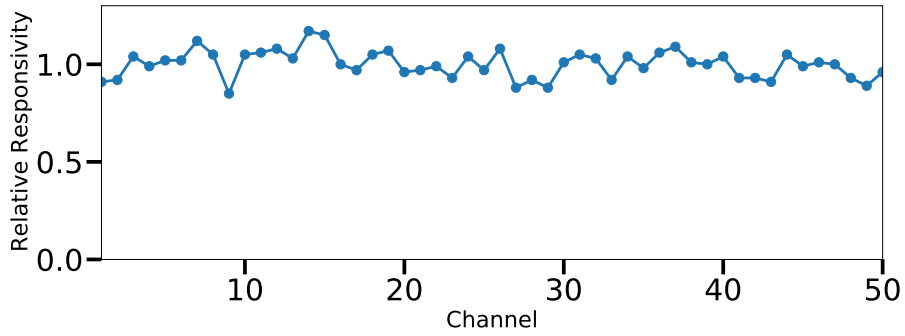

Figure 3.13: The relative responsivity of each channel of the PIN-diode-based X-ray sensor array to an ^{241}Am radioactive source. The solid lines that connect the 50 discrete data points (one data point for each channel) do not have any physical meaning. The responsivity is reasonably uniform across all 50 channels.

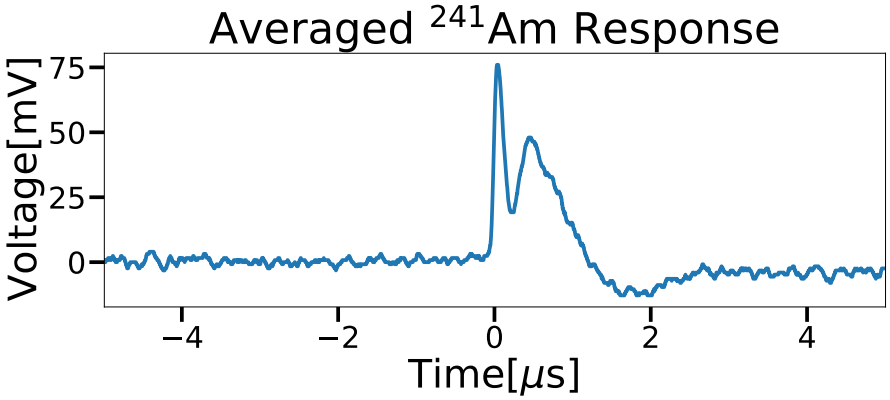

Figure 3.14: An 64-sample-averaged voltage trace that corresponds to the response of a PIN-diode-based X-ray sensor to a single photon from an ^{241}Am radioactive source. The averaging is done by an digital oscilloscope. An unwanted smaller pulse occurs right after the spike at 0 µs. How to remove this unwanted pulse is discussed in Section 3.7.

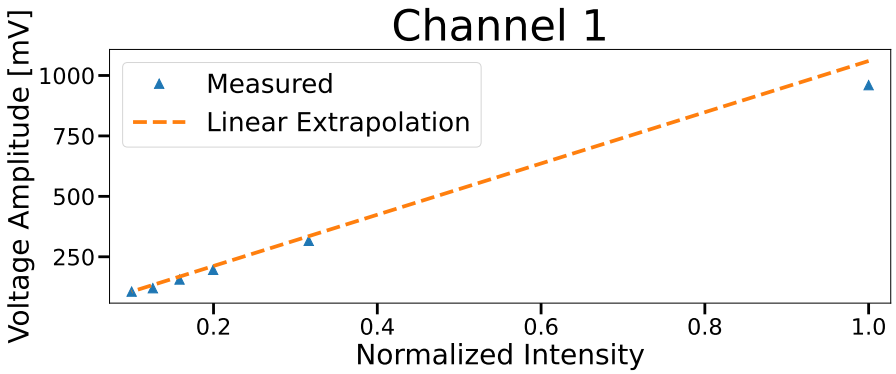

Figure 3.15: This plot demonstrates that the amplitude of the voltage pulse of an X-ray sensor increases linearly with the intensity of incident radiation. Similar plots are obtained for all 50 channels of the X-ray sensor array.

channel was acquired by a digital oscilloscope (the oscilloscope saved 64 traces in the memory and averaged them). An example of the averaged voltage trace is shown in Figure 3.14. Each data point in Figure 3.13 represents an amplitude of the corresponding voltage trace normalized by the mean amplitude of all 50 voltage traces.

Linearity in Responsivity

The pulse amplitudes of all 50 channels have been measured to be linear with the intensity of input radiation. For example, the measurements for channel 1 are shown in Figure 3.15. The setup in Figure 3.16 shows how these measurements were

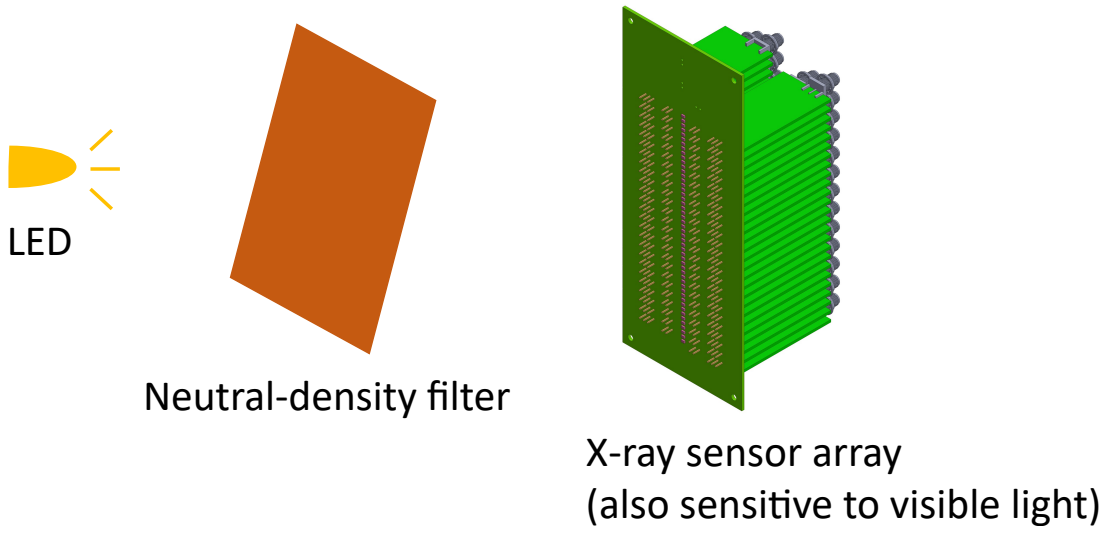

Figure 3.16: The incident radiation used for the linearity measurement is the visible light emitted from a light-emitting diode (LED). The intensity of the light is adjusted by ND filters with different optical densities, so that we can measure the pulse amplitude of an X-ray sensor as a function of the intensity of incident radiation.

obtained: the incident radiation was emitted from a light-emitting diode (LED), and a neutral density (ND) filter with an optical density d was placed between the LED and the X-ray sensor array to reduce the intensity of radiation that reached the X-ray sensor array. For an ND filter with optical density d, the fraction of the light intensity that transmits through the ND filter is given by 10^{-d}. Thus, the light intensity seen by the X-ray sensor array was varied by using ND filters with different optical densities.

3.6 Testing Coded Aperture Imaging Visible Light

A high-power LED that generates $\sim$ 100 µs visible light pulses was used to test the coded aperture imaging method with the PIN-diode-based camera. Figure 3.17 shows the setup of the test. An aluminum plate with two square holes masked the high-power LED to make two localized visible light sources that were separated by 1.27 cm (see Figure 3.18). These light sources were covered by two layers of Kapton sheets so that the visible light signals did not saturate the PIN-diode-base sensors. The coded aperture mask showed in Figure 3.4 was placed around 80 cm away from the light sources to project an image onto the PIN diodes. The distance between the PIN diodes and the coded aperture mask was 32 cm.

Figure 3.19 shows a raw image recorded by the coded aperture camera and the

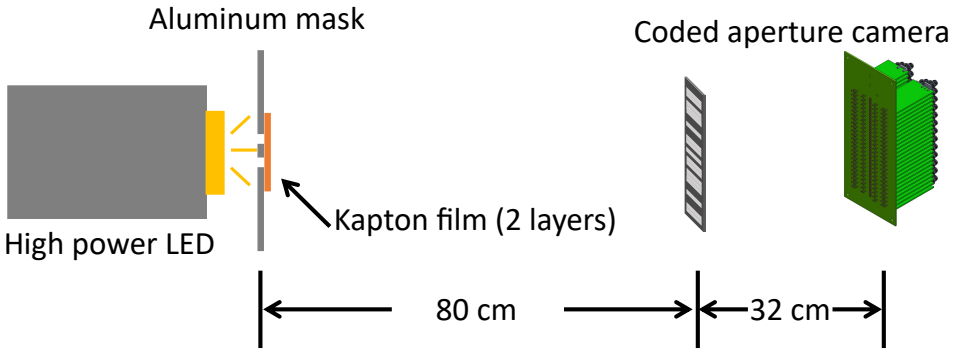

Figure 3.17: This diagram shows the setup of the visible light imaging test. The high-power light-emitting diode (LED) in the diagram generates a ~ 100 μs visible light pulse roughly every 200 μs. Two transient, localized light sources that are separated by 1.27 cm are created by masking the high-power LED with an aluminum plate. The visible light sources are attenuated by two layers of Kapton sheet so that the visible light signals do not saturate the PIN diodes.

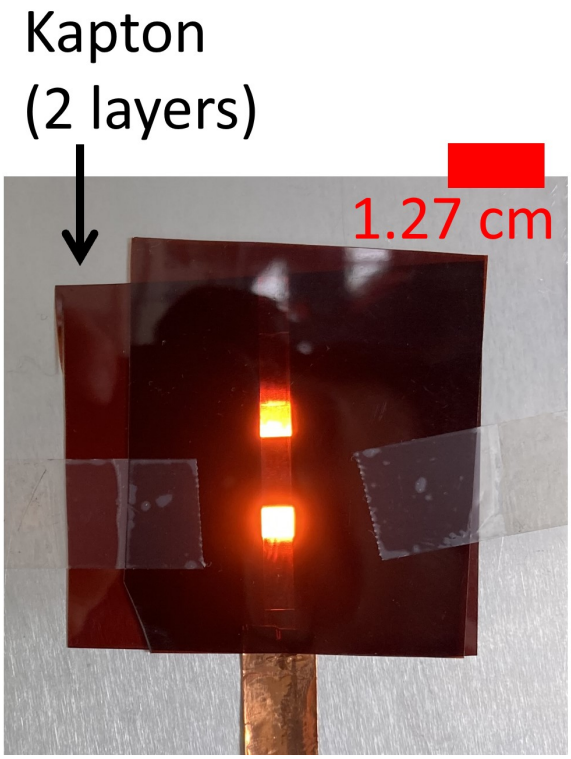

Figure 3.18: A photo of the two (pulsed) visible light sources being imaged.

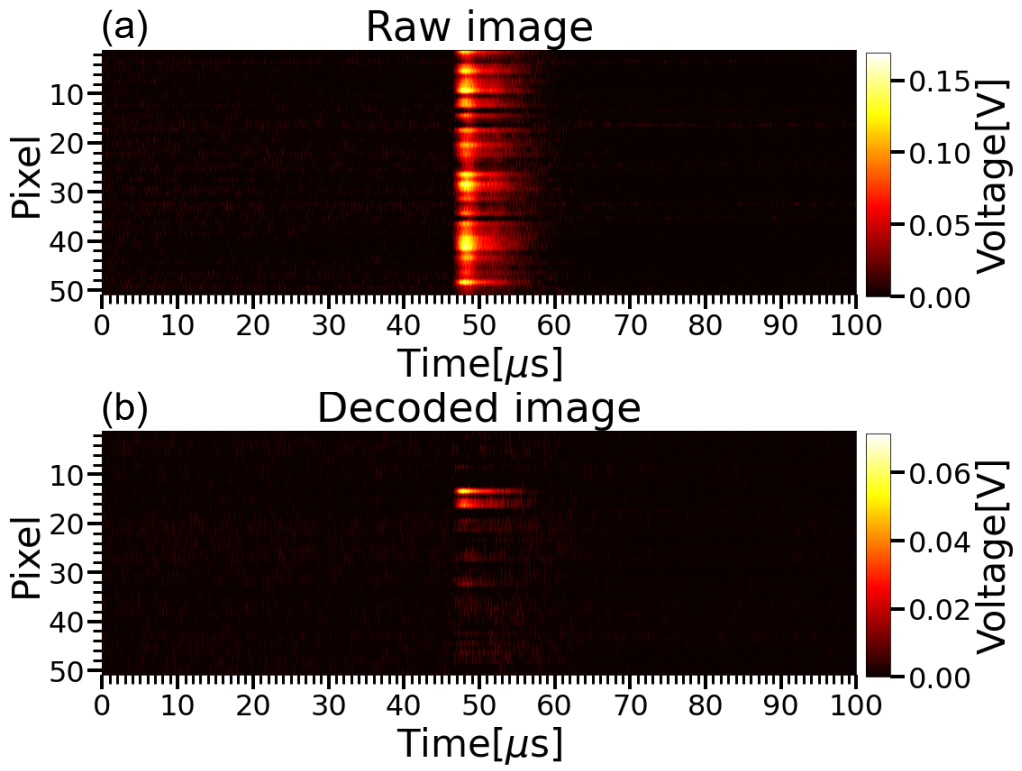

Figure 3.19: (a) shows a raw image recorded by the coded aperture camera. (b) shows the corresponding decoded image of the two visible light sources shown in Figure 3.18.

corresponding decoded image. The decoded image shows two bright stripes that agree well with the two visible light sources shown in Figure 3.18. The bright stripes in Figure 3.19 only last around $\sim$ 8 µs because these bright stripes only correspond to the rising edge of the 100 µs visible light pulse. The reason that the PIN-diode sensors could only respond to the rising edge but not to the flat part of the light pulse is because the sensors have very little gain at low frequency (see Figure B.18).

3.7 Richardson-Lucy Deconvolution

Figure 3.14 shows that the response of the X-ray sensor to an incident X-ray photon has a two-pulse structure: a smaller pulse occurs immediately after an initial spike. Ideally, the response should be a single delta-function-like pulse, and this unwanted second pulse lowers the time resolution of the X-ray sensor. This section describes a procedure to remove this unwanted pulse.

Conceivably, we can imagine there exists a linear transformation that transforms an ideal delta-function-like response to the imperfect two-pulse response. To model

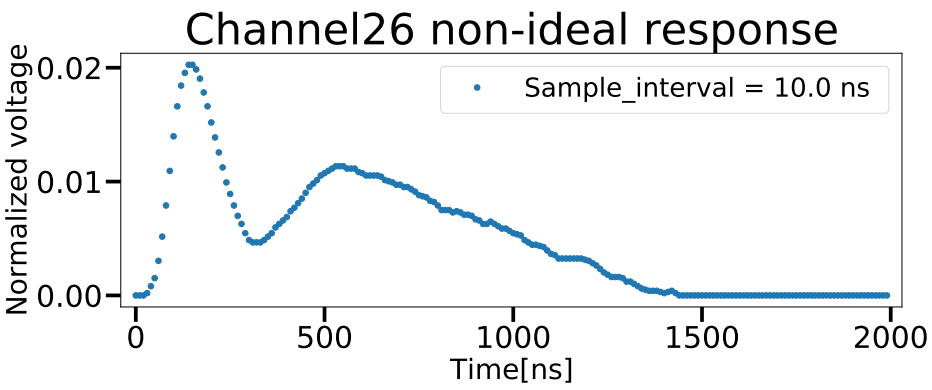

Figure 3.20: The imperfect time response of the 26th channel of the X-ray sensor array to an ^{241}Am radioactive source re-sampled at 100 MHz (the time step for discretization is Δt = 10 ns). The re-sampling is done using a one-dimensional linear interpolation. The original signal was obtained from a fast oscilloscope with a 250 MHz sampling rate. Negative voltages have been set to zero. The voltages are normalized such that the area under the voltage curve equals 1.

this transformation process, we can first discretize time with a small time interval Δt. We use i to index time, so $t_i = i\Delta t$. In this discretized time space, we can represent a voltage signal as a vector whose jth component corresponds to the voltage value at t_{j-1}. Specifically, the first component of the vector corresponds to the voltage value at $t = 0$.

If a photon hits the PIN-diode at time $t = 0$, we could represent the ideal voltage response with a standard basis vector $\hat{\mathbf{e}}_1$ (this vector has 1 in its 1st coordinate and 0s elsewhere). The transformation we are trying to model essentially "spreads out" $\hat{\mathbf{e}}_1$ and produces an imperfect two-pulse vector. Thus, the transformation process can be written as a matrix equation

$$\mathbf{d} = \mathbf{P}\hat{\mathbf{e}}_1, \tag{3.18}$$

where $\mathbf{P}$ is the matrix that represents the non-ideal linear transformation, and $\mathbf{d}$ is a vector that corresponds to an imperfect two-pulse response that starts rising at $t = 0$.

$\mathbf{d}$ can be obtained experimentally, and we can further process the experimental data such that $\mathbf{d}$ satisfies

$$\sum_i d_i = 1 \quad \text{and} \quad d_i \geq 0. \tag{3.19}$$

For example, the response of the 26th channel of the X-ray sensor array to the ^{241}Am source shown in Figure 3.20 can be treated as $\mathbf{d}$. Equation (3.18) shows that the 1st column of matrix $\mathbf{P}$ is $\mathbf{d}$. By a similar argument, the jth column of $\mathbf{P}$ should

be the same imperfect two-pulse response that starts rising at $t = (j-1)\Delta t$. More precisely, the components of $\mathbf{P}$ are defined as

$$P_{ij} = d_{i-j+1}, \tag{3.20}$$

where $P_{ij} = 0$ if $i < j - 1$. Thus, $\mathbf{P}$ is a lower triangular matrix, and $\mathbf{P}$ can be represented as

$$\mathbf{P} = \begin{pmatrix} d_1 & 0 & 0 & \cdots & 0 \\ d_2 & d_1 & 0 & \cdots & 0 \\ d_3 & d_2 & d_1 & \cdots & \vdots \\ \vdots & \vdots & \vdots & \cdots & d_1 \end{pmatrix} \tag{3.21}$$

in matrix form.

In general, multiple photons can hit the PIN diode at different times, so we expect $\mathbf{P}$ to transform a linear combination of delta-function-like pulses to a recorded voltage signal $\mathbf{m}$:

$$\mathbf{m} = \mathbf{P}\mathbf{u}, \tag{3.22}$$

where $\mathbf{u} = \sum u_j \hat{\mathbf{e}}_j$ is the linear combination. Therefore, given an invertible $\mathbf{P}$ and a noiseless $\mathbf{m}$, we can in principal reconstruct the original delta-function-like pulses by solving matrix Equation (3.22) exactly.

In practice, $\mathbf{P}$ could be either singular or ill-conditioned. Furthermore, $\mathbf{m}$ is typically recorded with some noise or errors. Thus, a satisfactory solution to Equation (3.22) could be impossible to obtain. If this is the case, we hope to obtain a good estimate for $\mathbf{u}$ (called $\hat{\mathbf{u}}$) so that $\mathbf{P}\hat{\mathbf{u}}$ is close to the noiseless $\mathbf{m}$, i.e.,

$$\mathbf{m} \approx \mathbf{P}\hat{\mathbf{u}}. \tag{3.23}$$

One algorithm that suppresses high-frequency noise and effectively approximates $\mathbf{u}$ is the Richardson–Lucy deconvolution algorithm [73, 74]. This iterative algorithm was proposed by Richardson to restore noisy images that are degraded by point spread functions. Lucy independently proposed the algorithm to solve deconvolution problems in statistical astronomy.

The Richardson–Lucy deconvolution starts with an initial guess $\hat{\mathbf{u}}^{(0)}$ and iteratively improves the guess. For iteration number t, the update on $\hat{\mathbf{u}}^{(t)}$ is calculated as follows:

$$\hat{u}_j^{(t+1)} = \hat{u}_j^{(t)} \sum_i \frac{m_i}{c_i} P_{ij}, \tag{3.24}$$

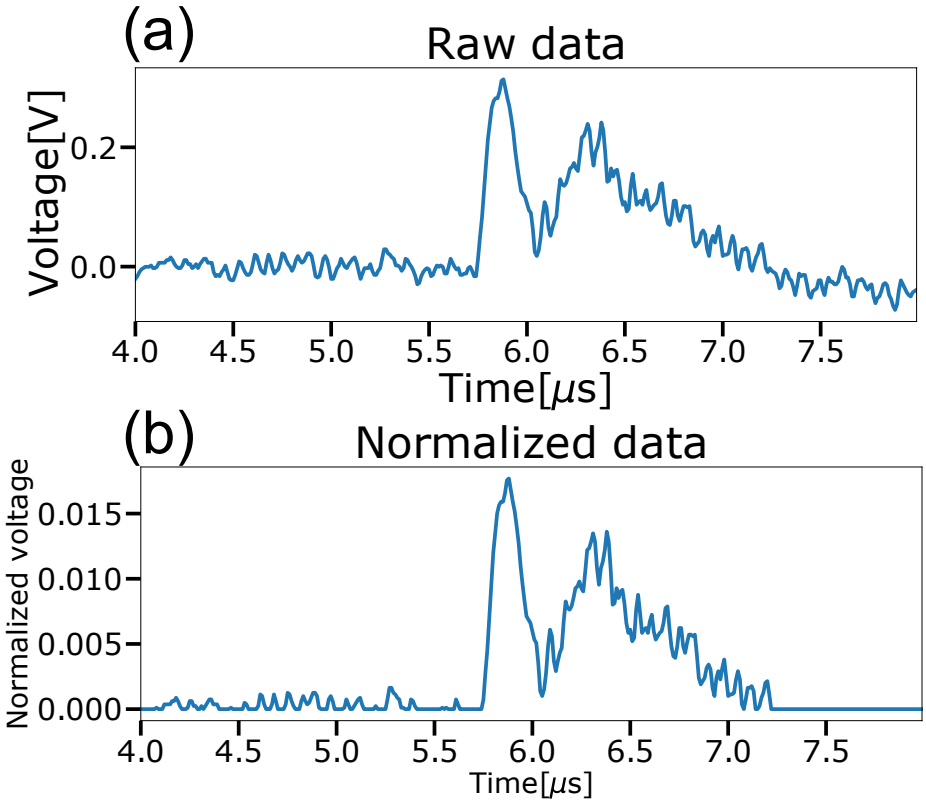

Figure 3.21: (a) shows a noisy X-ray signal from the plasma jet experiment (shot 30455). This signal has a non-ideal two-pulse waveform. (b) shows the normalized data for Richardson-Lucy algorithm.

where

$$c_i = \sum_j P_{ij} \hat{u}_j^{(t)}. \tag{3.25}$$

It can be proved that if $\hat{\mathbf{u}}^{(0)}$ satisfies the normalization and non-negativity constraints in Equation (3.19), then $\hat{\mathbf{u}}^{(t+1)}$ also satisfies those constraints. This iterative method has been empirically shown to arrive at a good solution to Equation (3.23) after a few iterations.

To demonstrate this deconvolution algorithm, we use noisy X-ray data, shown in Figure 3.21, from the plasma jet experiment. Negative voltages in the original data in Figure 3.21(a) are set to zero, and then the data is normalized such that the time-integrated voltage is 1. The resulted data shown in Figure 3.21(b) are used as $\mathbf{m}$ for the deconvolution.

To start the algorithm, the initial guess for $\hat{\mathbf{u}}$ is set to be a uniform distribution, i.e.,

$$\hat{u}_i = \frac{1}{\sum_j \hat{u}_j}, \quad \text{for all } i. \tag{3.26}$$

Figure 3.22 shows the resulted $\hat{\mathbf{u}}$ after different numbers of iterations. After just one iteration, the high-frequency voltage fluctuation due to electronic noise is smoothed out. After 10 iterations, the unwanted pulse around $t = 6.5$ µs in Figure 3.22 is significantly suppressed, and only a single peak between $t = 5.5$ µs and $t = 6$ µs remains. After about 20 iterations, the algorithm has generated a reasonably good $\hat{\mathbf{u}}$. The width of the pulse is only $\sim$ 100 ns. Further iterations slightly increase the amplitude of the peak, but these iterations do not significantly improve the approximation.

Figure 3.23 shows a noisy X-ray image and its associated restored image using the deconvolution algorithm. How the X-ray image was taken and how to interpret the image will be discussed in more detail in Chapter 4. Here, we mainly discuss how the deconvolution algorithm is implemented to improve the image quality. The bright strip in the middle of Figure 3.23(a) corresponds to X-ray signals recorded by the 25th and the 26th channels of the X-ray sensor array. Thirty iterations of the deconvolution algorithm are applied to the voltages on these 2 channels to reconstruct the bright spot in Figure 3.23(b). Comparing Figure 3.23(a) and Figure 3.23(b), we see that the duration of the X-ray signal has been reduced from around 1 µs to 100 ns. Voltages in all other channels are manually set to zero because these voltages are either electronic noise or errors introduced by electromagnetic interference or crosstalk.

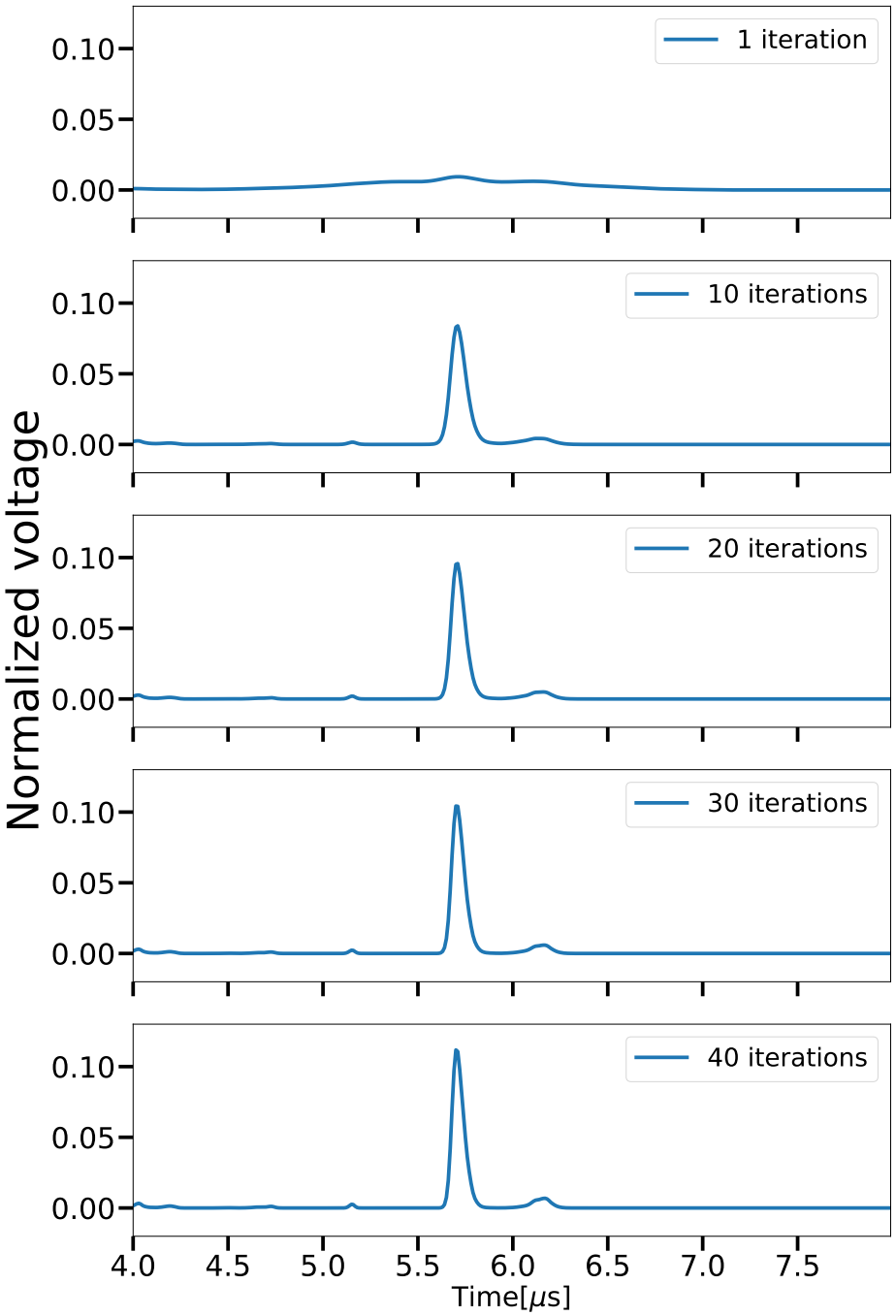

Figure 3.22: This figure shows the results of the Richardson-Lucy deconvolution after different numbers of iterations. The delta-function-like pulses between $t = 5.5$ µs and $t = 6$ µs are reconstructed from normalized data in Figure 3.21(b). The width of this pulse is ~100 ns. The initial guess for the algorithm is a uniform distribution defined in Equation (3.26).

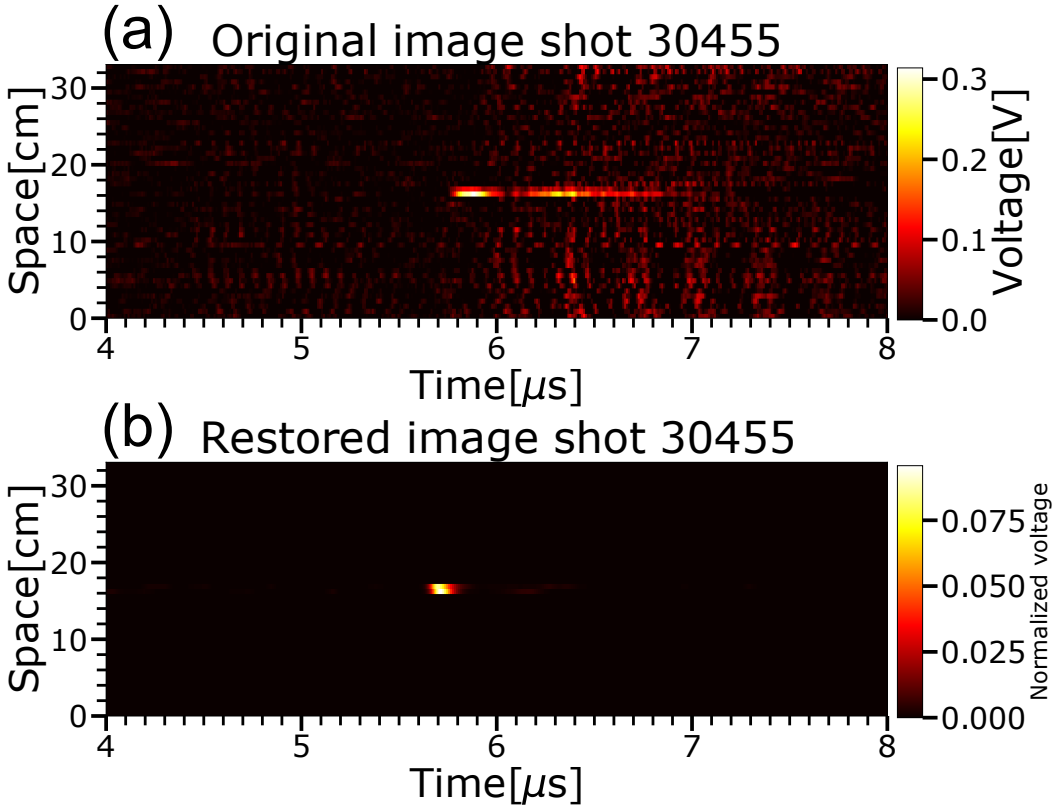

Figure 3.23: (a) shows a noisy X-ray pinhole image from the plasma jet experiment. The bright strip in the middle corresponds to non-ideal pulses recorded by two channels of the X-ray sensor array. More details on how this image was taken can be found in Chapter 4. (b) shows a restored image using 30 iterations of the Richardson-Lucy deconvolution algorithm. The algorithm is only applied to the two channels that contain X-ray signals. Voltages on the other channels are manually set to zero. The Richardson-Lucy algorithm successfully reduced the duration of the X-ray image from around 1 µs to 100 ns.

Chapter 4

MEASURING X-RAYS FROM THE CALTECH PLASMA JET EXPERIMENT

[1] Y. Zhou, S. Pree, and P. M. Bellan. "Imaging suprathermal x-rays from a laboratory plasma jet using PIN-diode-based and scintillator-based 1D pinhole/coded aperture cameras". In: *Review of Scientific Instruments* 94 (2023), p. 013504. DOI: 10.1063/5.0122760.

This chapter describes how the PIN-diode-based X-ray camera has been utilized to produce time-resolved X-ray images of the transient, low-intensity, and suprathermal X-rays produced in two different experimental configurations of the plasma jet experiment. In addition, how the PIN-diode-based X-ray camera is reconfigured to measure the X-ray energy is also described.

4.1 X-rays from the Plasma Jet Experiment

Depending on the bias magnetic flux generated by the coil located behind the inner electrode, two different plasma configurations that generate ~6 keV suprathermal X-rays have been found. These two configurations will be referred to as the low-flux (LF) configuration and the high-flux (HF) configuration. Figure 4.1 shows the typical X-ray signals from these configurations. These signals are detected by a scintillator X-ray detector located inside the vacuum chamber. X-rays from the LF configuration tend to be intense and highly reproducible. In contrast, the X-rays from the HF configuration have a lower intensity and appear sporadically in a ~ 20 μs time window. As a result, X-rays from the HF configuration are significantly more difficult to image.

The suprathermal X-rays are typically produced when the plasma jet is affected by magnetohydrodynamic (MHD) instabilities which are shown in the visible light photos in Figure 4.2. Details about these MHD instabilities and X-ray measurements have been published in previous papers [14, 15, 16, 18]. Figure 4.2(a) shows that a plasma jet in the LF configuration is locally pinched by a sausage-like instability [16] at approximately 5 cm away from the center of the electrode around 5 μs after plasma breakdown. Figure 4.2(b) shows that the column of a plasma jet in the HF configuration is constricted by a periodic kink-instigated Rayleigh-Taylor (RT)

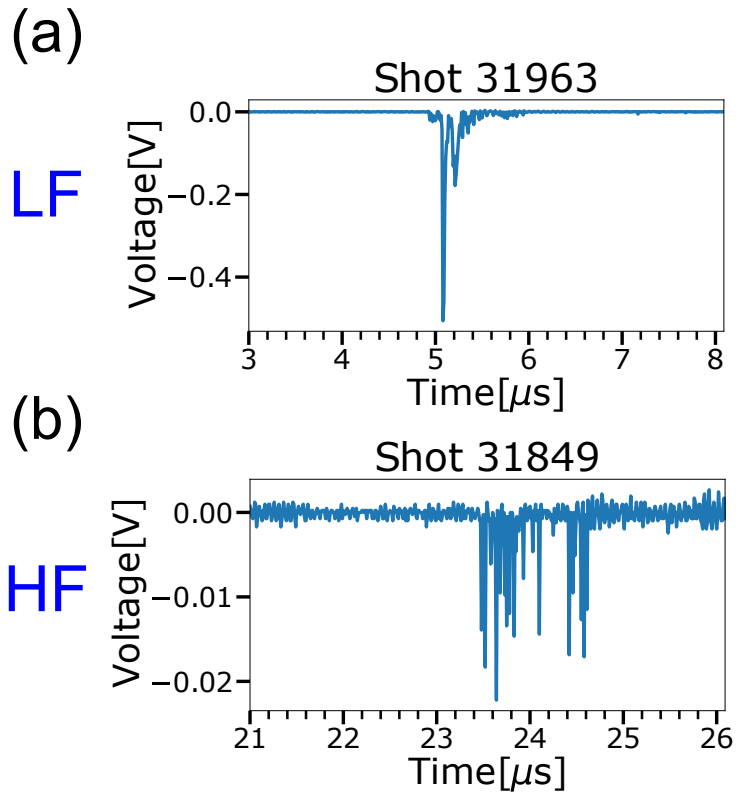

Figure 4.1: (a) shows a typical X-ray signal from the low-flux (LF) configuration. This X-ray signal is strong and highly reproducible. (b) shows a typical X-ray signal from the high-flux (HF) configuration. This X-ray signal is weaker and tends to appear sporadically in a ∼ 20 µs time window. The weaker intensity and lower reproducibility of this X-ray signal make imaging X-rays from the HF configuration more challenging.

instability [18, 14, 15] around 30 µs after breakdown. The constricted region is roughly 10–15 cm away from the electrode and occupies a 10 cm × 10 cm area. The time at which the RT instability occurs and the constricted location vary from shot to shot. Because X-rays are typically detected during these MHD instabilities, one would naturally expect that X-rays are emitted from these instability regions. However, some other unexpected locations of the X-ray sources have been revealed by X-ray images that will be presented in this chapter.

4.2 Image X-rays from the Experiment

Figure 4.3 shows the setup for imaging X-rays from the plasma jet experiment. The PIN-diode-based X-ray camera and the fast framing camera are on opposite sides of the plasma jet so that visible light and X-rays from the experiment can be imaged

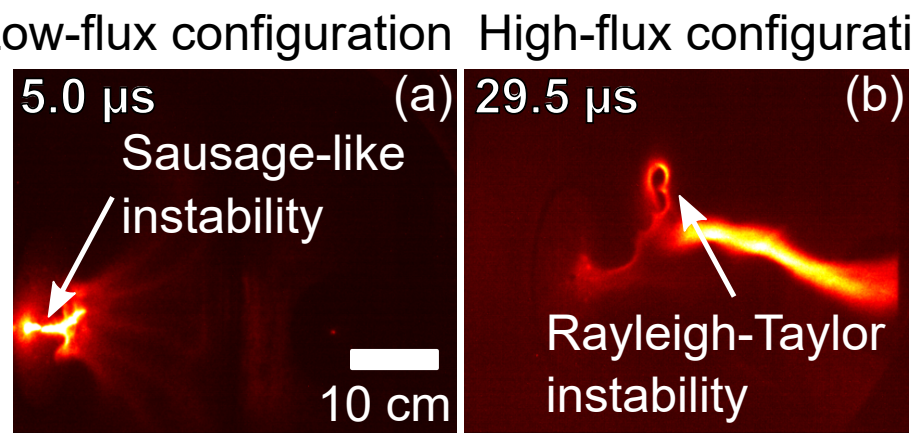

Figure 4.2: False color images showing the instabilities formed in plasma jets in the (a) low-flux and the (b) high-flux configurations. The plasma jet in the low-flux configuration is locally pinched by a sausage-like instability at approximately 5 cm away from the center of the electrode around 5 μs after breakdown. The column of the plasma jet in the high-flux configuration is constricted by a periodic kink-instigated Rayleigh-Taylor instability around 30 μs after breakdown. The constricted region is roughly 10–15 cm away from the electrode and occupies a 10 cm × 10 cm area. Determining whether X-rays are generated from these instability regions is the main motivation for imaging X-rays in this experiment.

simultaneously. The scintillator-photomultiplier X-ray detector inside the vacuum chamber provides an independent validation for the X-ray signal seen by the X-ray camera.

Because the 1D X-ray sensor array can only resolve X-rays along one direction at a time, we oriented the array horizontally and then vertically to locate the source of the X-rays from the Caltech plasma jet experiment in two dimensions. The pinhole-to-plasma distance was fixed to be approximately 80 cm, while the pinhole-to-array distance was varied between 16 cm and 40 cm to adjust the size of the field of view (FOV). An example of the horizontal arrangement is depicted in Figure 4.4.

In the horizontal orientation, only pinhole images were successfully captured. The best images were captured using a long and narrow rectangular pinhole, so the camera also had a large vertical FOV. However, the horizontally placed 1D array could not resolve the vertical position of the X-ray source. In the vertical arrangement both coded apertures and pinhole images were successfully captured. For comparison purposes, the size of a pinhole was set to be equivalent to that of a single coded aperture element. To help visualize the FOVs in both horizontal and vertical orien-

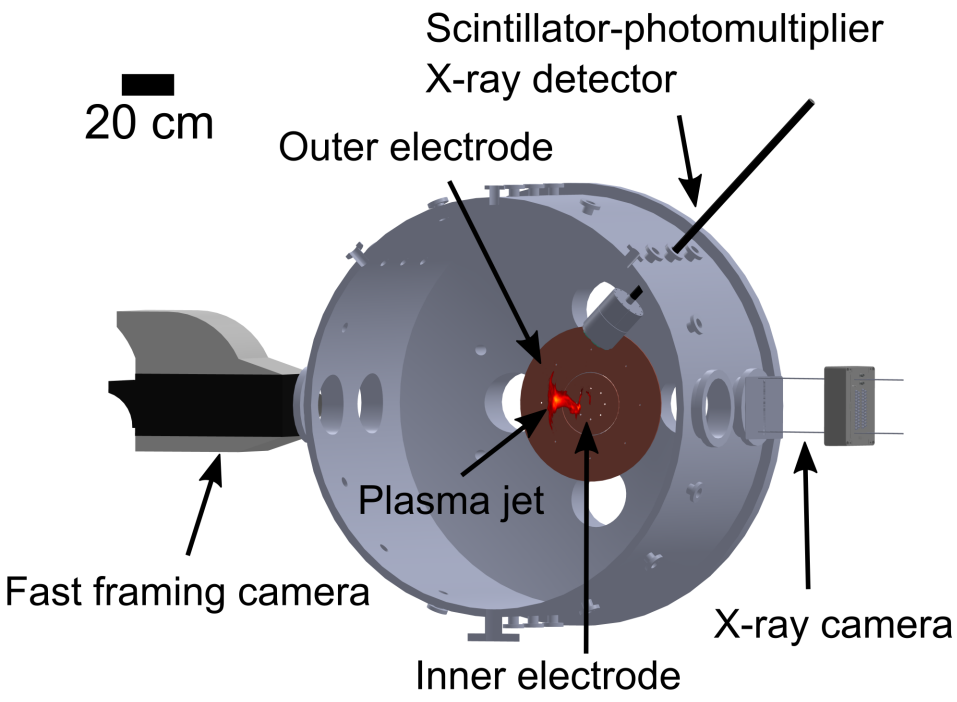

Figure 4.3: The PIN-diode-based X-ray camera on the right images X-rays, while the fast framing camera on the left images visible light. The scintillator-photomultiplier X-ray detector inside the vacuum chamber validates the X-ray signal seen by the X-ray camera, but the X-ray detector does not have an imaging capability.

tations, two examples of the FOVs are represented by green and blue dashed boxes in a visible light photo of the plasma jet in Figure 4.5.

Horizontal Pinhole Images

Figure 4.6 shows two horizontal pinhole images taken by the PIN-diode-based X-ray camera. Figure 4.6(a) is for the LF configuration, and Figure 4.6(b) is for the HF configuration. They are presented as streak images with the vertical axis being the time axis and the horizontal axis being the space axis. Output voltages from the X-ray sensor pixels are mapped to colors in the images. Time zero corresponds to plasma breakdown, and the right end of an image roughly corresponds to the location of the inner electrode. Both images show that X-rays are emitted a few centimeters away from the inner electrode. Compared to the visible light photos of the plasma jet shown in Figure 4.2, we see that this close-to-electrode X-ray source likely coincides with the location of the sausage-like instability in the LF

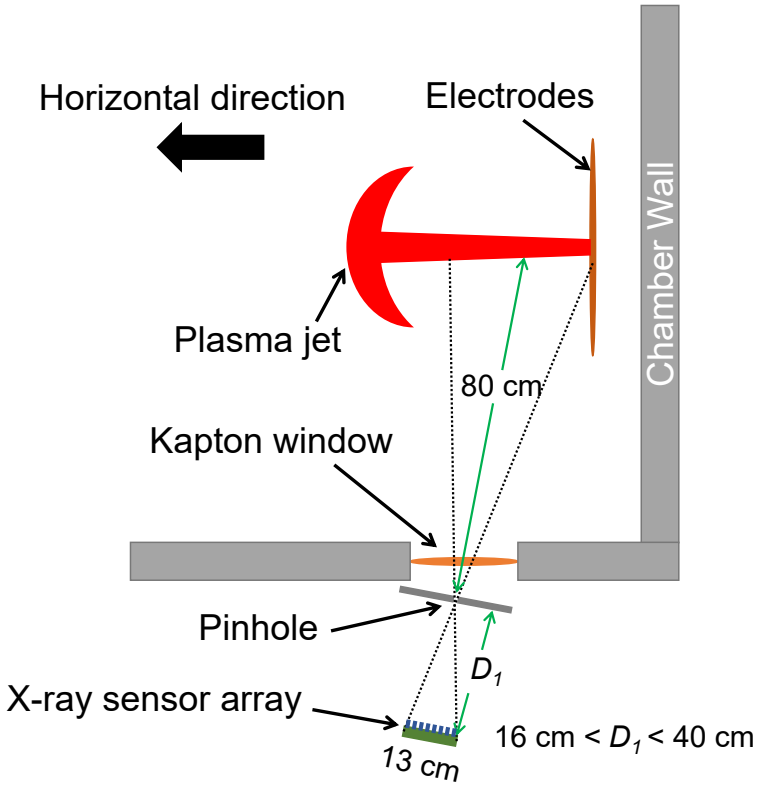

Figure 4.4: Diagram illustrating the location of an X-ray sensor array oriented horizontally with respect to the plasma jet. This configuration resolves the horizontal position of the X-ray source. The vertical position of the X-ray source can be resolved if the X-ray sensor array is rotated 90 degrees. D_1 denotes the pinhole-to-array distance. Varying D_1 adjusts the horizontal field of view. A smaller D_1 allows the X-ray camera to image X-rays that are farther away from the electrodes.

configuration but not with the location of the Rayleigh-Taylor instability in the HF configuration.

Besides X-ray sources near the inner electrode, X-ray sources around 30 to 40 cm away from the electrode were also identified via imaging. These X-rays were only observed in the HF configuration but not in the LF configuration. In order to capture these farther X-rays, the pinhole-to-array distance was reduced to 16 cm to enlarge the horizontal FOV. Figure 4.7 (a) and (b) show two such horizontal pinhole X-ray images taken with the PIN-diode-based camera. The bright spots near the tails of the two arrows in Figure 4.7 correspond to the X-ray sources that are 30–40 cm away from the electrode. The location of these X-ray sources coincides with the position of a spatially translatable metal frame [33] shown in Figure 4.8. The periodic, bright stripes in these images are due to unwanted electromagnetic interference. The metal

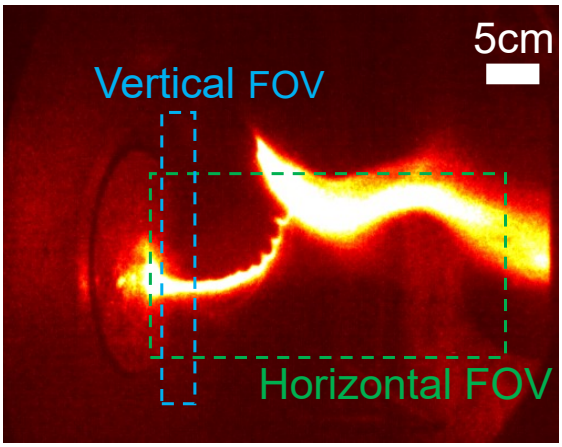

Figure 4.5: False color image of a plasma jet taken by the fast framing camera with dashed boxes indicating horizontal and vertical fields of view of the 1D X-ray camera. By combining X-rays seen in these two fields of view, we can locate the source of X-rays in two dimensions. The horizontal field of view (FOV) has a large vertical dimension because a long and narrow pinhole was used. However, the 1D camera can only resolve X-rays along the horizontal direction in the horizontal FOV.

frame was moved toward the electrode by approximately 6 cm in the interval between the times when Figure 4.7(a) and (b) were taken. Correspondingly, the image of the X-ray source also shifted by approximately the same distance. This shift can be seen obviously in the time-integrated (100 ns integration time) intensities shown in Figure 4.7(c). The measurement of X-rays both near the electrode and near the metal frame suggests that the energetic particles travel both toward and away from the electrode when X-rays are produced in the HF configuration.

Vertical X-ray Images

Figure 4.9 shows pinhole and coded aperture X-ray images taken with X-ray sensor array oriented vertically and pointed at the surface of the inner electrode. The decoded images in Figure 4.9(b) are produced from the raw coded aperture image in Figure 4.9(a). All 3 images are for plasma jets in the LF configuration. The vertical axis is now the space axis, and the horizontal axis is the time axis. These images show a localized X-ray source in the center of the FOV around 5 μs after plasma breakdown, but some unwanted artifacts occur on the decoded image in Figure 4.9(b). These unwanted artifacts can be better seen in a time-integrated image (100 ns integration time) shown in Figure 4.10(a). In comparison, the pinhole image in Figure 4.9(c) or the time-integrated version of the image in Figure 4.10(b) is artifact-free and clearly shows a localized X-ray source in the center. As expected, the maximum

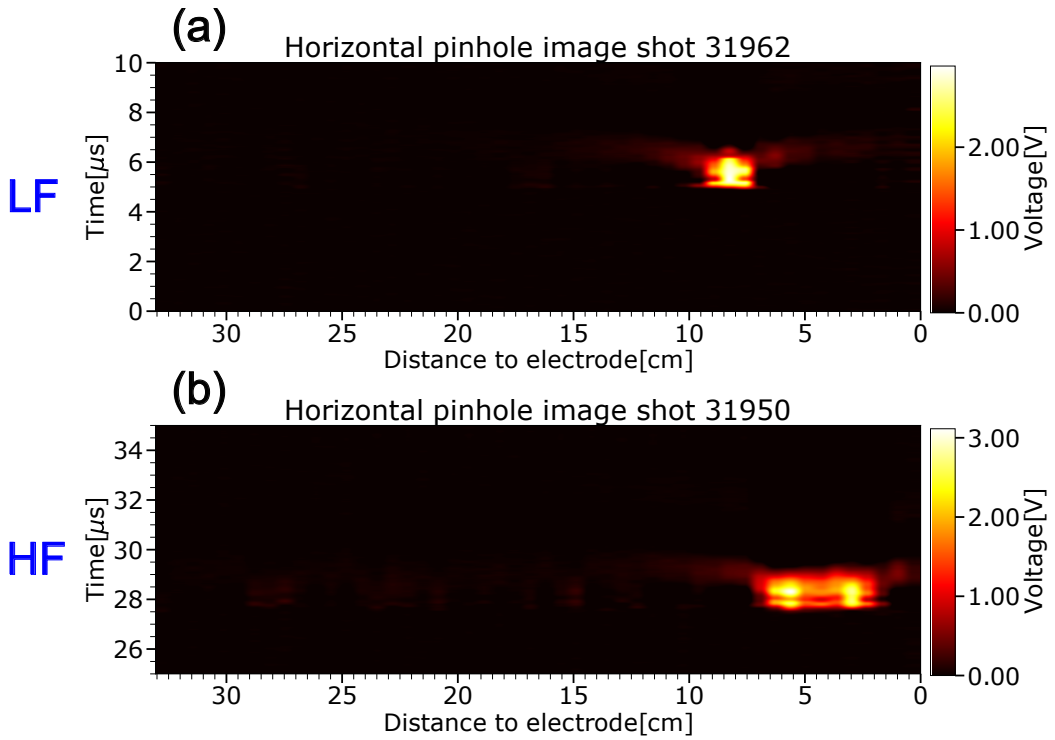

Figure 4.6: (a)–(b) Horizontal X-ray pinhole images taken with the PIN-diode-based camera in the low-flux (LF) configuration and the high-flux (HF) configuration. The right ends of the images roughly correspond to the location of the inner electrode. The bright regions on the 2 images represent X-ray sources a few centimeters away from the inner electrode.

voltage in the decoded image is higher than that in the pinhole image, so the coded aperture indeed collected more X-rays. However, this improvement in X-ray collection efficiency is not significant enough to overcome the harm of unwanted artifacts because the effective signal-to-noise ratio (SNR) of Figure 4.10(a) is not better than the SNR of Figure 4.10(b).

Vertical X-ray images from the HF configuration was significantly more difficult to capture. Figure 4.11 shows some of the X-ray images with a reasonable quality but a very low reproducibility. The X-ray sources in these images are also located in the center of the FOV, but they are more extended than the X-ray sources in the LF configuration.

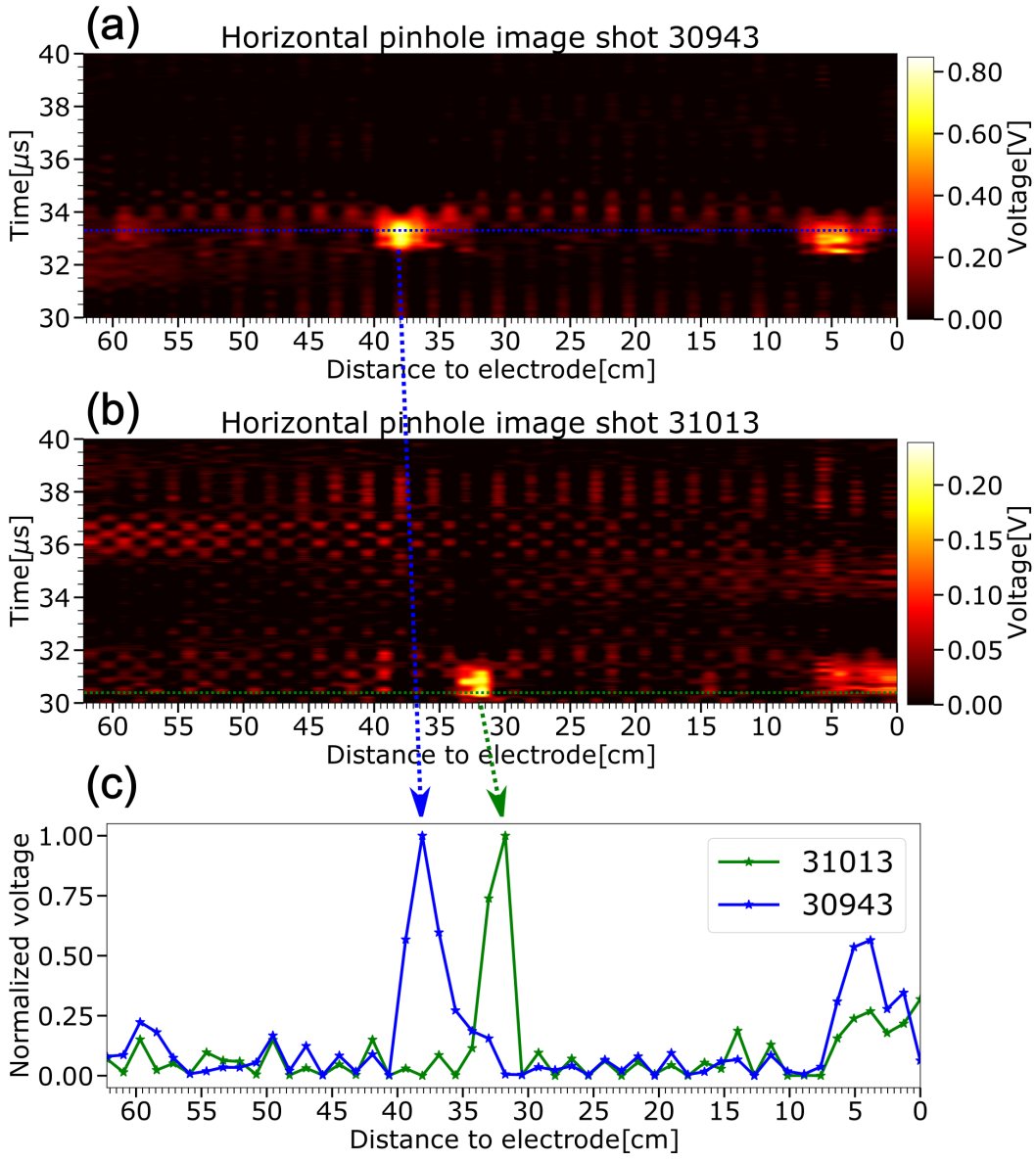

Figure 4.7: (a) and (b) are horizontal X-ray pinhole images taken with the PIN-diode-based camera in the high-flux configuration. The bright spots near the tails of the two arrows correspond to the X-ray sources that are 30–40 cm away from the electrode. The location of these X-ray sources coincides with the position of a spatially translatable metal frame. (c) shows the time-integrated (100 ns integration time) intensities of (a) and (b). The shift between the two peaks in (c) is due to the movement of the metal frame in the interval between the times when (a) and (b) were taken.

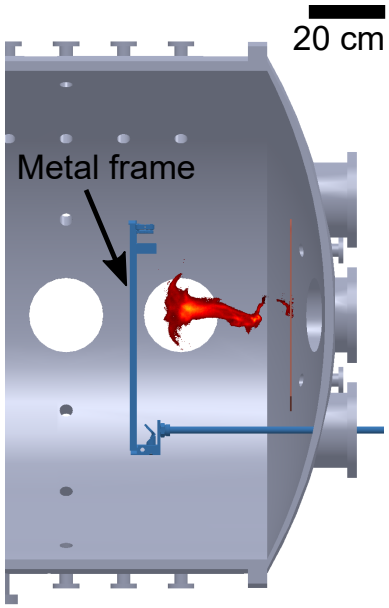

Figure 4.8: Side view of the plasma jet experiment showing the location of a spatially translatable metal frame responsible for X-rays that are 30–40 cm away from the electrode.

X-ray Images Taken by the SPARTA Camera

X-rays from the plasma jet experiment were imaged by a commercial high-speed X-ray camera called SPARTA in August 2022. SPARTA is a 2D camera that has 128 x 512 pixels. The size of each pixel is 200 µm × 200 µm. Each pixel is sensitive to single photons in the 3–15 keV range. The maximum frame rate of the camera is 6 MHz (~160 ns inter-frame time), and the camera can take up to 352 frames per shot. Operation of this camera requires a chiller to avoid overheating.

Figure 4.12 illustrates how the camera was positioned relative to the plasma jet: the camera was oriented horizontally and placed 7 cm from a circular pinhole with a 5 mm diameter. The distance between the pinhole and the plasma jet was around 80 cm.

Figure 4.13 shows some X-ray images from shot 32504. The green dots in these images represent pixels with counts above the maximum background count. The count of a pixel is set to either 1 or 0. The images are displayed in this manner to help us see weak X-ray signals, but the intensity information is lost. These images agree with the PIN diode X-ray images shown in Figure 4.7 reasonably well and show X-ray sources that are near the electrode and near the metal frame. Even though the distance between the SPARTA camera and the plasma experiment was closer

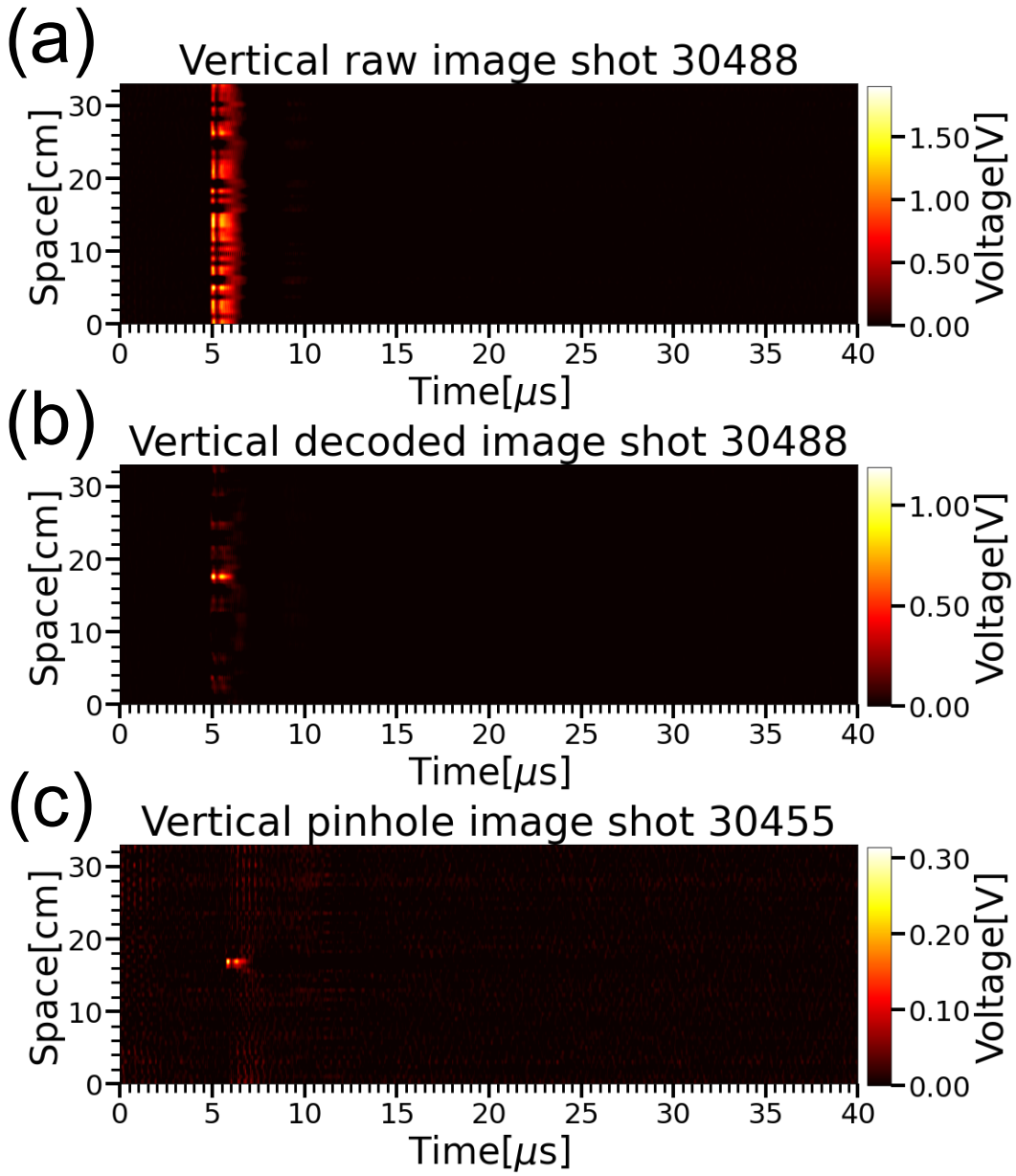

Figure 4.9: Vertical X-ray images taken with the PIN-diode-based X-ray camera in the low-flux configuration. (a) is the raw image projected by a coded aperture. (b) is the corresponding decoded image generated using the decoding algorithm. (c) is an image formed by a pinhole equivalent to an individual element of the coded aperture. Both the decoded image and the pinhole image show a localized X-ray source in the center of the field of view around 5 µs, but some unwanted artifacts in (b) make the central X-ray source seem more extended.

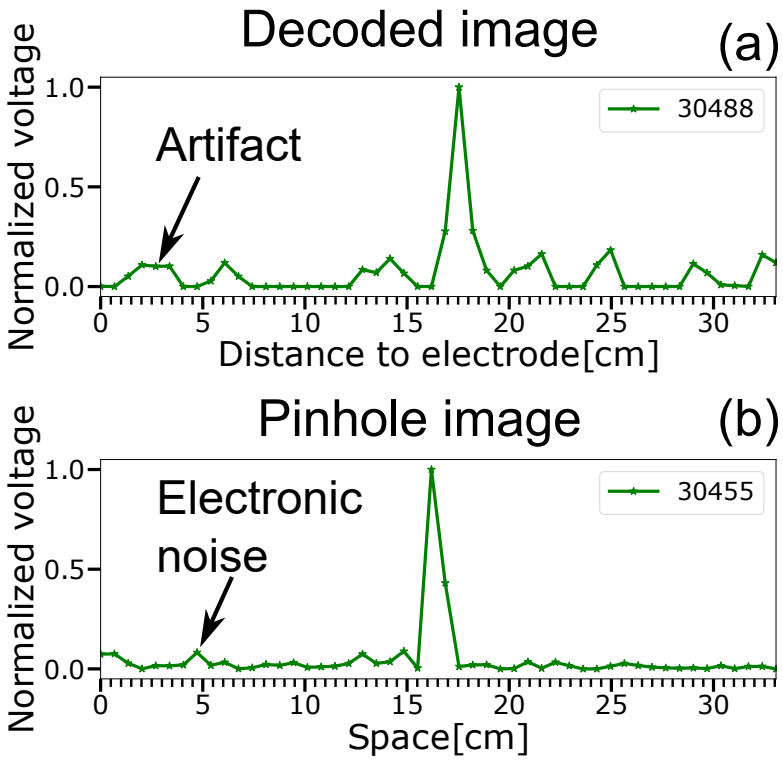

Figure 4.10: (a) is the time-integrated (100 ns integration time) intensity of the image shown in Figure 4.9(b). This image has some unwanted artifacts whose amplitudes are roughly one tenth of the the amplitude of the central peak. Electronic noise is not visible in this image. (b) is the time-integrated (100 ns integration time) intensity of the image shown in Figure 4.9(c). This image is artifact free, but a small amount of electronic noise is visble.

than the distance between the PIN-diode-based X-ray camera and the experiment, the images taken by the SPARTA camera were not affected by the noisy plasma experiment. Comparing Figure 4.13(a) to Figure 4.13(c), we see that the X-rays near the electrode occurr slightly earlier than the X-rays that are emitted from the metal frame.

4.3 A Possible Explanation for the Artifacts

Even though the decoded image in Figure 4.9(b) resembles its equivalent pinhole image in Figure 4.9(c), the unwanted artifacts in the decoded image make the localized X-ray source look more extended. According to a review on coded aperture imaging by Cannon and Fenimore [58], these artifacts are typical for almost all coded aperture cameras in practice because of imperfection in the decoding algorithm. In the Caltech experiment, one likely cause of imperfection is the low number of X-ray

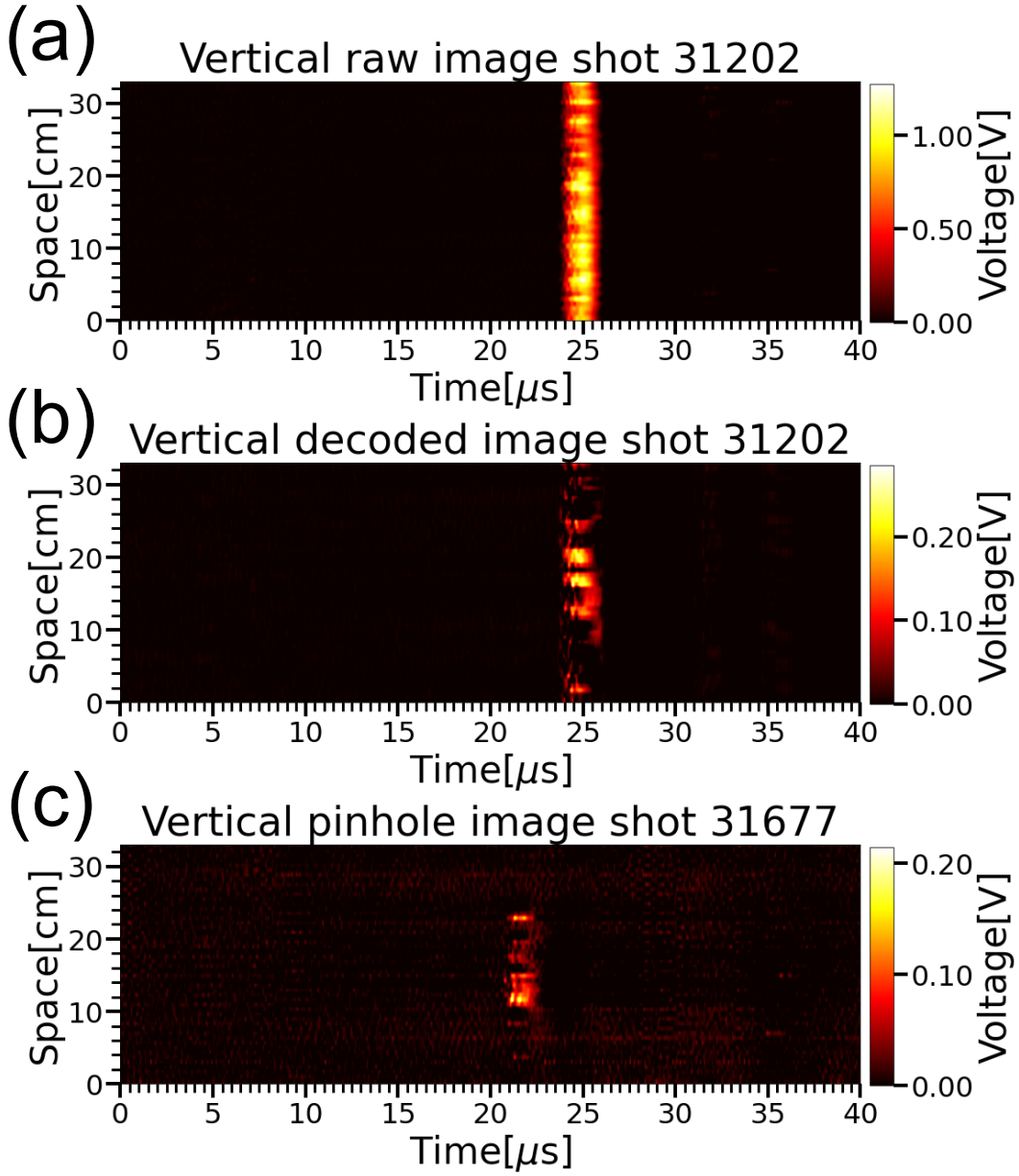

Figure 4.11: Vertical X-ray images taken with the PIN-diode-based X-ray camera in the high-flux (HF) configuration. (a) is the raw image projected by a coded aperture. (b) is the corresponding decoded image generated using the decoding algorithm. (c) is an image formed by a pinhole equivalent to an individual element of the coded aperture. These images show that the X-ray source from the HF configuration is more extended than the X-ray source from the low-flux configuration. However, these images are not highly reproducible (the reproducibility is roughly one in every thirty shots). The coded aperture used for these images was 5.6 cm wide instead of 1 cm wide, so more incident X-rays could be collected.

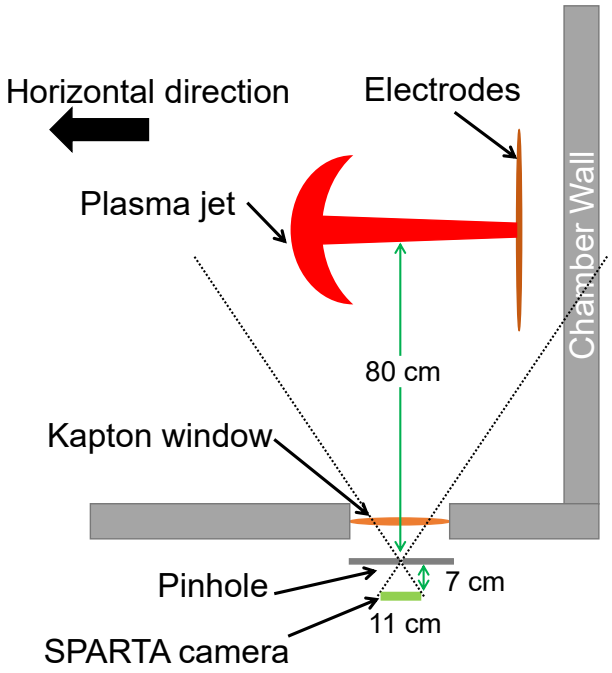

Figure 4.12: This diagram shows how the SPARTA camera is positioned relative to the plasma jet. The SPARTA camera is a 2D camera so it can resolve X-rays along the horizontal and vertical directions.

photons. This is intuitive because the decoding algorithm is based on the shadow cast by a coded aperture mask. If the number of incident X-ray photons is low, an imperfect shadow will be cast.

We illustrate that a low X-ray photon number can cause artifacts in decoded images with a 2D ray-tracing simulation shown in Figure 4.14. Figure 4.14(a) shows the geometry of the ray-tracing simulation with spacing similar to the actual experiment. An X-ray point source at (0,0) emits a variable number of X-ray photons toward a 1D X-ray sensor array (represented as a black vertical line) 1300 mm away, and the photons that survive through a coded aperture mask 900 mm away from the source are shown as blue lines. The direction of each photon is sampled from a uniform probability distribution. We measure the number of photons using the photon counts per pixel when the mask is absent because this quantity is independent of the mask pattern and can be measured experimentally. Figure 4.14(b) shows a recorded image and the corresponding decoded image from a simulation with 0.7 photon counts per pixel. Because each pixel in the recorded image is only hit by a couple of photons, the recorded image is far from being ideal. As a result, the decoded image contains artifacts that are comparable to the central peak (the actual signal) around pixel 64.

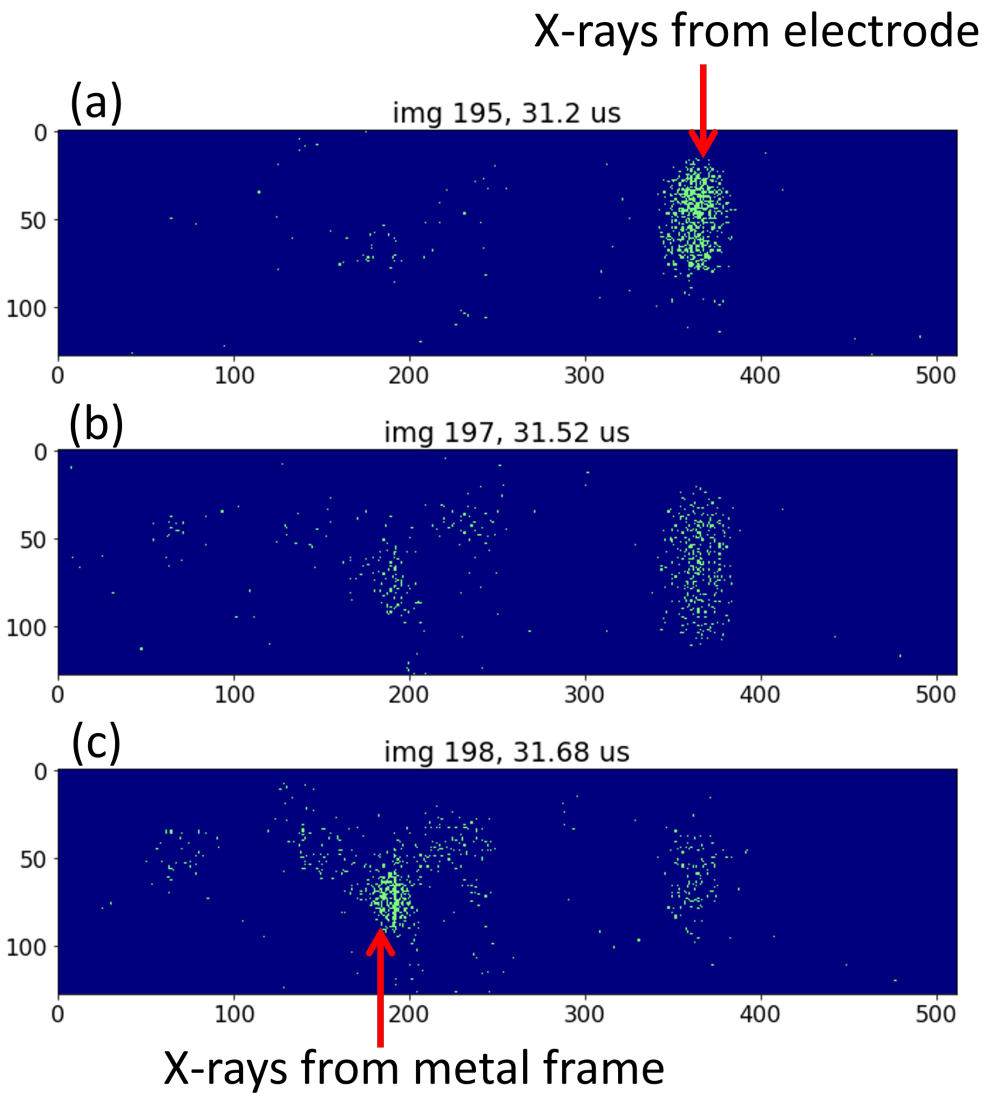

Figure 4.13: (a)–(c) show X-ray images taken by the SPARTA camera in the high-flux configuration. These images are displayed in a way such that the count of a pixel is either 1 or 0. The green dots are bright pixels with counts that are above the background count. (a) shows that a strong X-ray source first occurs near the electrode. (c) shows that, around 480 ns later, another strong X-ray source near the metal frame that is far from the electrode occurs. These images agree reasonably well with the X-ray images taken by the PIN-diode-based X-ray camera (see Figure 4.7).

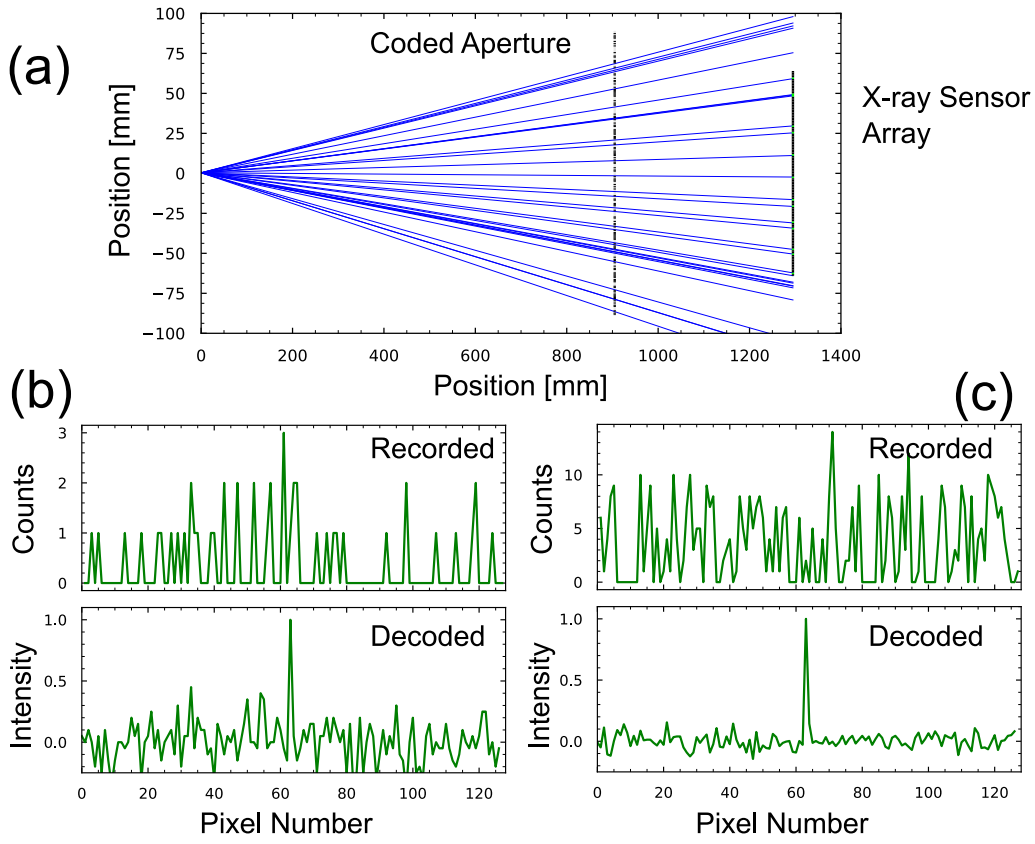

Figure 4.14: (a) shows the geometry of a ray-tracing simulation with a coded aperture mask located 900 mm away from the point source at (0,0). The black line at x = 1300 mm represents a 1D X-ray sensor array. The spacing in this simulation is similar to the actual experiment. The point source at (0,0) emits a variable number of photons toward the X-ray sensor array, and the photons that survive through the coded aperture mask are shown as blue lines. (b) shows the image recorded by the X-ray sensor array and the corresponding decoded image from a simulation with 0.7 photon counts per pixel if the mask were absent. The recorded and decoded images from a similar simulation with seven photon counts per pixel if the mask were absent are shown in (c). The larger photon number suppresses the artifacts in the decoded image in (c). The results in (b) are closer to the actual experiment.

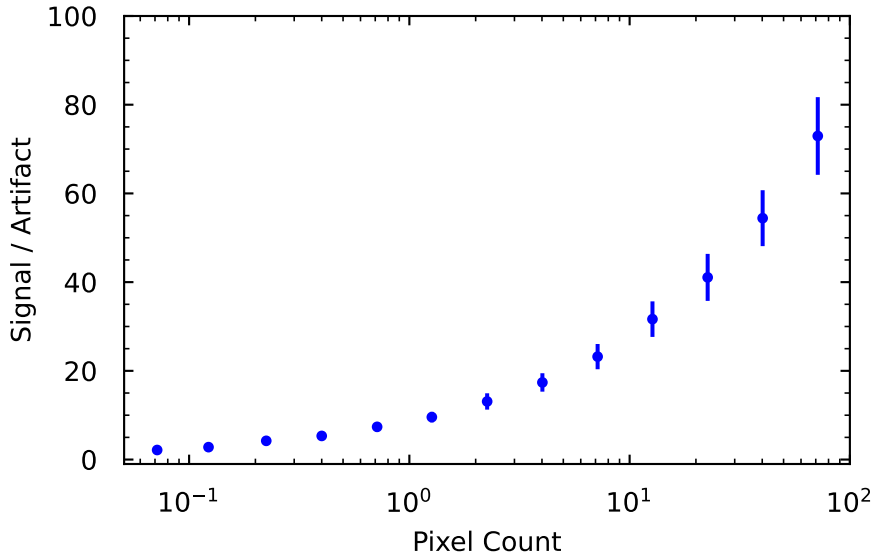

Figure 4.15: The ratio of the amplitude of the decoded signal to the root mean square of the artifacts is plotted against the number of photon counts per pixel if the mask were absent. Each data point represents a mean from 100 simulations, and the error bar on each data point represents a standard deviation from the same 100 simulations. The signal-to-artifact ratio increases as the photon counts per pixel increases. Around 10 counts per pixel are required to form an image with $>$ 20 signal-to-artifact ratio.

In comparison, Figure 4.14(c) shows the results of a simulation with seven photon counts per pixel. The artifacts in the decoded image are significantly suppressed because the recorded image approaches the ideal recorded image formed by an infinite number of photons. The results in Figure 4.14(b) are closer to the actual experiment because a bright pixel in the experiment was typically hit by only a few X-ray photons.

To better quantify the effect of photon number on artifacts, we plot the signal-to-artifact ratio, which is defined as the ratio of the amplitude of the central peak to the root mean square of the artifacts, as a function of photon counts per pixel in Figure 4.15. Each data point in Figure 4.15 is obtained by calculating the mean from 100 simulations with the same number of photon counts per pixel. The error bar associated with each data point represents the standard deviation from the same 100 simulations. As expected, the signal-to-artifact ratio improves as the photon number increases to form a better recorded image. Around 10 counts per pixel are required to achieve a $>$ 20 signal-to-artifact ratio.

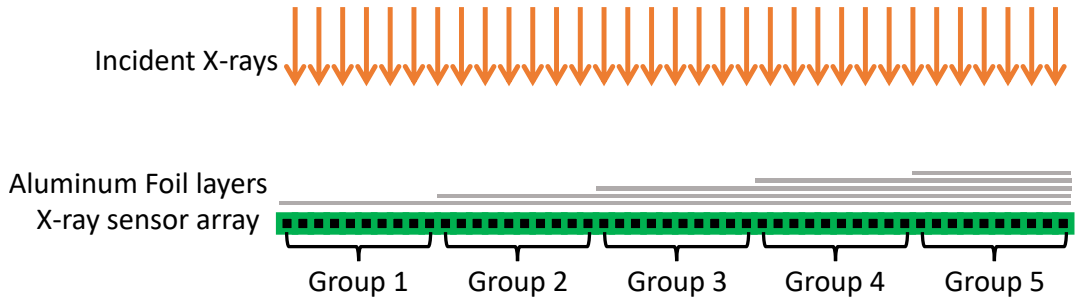

Figure 4.16: Aluminum foil arrangement for measuring X-ray energy. 50 pixels of the PIN-diode-based X-ray sensor array are divided into five groups with 10 pixels in each group. Pixels in group 1 (pixel 1–10) are covered with one layer of aluminum foil (18 μm thickness), group 2 (pixel 11–20) with two layers of foil, all the way up to group 5 (pixel 41–50) with five layers of foil. This arrangement allows us to measure X-ray attenuation as a function of foil layers.

4.4 Measure X-ray Energy

Foil Arrangement

The PIN-diode-based X-ray camera can also be configured to measure X-ray energy. In the energy measurement configuration, the 50 pixels of the PIN-diode-based X-ray sensor array are divided into five groups with 10 pixels in each group. These five groups are covered by an increasing number of aluminum foil layers. Specifically, pixels in group 1 (pixel 1–10) are covered with one layer of aluminum foil (18 μm thickness), group 2 (pixel 11–20) with two layers of foil, all the way up to group 5 (pixel 41–50) with five layers of foil. The foil arrangement described above is depicted in Figure 4.16. Pinhole/coded aperture masks are removed to allow incident X-rays to reach all pixels.

Even though the X-rays from the plasma jet experiment are not strictly mono-energetic, a simple exponential decay model was used to estimate the mean energy of X-rays. The intensity of mono-energetic X-rays decreases exponentially as the X-rays pass through a metal foil with thickness x. Since the output pulse amplitude V of a pixel of the X-ray sensor array is proportional to the intensity of incident X-rays, V should satisfy

$$\frac{V}{V_0} = e^{-\mu x} \quad \text{or} \quad \ln V = -\mu x + \ln V_0, \tag{4.1}$$

where μ is a linear attenuation coefficient that depends on the X-ray energy and the material of the foil. Figure 4.17 shows the energy dependence of μ for aluminum.

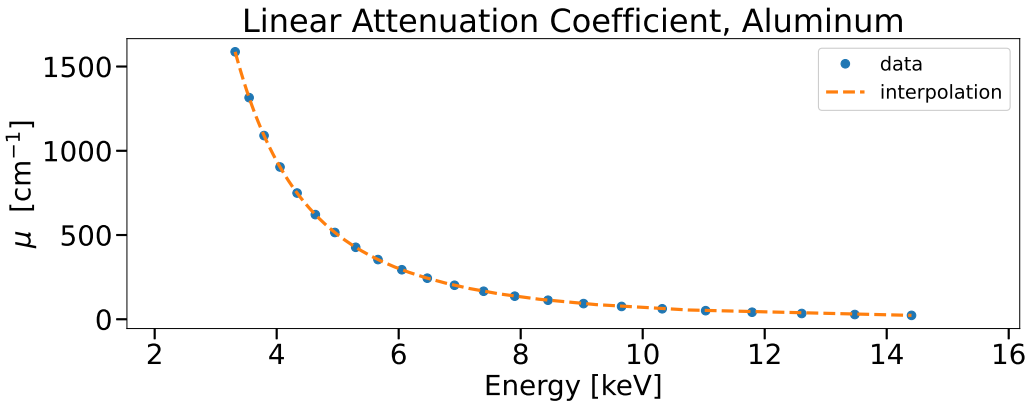

Figure 4.17: Interpolation showing linear attenuation coefficient μ of aluminum at different X-ray energies. An aluminum foil with a thickness equal to the inverse of the attenuation coefficient attenuates X-ray intensity by a factor of $e \approx 2.7$. Data is taken from the "X-Ray Form Factor, Attenuation, and Scattering Tables" database maintained by National Institute of Standards and Technology.

Energy Measurement

An energy measurement for X-rays from the plasma jet experiment is shown in Figure 4.18. In Figure 4.18(a), voltage amplitudes from pixels covered by different numbers of foil layers are plotted. Voltages from pixels near the group boundaries, such as pixel 10 and 20, are omitted to avoid confusion about the number of foil layers covering these pixels. As the the pixel number increases along the horizontal axis, the pixels are covered by more foil layers, so their voltage amplitudes decrease correspondingly.

The voltage amplitudes in Figure 4.18(a) are grouped up according to foil layers. The standard deviation and the mean of each group are calculated. These means and standard deviations are used for a weighted least squares fit shown in Figure 4.18(b). The slope of the linear fit corresponds to a linear attenuation coefficient of 167 ± 29 cm^{-1}, and the X-ray energy associated with this coefficient is 7.4 ± 0.4 keV according to Figure 4.17. This result is reasonable considering the X-ray attenuating materials between the plasma jet and the X-ray sensor array, namely the Kapton sheet, the air between the Kapton window and the x-ray sensor array, and the aluminum foil covering the X-ray sensor array. Figure 4.19 shows the relevant transmission curves of Kapton, air, and aluminum[75]. The red solid line on the bottom of the plot represents the product of the three transmission curves above, and this solid line essentially determines that only $>$ 6 keV X-rays from the plasma jet experiment could reach the X-ray sensor array with a high transmission. This measurement

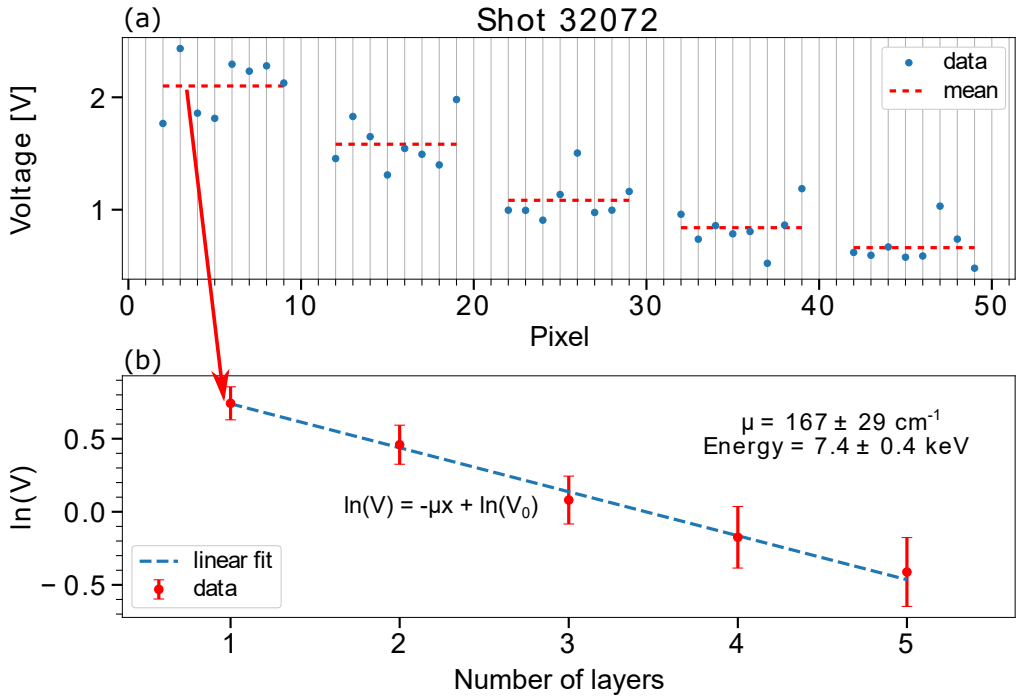

Figure 4.18: (a) shows voltage amplitudes from different pixels of the PIN-diode-based X-ray sensor array. Pixels near the group boundaries, such as pixels 10 and 20, are neglected because the number of foil layers covering these pixels is ambiguous. Red dashed lines represent mean voltages of different groups of pixels. The mean voltages and the standard deviations of five groups are used for a weighted least squares fit shown in (b). The slope of the fit corresponds to a specific linear attenuation coefficient μ, and the value of μ can be translated to a mean X-ray energy using the data from Figure 4.17.

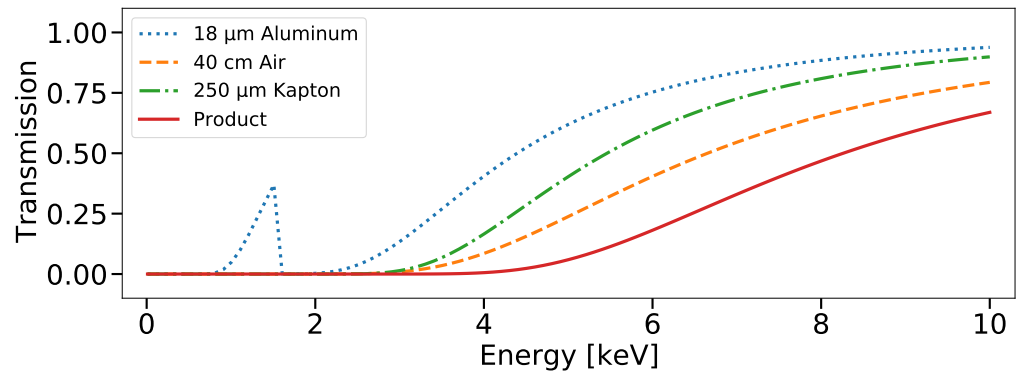

Figure 4.19: X-ray transmission curves of Kapton, air, and aluminum. The red curve is the product of all three curves above it. According to the red solid line, only X-rays with energy that is greater than 6 keV can reach the PIN diode X-ray detector with a > 0.2 transmission. The data in this plot is obtained from a study by Henke, Gullikson, and Davis [75].

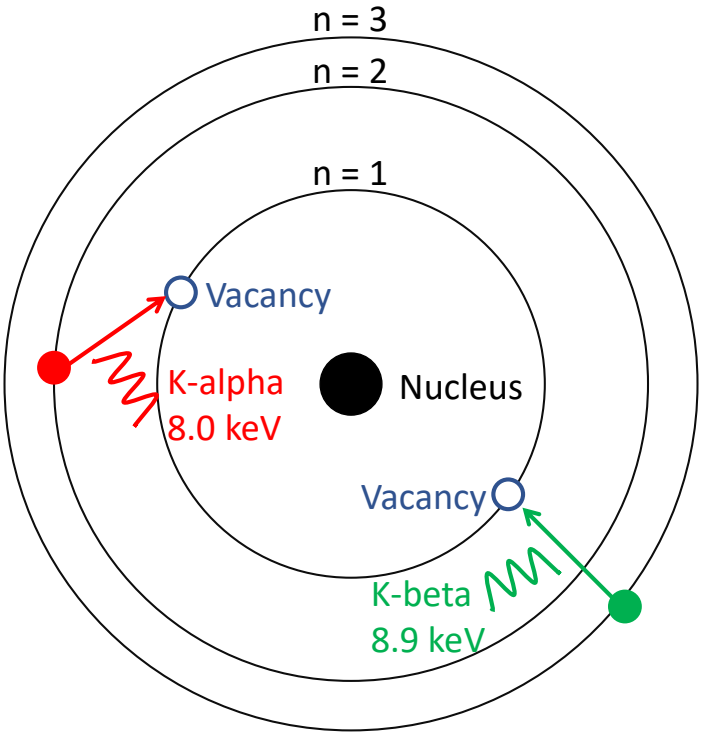

Figure 4.20: The atomic energy diagram of a copper atom. The K-alpha X-ray is emitted when an electron transitions from the $n = 2$ level to the $n = 1$ level to fill a vacancy in the $n = 1$ level. The K-beta X-ray is emitted when an electron transitions from the $n = 3$ level to the $n = 1$ level.

does not preclude the possibility that the plasma jet experiment could generate < 6 keV X-rays, but these low energy X-rays would not survive to reach the X-ray sensor array outside the vacuum chamber.

Filtering X-rays with Nickel and Copper

When an energetic particle hits a copper atom, an electron in the innermost shell (K shell, principal quantum number $n = 1$) can be knocked out by the energetic particle, and a vacancy is left behind. When this vacancy is filled by an outer electron, 8.0 keV (K-alpha) or 8.9 keV (K-beta) characteristic X-rays are emitted depending on the initial energy level of the outer electron [76], as illustrated in the atomic energy diagram in Figure 4.20. These copper characteristic X-rays could be an explanation for the X-rays emitted near the copper electrode. In order to investigate these characteristic X-rays, we can use K-edges, which are sudden decreases in the transmission curves. These K-edges can be easily seen in the copper and nickel transmission curves shown in Figure 4.21.

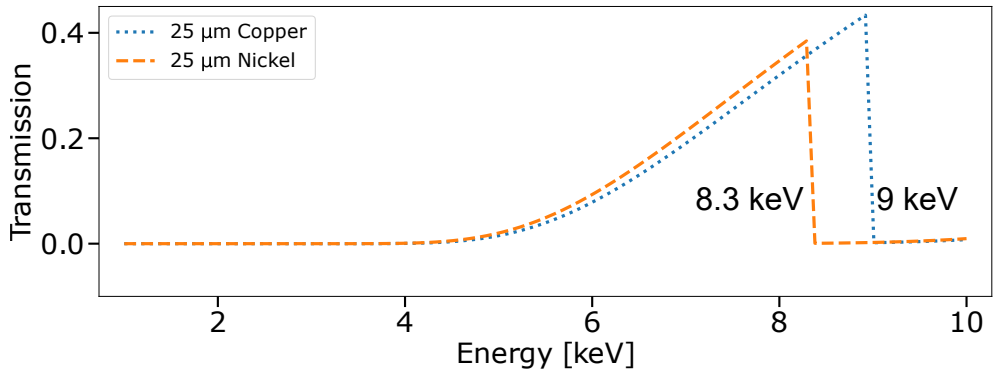

Figure 4.21: The transmission curves of 25 μm thick copper and nickel obtained from the study by Henke, Gullikson, and Davis [75]. The nickel transmission curve has a K-edge near 8.3 keV, and the copper transmission curve has a K-edge near 9 keV [77]. If the energy of an X-ray photon is between 8.3 and 9 keV, then the photon can transmit through copper but not nickel.

These K-edges form because an atom can efficiently absorb an X-ray photon with an energy that is just above the binding energy of an electron in the K shell of that atom. Because the K-edge of nickel is at 8.3 keV and the K-edge of copper is at 9 keV [77] (the K-edge energy must be greater than the energy of characteristic X-rays), an X-ray photon with an energy that is between 8.3 keV and 9 keV can effectively transmit through copper but not nickel. Therefore, if the X-rays emitted near the copper electrode of the jet experiment happened to be the K-beta X-rays (8.9 keV) of copper, then we could in principle identify these X-rays with copper and nickel filters.

Figure 4.22 shows that about half of the pixels on the X-ray sensor array are covered by one layer of 25 μm thick nickel foil and the other half of the pixels are covered by one layer of 25 μm thick copper foil. A piece of thick aluminum metal is placed in the middle to block a few pixels from the incident X-rays. These pixels act as a clear boundary between the nickel foil region and the copper foil region. The X-ray sensor array with this foil arrangement was oriented horizontally and exposed to the X-rays from the LF configuration. The voltage amplitudes of all 50 pixels are represented by blue stars in Figure 4.23. The blue solid lines connecting the blue stars are visual aids that do not have any physical meaning. The black dashed lines represent the mean amplitudes in the nickel and copper regions. Since there is not a big difference between the two mean amplitudes, the X-rays from the LF configuration must have passed through two metal foils with a similar transmission. Thus, we can safely conclude that the X-rays emitted near the copper electrode must

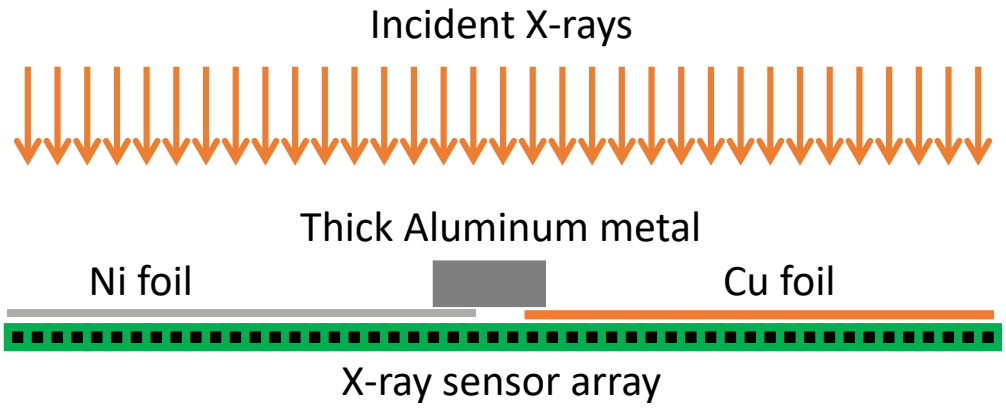

Figure 4.22: The first half of the X-ray sensor array is covered by one layer of 25 μm thick nickel foil, and the second half of the array is covered by one layer of 25 μm thick copper foil. The thick aluminum metal in the middle of the array blocks all incident X-rays and creates a clear boundary between the pixels covered by nickel foil and the pixels covered by copper foil.

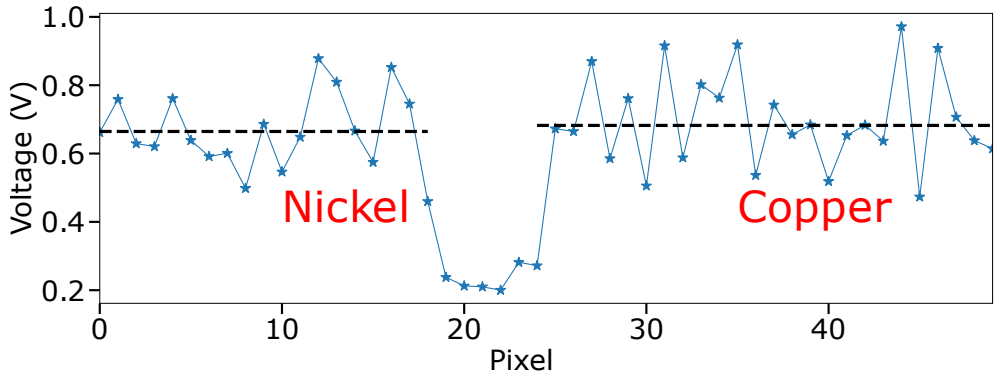

Figure 4.23: This plot shows the voltage amplitudes of all 50 pixels of the X-ray sensor array after the pixels have been exposed to X-rays from the low-flux configuration. The blue stars are the actual data points, and the blue lines connecting the stars do not have any physical meaning. The two black dashed lines represent the mean voltages of the pixels in the nickel region and the copper region. Because these two mean voltages are similar, the nickel foil and the copper foil must have transmitted the X-rays equally.

have spectral components outside the 8.3–9 keV range.

The nickel-copper measurement that has been studied so far does not preclude the possibility that the X-rays emitted near the copper electrode are primarily the 8 keV K-alpha copper X-ray. In fact, measurements on copper emission spectra have shown that the intensity of the K-alpha copper X-ray is about 7 times stronger than that of the K-beta copper X-ray [76]. If one is interested in identifying whether X-rays are mainly the K-alpha copper X-ray, then the nickel filter needs to be replaced by a cobalt filter which has a K-edge energy of 7.7 keV [77].

Chapter 5

TWO-STREAM INSTABILITY IN THE CALTECH PLASMA JET EXPERIMENT

[1] Y. Zhou and P. M. Bellan. "Two-stream instability with a growth rate insensitive to collisions in a dissipative plasma jet". In: *Physics of Plasmas* 30 (2023), p. 052101. DOI: 10.1063/5.0146806.

5.1 Introduction

The two-stream instability, also known as the Buneman instability, is a fundamental plasma behavior that can lead to rapid, unstable growth of small perturbations, resulting in effective dissipation of currents in plasmas [24]. This instability is typically triggered when the electron drift velocity relative to ions is faster than the electron thermal velocity [3]. The two-stream instability is believed to be related to the formation of a double layer (DL) [78, 79, 80, 81, 82, 83, 84] which is a large, localized electric field parallel to the current flow or magnetic field inside a plasma. This localized electric field is called a double layer because the associated charge density given by Poisson's equation consists of two spatially-separated and oppositely-charged layers of particles [79]. Studying the two-stream instability and double layers is of value in understanding particle energization in astrophysical plasmas [85], nuclear fusion [21], plasmas for space propulsion [86], and laboratory plasma discharges [87, 88].

Traditionally, the two-stream instability is derived from two-fluid equations or Vlasov equations by neglecting collision terms [3, 24, 25], and it is commonly presumed that the inclusion of collision terms damps the instability. The Vlasov equations and the two-fluid equations are listed in Appendix A for reference. In fact, many analytical and numerical studies [26, 27, 28, 29, 30, 31] have argued that collisions suppress the instability. However, these studies typically do not account for the momentum change of ions as a result of collisions, resulting in violation of momentum conservation. In this chapter, we present a collisional two-fluid model which conserves total momentum. The momentum conservation enables this two-fluid model to describe a very low-frequency two-stream instability which, contrary to conventional presumptions, maintains its characteristic behavior even if the plasma is extremely collisional. This low-frequency two-stream instability will

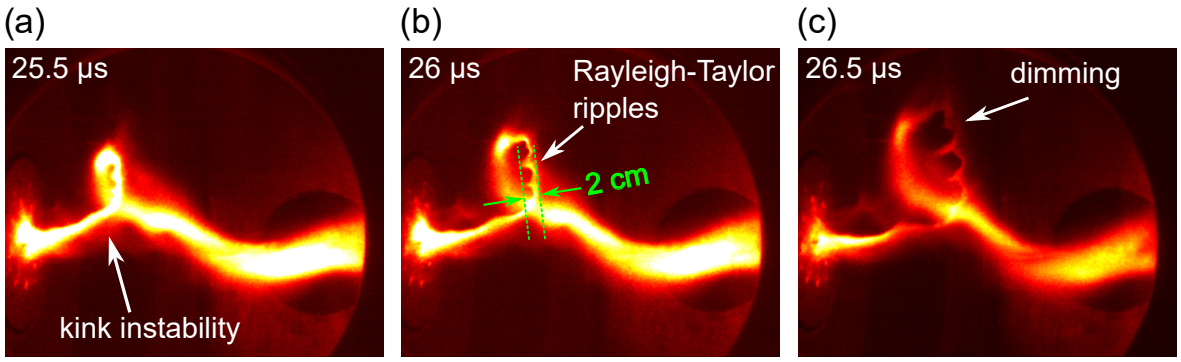

Figure 5.1: A sequence of false color images of the plasma jet in the Caltech experiment. (a) The plasma jet becomes helical due to the Kruskal-Shafranov kink instability. (b)–(c) The current channel cross section becomes constricted at the location of the Rayleigh-Taylor ripples and then dims.

be referred to as an evacuation instability because it has similarities to an evacuation mechanism proposed long ago by Alfvén and Carlqvist [89, 90] and then elaborated by Carlqvist [90] in the context of density depletion and double layer formation with the important exceptions that here (i) collisionality is taken into account and (ii) the driver of the evacuation instability is a naturally occurring periodic constriction of the plasma cross section.

5.2 Observations in the Caltech Plasma Jet Experiment

The motivation of this study is to explain previous extreme ultraviolet (EUV) and visible light observations made in the Caltech plasma jet experiment [19]. The experiment setup is described in detail in Chapter 2. Figure 5.1 shows a typical sequence of transient events that occur after the jet has lengthened from several centimeters to tens of centimeters in the high-flux configuration. At approximately 20 μs the jet develops a helical instability (kink), and Figure 5.1(a) shows this kink after it has grown in about 5 μs to a finite size; the kink identification and its onset being consistent with Kruskal-Shafranov theory was presented previously [14]. Since the kinking is a rapid exponential growth of a corkscrew shape, kinking produces a strong lateral acceleration of each segment of the plasma jet away from the initial axis of the jet. This lateral acceleration provides a large effective gravity (10^{10} – 10^{11} m/s^2) that causes a secondary instability called the Rayleigh-Taylor (RT) instability; this rapid acceleration and the resulting RT instability ripples were reported previously [15]. Figure 5.1(a) and (c) show that in 1 μs these ripples significantly constrict the cross section of the plasma jet. Chai, Zhai, and Bellan [19]

observed that the region constricted by the RT ripples became bright in EUV radiation (20–60 eV, see Figure 3 of Chai, Zhai and Bellan [19]) but, as can be seen in Figure 3 of Chai, Zhai, and Bellan and in Figure 5.1(c) here, the constricted region also became dim in visible light. The visible light dimming suggests a reduction of the plasma density n has occurred since visible light emission is proportional to n^2, the EUV brightening suggests electrons are heated to a higher energy to excite or further ionize ions to emit EUV radiation. It has been unclear why the dimming in visible light and the brightening in EUV should occur simultaneously.

5.3 Model Description

Overview of the Model

We present here a collisional two-fluid model consistent with the observed behavior; this model describes an evacuation instability that has a rapid growth rate γ despite $\gamma \ll \nu_{ei}$, where ν_{ei} is the electron-ion collision frequency. The model critically depends on the plasma jet having a large electric current flowing along the jet axis (z direction). Since magnetic forces are perpendicular to currents, there are no magnetic forces in the z direction, so a 1D electrostatic model describes the dynamics along the z direction. The jet current I is constant because the power supply driving the jet operates in a constant current mode. This means that the current density $J = I/A$ must increase when the RT ripples constrict the jet cross-sectional area A. MHD instabilities such as the kink and RT are incompressible [91] and so imply the density n is constant when the plasma jet is perturbed by the kink and RT instabilities. Because $J = nq_e u_e$, where q_e is the electron charge and $u_e < 0$ is the electron drift velocity relative to ions, u_e should become more negative when J increases. Hence, the absolute value $|u_e|$ will peak at the constricted location, as shown in Figure 5.2 (a) and (b). Figure 5.1(a) and (c) show that the radius of the plasma jet current channel is reduced from initially greater than 1 cm to eventually less than 0.3 cm. As a result, $A = \pi r^2$ is constricted approximately by a factor of 10 to 20 (from > 3 cm^2 to < 0.2 cm^2). With $I = 70$ kA and $n = 10^{22}$ m^{-3}, $|u_e| = I/Anq_e$ can increase from below 1×10^5 m/s to above 2×10^6 m/s. The electron thermal velocity of the 2 eV plasma jet is approximately $v_{Te} = \sqrt{\kappa T_e/m_e} \approx 6 \times 10^5$ m/s. Therefore, the initially slower electron drift velocity will greatly exceed v_{Te} due to the constriction of A. It will be shown that this suprathermal electron drift velocity triggers the evacuation instability that can create a density cavity at the constricted location, as shown in Figure 5.2(c). This density cavity would then cause the dimming of visible light.

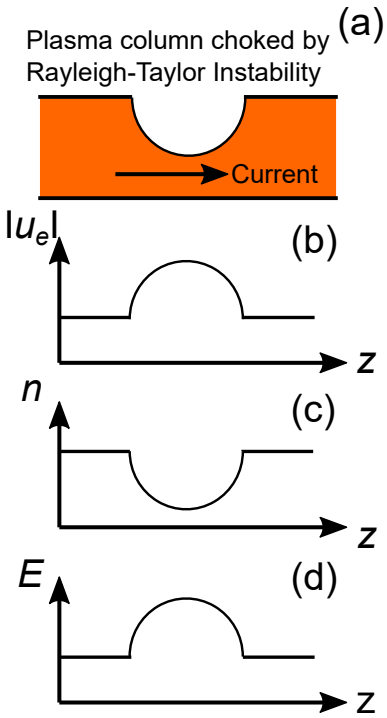

Figure 5.2: The cartoon in (a) illustrates the choking of the plasma jet current channel cross section A by RT ripples as shown in Figure 5.1(b). Plots (b)–(d) illustrate the electron drift velocity $|u_e|$, density n, and electric field E at the constricted location respectively.

Due to the combination of low temperature ($T_e \approx T_i \approx 2$ eV) and high density ($n_e \approx n_i \approx 10^{22}$ m^{-3}), the characteristic electron-ion collision frequency for the plasma jet is

$$\nu_{ei} = \frac{e^{5/2}}{2 \times 3^{3/2} \pi \varepsilon_0^2 m_e^{1/2}} \frac{n_i \ln \Lambda}{T_e^{3/2}} \approx 10^{11} \text{ s}^{-1}, \tag{5.1}$$

where $\ln \Lambda$ is the Coulomb logarithm whose value is assumed to be around 10, and T_e is in units of electron volts. This fast collision frequency corresponds to a 10^{-10}–10^{-11} s characteristic collision time scale. Since this collision time is five to six orders of magnitude smaller than the 10^{-6}–10^{-5} s jet dynamic time scale, the jet dynamics is highly collisional. Thus, a model explaining how the RT ripples lead to simultaneous visible light dimming (density evacuation) and EUV brightening must take into account that there are 10^5 – 10^6 electron-ion collisions in the 1 μs observed time scale of the visible light dimming and EUV brightening. Clearly whatever is happening cannot be described by a collisionless instability. One may argue that the subset of suprathermal electrons at the constricted region could be collisionless because the electron-ion collision frequency for these fast electrons

should be significantly smaller [92]. A quick estimate of this smaller collision frequency shows that this argument is not correct: we can roughly estimate the collision frequency by replacing the T_e in Equation (5.1) with the kinetic energy of electrons traveling at $u_e \approx 2 \times 10^6$ m/s, i.e., $m_e u_e^2/2 \approx 11$ eV. This kinetic energy reduces the collision frequency to be around 8×10^9 s^{-1}, which corresponds to a 1×10^{-10} s characteristic collision time.

Because the plasma jet is extremely collisional, we can consider the plasma jet as a resistor whose resistance is inversely proportional to A. When A is constricted by RT ripples, the resistance at the constricted location should increase. As the current carried by the plasma jet flows through this location with larger resistance, a DL, as shown in Figure 5.2(d), would develop to heat the plasma locally. This heating can potentially explain the observed EUV radiation. A collisional two-fluid model that contains the presumptions discussed above will be derived in the next section.

Derivation of the Collisional Two-Fluid Model

We can derive our collisional two-fluid model by neglecting various small terms from the familiar 1-dimensional, unmagnetized, two-fluid equations for a fully ionized, collisional plasma, namely

$$\frac{\partial n_e}{\partial t} + \frac{\partial}{\partial z}(n_e u_e) = 0, \tag{5.2}$$

$$\frac{\partial n_i}{\partial t} + \frac{\partial}{\partial z}(n_i u_i) = 0, \tag{5.3}$$

$$m_e \left(\frac{\partial u_e}{\partial t} + u_e \frac{\partial u_e}{\partial z} \right) = q_e E - \frac{1}{n_e} \frac{\partial P_e}{\partial z} - \frac{R_{ei}}{n_e}, \tag{5.4}$$

$$m_i \left(\frac{\partial u_i}{\partial t} + u_i \frac{\partial u_i}{\partial z} \right) = q_i E - \frac{1}{n_i} \frac{\partial P_i}{\partial z} - \frac{R_{ie}}{n_i}, \tag{5.5}$$

$$\varepsilon_0 \frac{\partial E}{\partial z} = n_i q_i + n_e q_e. \tag{5.6}$$

Variables in the above equations are defined in the usual way. The electron energy equation is assumed to be the isothermal equation of state, i.e., $P_e = n_e \kappa T_e$ with T_e being a constant, and the ion energy equation is assumed to be the adiabatic equation of state $P_i \propto n_i^\Gamma$ where Γ is an adiabatic constant of order unity. Justification of these energy equations can be found below. The collision terms satisfy $R_{ei} + R_{ie} = 0$ because the collisions between electrons and ions must conserve the overall momentum. The derivation of Equations (5.2–5.6) can be found in several plasma physics textbooks [93, 94, 95].

For simplicity, we consider the two-fluid equations in a reference frame that moves with the plasma jet center of mass velocity. In this frame, ions are nearly stationary because the mean ion velocity approximately equals the plasma jet center of mass velocity, i.e.,

$$u_i \approx \frac{m_e n_e u_e + m_i n_i u_i}{m_e n_e + m_i n_i}. \tag{5.7}$$

As a result, u_e in this reference frame not only describes the mean electron drift velocity but also the electron drift velocity relative to ions. This use of u_e is consistent with the definition of u_e in Section 5.3.

We will analyze equations near an unstable equilibrium with an initial density n_0 and an initial suprathermal drift velocity u_{e0} that satisfies $1 \ll u_{e0}/v_{Te} \ll \sqrt{m_i/m_e}$. This fast u_{e0} is achieved when the plasma jet cross section is significantly constricted. This equilibrium is perturbed by an evacuation instability that has a space-time dependence proportional to $\exp(ik_z z + \gamma t)$, where the wavenumber $k_z = 2\pi/\lambda$ is defined by the wavelength λ of the RT ripples ($\sim$ 1 cm) and the growth rate γ is assumed to be faster than that of the RT instability (γ_{RT} is experimentally measured to be on the order of 1×10^6 s^{-1}) but slower than $k_z v_{Te}$.

Figure 5.3 shows the assumed γ is either much smaller or much bigger than several characteristic frequencies relevant to the Caltech plasma jet experiment. After an expression for γ is derived, it can be directly verified that γ indeed falls in the range indicated by this plot, i.e.,

$$\gamma_a \ll k_z v_{Ti} \ll \gamma_{RT} \ll \gamma \ll k_z v_{Te} \ll k_z u_{e0} \ll \omega_{pi} \ll \nu_{ei}, \tag{5.8}$$

where γ_a is the growth rate of the ion-acoustic instability (see Section 5.5), and ω_{pi} is the ion-plasma frequency. The physically relevant inequality (5.8) establishes that a number of terms in Equations (5.2)–(5.6) are extremely small and so may be neglected; the detailed arguments for dropping these terms are as follows:

1. The plasma is quasi-neutral, so $n_e = n_i = n$ when ions are singly charged. From now on, n will be used to denote either the electron or ion density. This simplification is equivalent to assuming the left-hand side (LHS) of Equation (5.6) is negligible compared to either one of the two terms on the right-hand side (RHS), i.e.,

$$\left| \varepsilon_0 \frac{\partial E}{\partial z} \right| \ll |n_i q_i| \, , |n_e q_i| \, , \tag{5.9}$$

   so the two terms on the RHS approximately balance each other.

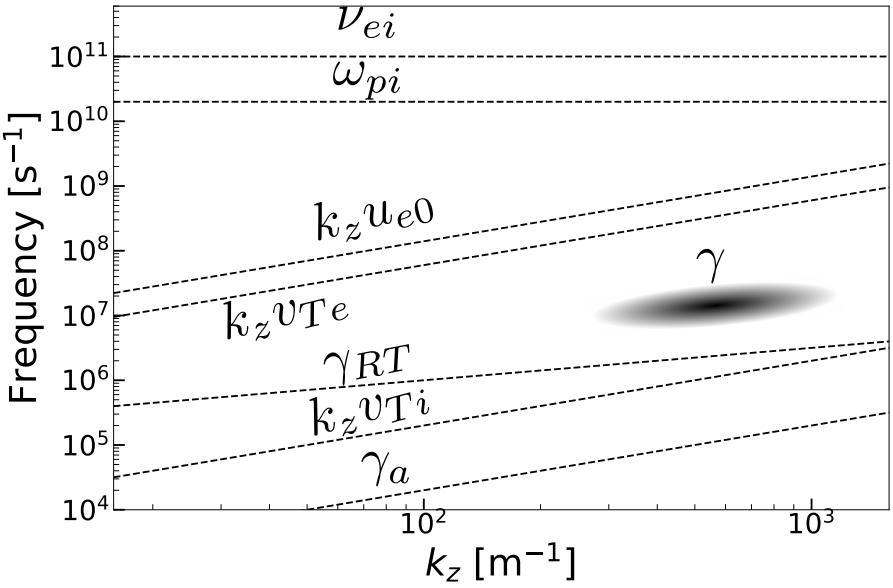

Figure 5.3: A plot of various characteristic frequencies in the Caltech plasma jet as a function of k_z. The dashed lines represent characteristic frequencies estimated with experimental measurements. The growth rate γ_{RT} of the RT instability is approximated by the formula $\gamma_{RT} \approx \sqrt{g_{\text{eff}} k_z}$, where the effective gravity g_{eff} is estimated from image data to be $\sim 10^{10}$ m/s^2. The ion acoustic instability growth rate γ_a is approximated to be an order of magnitude smaller than $k_z c_s$ where c_s is the ion acoustic velocity $\sqrt{\kappa T_e/m_i}$ (see Section 5.5). The growth rate γ of the evacuation instability, indicated by the shaded ellipse, is assumed to be at an intermediate location that is either much bigger or smaller than a characteristic frequency. This separation in frequencies enables several simplifications of the original two-fluid equations.

Justifying this quasi-neutral simplification requires the wavelength of the perturbation to be much longer than the electron Debye length $\lambda_{De} = \sqrt{\varepsilon \kappa T_e/nq_e^2}$. This requirement can be written as

$$k_z^2 \lambda_{De}^2 \ll 1, \tag{5.10}$$

which is satisfied when $k_z v_{Ti} \ll \gamma \ll \omega_{pi}$ because

$$k_z^2 \lambda_{De}^2 = \frac{k_z^2 v_{Te}^2}{\omega_{pe}^2} = \frac{k_z^2 v_{Ti}^2}{\omega_{pi}^2} \ll \frac{\gamma^2}{\omega_{pi}^2} \ll 1. \tag{5.11}$$

2. The partial time derivative in Equation (5.2) is negligible compared to the spatial derivative of n, i.e.,

$$\left|\frac{\partial n}{\partial t}\right| \ll \left|u_e \frac{\partial n}{\partial z}\right|. \tag{5.12}$$

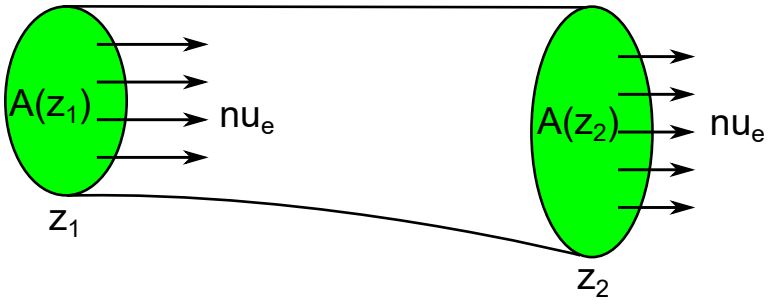

Figure 5.4: A current channel with varying cross-sectional area extending from z_1 to z_2. The product nu_eA is independent of z.

Ignoring the time derivative simplifies Equation (5.2) to be $\nabla \cdot (nu_e\hat{z}) = 0$ which when integrated over the volume of a current channel extending from z_1 to z_2, as shown in Figure 5.4, gives $n(z_2)u_e(z_2)A(z_2) - n(z_1)u_e(z_1)A(z_1) = 0$. Since z_1 and z_2 are arbitrary, the equation above is equivalent to $n(z)u_e(z)A(z) =$ constant for any z (specifically, nu_eA is constant at the constriction location). This corresponds to stating that the electric current flowing along the channel is independent of z.

This simplification is justified when γ is small compared to $k_z u_{e0}$. This is because the linearized form of inequality (5.12) can be reduced to $\gamma \ll k_z u_{e0}$ due to the $\exp(ik_z z + \gamma t)$ dependence of perturbations.

3. Similar to simplification 2, the partial time derivative in Equation (5.4) can be ignored compared to the convective term, i.e.,

$$\left|\frac{\partial u_e}{\partial t}\right| \ll \left|u_e \frac{\partial u_e}{\partial z}\right|. \tag{5.13}$$

4. Electrons are isothermal, so the electron pressure is $P_e = n\kappa T_e$ where T_e is a constant.

   The validity of this assumption relies on γ being much smaller than $k_z v_{Te}$. This is because electrons can be considered as isothermal for a perturbation with a characteristic velocity γ/k_z that is slow compared to the electron thermal velocity v_{Te}.

5. The ion pressure term can be ignored compared to the partial time derivative in Equation (5.5), i.e.,

$$\left|\frac{1}{n}\frac{\partial P_i}{\partial z}\right| \ll \left|m_i \frac{\partial u_i}{\partial t}\right|. \tag{5.14}$$

This simplification is equivalent to assuming $k_z v_{Ti} \ll \gamma$ because the the linearized form of inequality (5.14) can be rewritten as $\Gamma k_z^2 v_{Ti}^2 \ll \gamma^2$ and the adiabatic constant Γ is of order unity. To see how this can be done, we first multiply both sides of inequality (5.14) by n_0/m_i and express P_{i1} in terms of n_1 using the linearized adiabatic equation of state $P_{i1} = \Gamma \kappa T_i n_1$:

$$\left| \Gamma v_{Ti} \frac{\partial n_1}{\partial z} \right| \ll \left| n_0 \frac{\partial u_{i1}}{\partial t} \right|. \tag{5.15}$$

We can then differentiate both sides with respect to z and eliminate u_{i1} using the linearized form of Equation (5.3) (see Equation [5.26]) to get

$$\left| \Gamma v_{Ti} \frac{\partial^2 n_1}{\partial z^2} \right| \ll \left| \frac{\partial^2 n_1}{\partial t^2} \right|. \tag{5.16}$$

Assuming n_1 is proportional to $\exp(ik_z z + \gamma t)$ gives us desired inequality $\Gamma k_z^2 v_{Ti}^2 \ll \gamma^2$.

The 5 simplifications listed above reduce the original system of two-fluid equations to be

$$n q_e u_e A = I = \text{constant}, \tag{5.17}$$

$$\frac{\partial n}{\partial t} + \frac{\partial}{\partial z}(n u_i) = 0, \tag{5.18}$$

$$m_e u_e \frac{\partial u_e}{\partial z} = q_e E - \frac{\kappa T_e}{n} \frac{\partial n}{\partial z} - \frac{R_{ei}}{n}, \tag{5.19}$$

$$m_i \left(\frac{\partial u_i}{\partial t} + u_i \frac{\partial u_i}{\partial z} \right) = q_i E - \frac{R_{ie}}{n}. \tag{5.20}$$

Adding Equations (5.19) and (5.20) gives

$$m_e u_e \frac{\partial u_e}{\partial z} + m_i \left(\frac{\partial u_i}{\partial t} + u_i \frac{\partial u_i}{\partial z} \right) + \frac{\kappa T_e}{n} \frac{\partial n}{\partial z} = 0, \tag{5.21}$$

which has the interesting feature of being a two-fluid equation that, while taking collisions into account, does not explicitly depend on collisions. By two-fluid, it is meant that the equation is beyond the scope of MHD as there is an explicit dependence on electron mass. The collision terms in Equations (5.19) and (5.20) can be arbitrarily large without affecting Equation (5.21).

If the collision effects are neglected and the cross-sectional area A is assumed to be uniform, the system of Equations (5.17)–(5.21) reduces to Carlqvist's collisionless evacuation mechanism [90] and to the collisionless equations studied by Galeev et

al. [96] and by Bulanov and Sarosov [97]. Because collision effects and a constricted A are not considered in References [90, 96, 97], these studies failed to describe the unidirectional DL electric field shown in Figure 5.2(d) (note that the electric field in Figure 2d of Carlqvist [90] is bidirectional). It will be shown in Section 5.3 that collision effects and a constricted A are critical for producing the unidirectonal DL electric field.

Growth Rate of the Evacuation Instability

We now consider the cross section A to vary on the time scale of the RT instability which is assumed to be much slower than the evacuation instability being derived. Thus, A is a slowly varying parameter from the point of view of the evacuation instability, and a decrease of A with a consequent increase of u_e is effectively the "knob" that triggers the fast evacuation instability. Because the decrease of A is caused by the RT instability, the evacuation instability can be considered as a tertiary instability triggered by the secondary RT instability.

The growth rate γ of the evacuation instability can be calculated in the jet frame (ion velocity is nearly zero in this frame) by first linearizing Equations (5.17), (5.18), and (5.21) about an initial equilibrium with a uniform density n_0 and an electron drift velocity u_{e0} to obtain

$$n_0 u_{e1} + n_1 u_{e0} = 0, \tag{5.22}$$

$$\frac{\partial n_1}{\partial t} + n_0 \frac{\partial u_{i1}}{\partial z} = 0, \tag{5.23}$$

$$m_e u_{e0} \frac{\partial u_{e1}}{\partial z} + m_i \frac{\partial u_{i1}}{\partial t} + \frac{\kappa T_e}{n_0} \frac{\partial n_1}{\partial z} = 0, \tag{5.24}$$

where the subscript 1 denotes a small perturbation to the initial equilibrium. The cross-sectional area A is treated as a constant when linearizing Equation (5.17). We can express u_{e1} and u_{i1} in terms of n_1 using Equations (5.22) and (5.23):

$$u_{e1} = -\frac{n_1 u_{e0}}{n_0}, \tag{5.25}$$

$$\frac{\partial u_{i1}}{\partial z} = -\frac{1}{n_0} \frac{\partial n_1}{\partial t}. \tag{5.26}$$

Multiplying Equation (5.24) by $-n_0$ and differentiating the resulting equation with respect to z give

$$-n_0 m_e u_{e0} \frac{\partial^2 u_{e1}}{\partial z^2} - n_0 m_i \frac{\partial^2 u_{i1}}{\partial t \partial z} - \kappa T_e \frac{\partial^2 n_1}{\partial z^2} = 0. \tag{5.27}$$

We can get an equation that only involves n_1 by eliminating u_{i1} and u_{e1} using Equations (5.25) and (5.26):

$$m_e u_{e0}^2 \frac{\partial^2 n_1}{\partial z^2} + m_i \frac{\partial^2 n_1}{\partial t^2} - \kappa T_e \frac{\partial^2 n_1}{\partial z^2} = 0. \tag{5.28}$$

We can then derive a dispersion relation by assuming the density perturbation n_1 has an $\exp(ik_z z + \gamma t)$ dependence:

$$-k_z^2 m_e u_{e0}^2 + \gamma^2 m_i + k_z^2 \kappa T_e = 0, \tag{5.29}$$

which can be solved for γ to obtain

$$\gamma = k_z \sqrt{\frac{m_e}{m_i}(u_{e0}^2 - v_{Te}^2)}. \tag{5.30}$$

Equation (5.30) shows γ is real and positive when u_{e0} is greater than v_{Te}, so this instability is triggered when reduction of A causes the electron drift velocity to exceed the electron thermal velocity. It is important to note that, while collisions have been taken into account, this instability does not depend on whether or not the plasma is collisional. Thus, the instability should occur in a highly collisional plasma such as the Caltech plasma jet. Using $k_z = 700$ m^{-1}, $m_e = 9.1 \times 10^{-31}$ kg, $m_i = 6.7 \times 10^{-26}$ kg, $u_{e0} = 2 \times 10^6$ m/s, and $v_{Te} = 6 \times 10^5$ m/s, we can estimate the instability growth rate γ for the Caltech argon plasma jet to be $\gamma \approx 5 \times 10^6$ s^{-1}, which is indeed consistent with Figure 5.3.

Electric Field

The electric field in the plasma jet can be found from Equation (5.4):

$$E = \frac{m_e}{q_e}\left(\frac{\partial u_e}{\partial t} + u_e \frac{\partial u_e}{\partial z}\right) + \frac{1}{n q_e}\frac{\partial P_e}{\partial z} + \frac{R_{ei}}{n q_e}. \tag{5.31}$$

As discussed in Section 5.3 and shown in Figure 5.3, the electron-ion collision frequency ν_{ei} is much larger than any other characteristics frequencies, such as $k_z u_{e0}$ and $k_z v_{Te}$. The collisional term $R_{ei}/n q_e$ is proportional to ν_{ei}:

$$\frac{R_{ei}}{n q_e} = \frac{\nu_{ei} m_e (u_e - u_i)}{q_e} \approx \frac{\nu_{ei} m_e u_e}{q_e}. \tag{5.32}$$

Thus, we can assume the collision term in Equation (5.31) is the dominant term that balances the electric field, i.e.,

$$E \approx \frac{\nu_{ei} m_e u_e}{q_e}. \tag{5.33}$$

This electric field is in fact a DL that is inversely proportional to the cross-sectional area A. Before the plasma jet is constricted significantly, the electron drift velocity is slower than the electron thermal velocity v_{Te}. To first order, we can assume ν_{ei} is initially proportional to $nT_e^{-3/2} \ln\Lambda$. Since T_e is a constant for isothermal electrons and $\ln\Lambda$ does not vary much, ν_{ei} is approximately proportional to n. Thus, the electric field in Equation (5.33) is approximately proportional to the electron flux nu_e, which is inversely proportional to the cross-sectional area A because $nu_e = I/q_e A$. Therefore, this electric field is enhanced at the region constricted by RT ripples and appears as a DL as shown in Figure 5.2(d).

The combination of this DL and high collisionality of the plasma jet can possibly cause Ohmic heating which can potentially explain the 20–60 eV EUV radiation observed in the plasma jet experiment. Because the Caltech plasma jet is highly collisional, this DL electric field can be quite large. For example, this DL can be as large as $\sim 6 \times 10^4$ V/m, when the relative drift velocity is $u_e \approx 1 \times 10^5$ m/s and the electron-ion collision frequency is $\nu_{ei} \approx 1 \times 10^{11}$ s^{-1}. A complication associated with Ohmic heating is if the local electron temperature is increased to become sufficiently large, then the condition $u_e \gg v_{Te}$ would cease and the evacuation instability would be quenched; consideration of this higher order issue will be left for future consideration and so will not be addressed here.

The $1/A$ dependence derived above depends on ν_{ei} being proportional to $nT_e^{-3/2} \ln\Lambda$. However, assuming ν_{ei} is proportional to $nT_e^{-3/2} \ln\Lambda$ is not valid when the electron drift velocity becomes significantly faster than the electron thermal velocity [92]. As a result, the DL due to collisions will probably not scale as $1/A$ when the plasma jet is constricted significantly. In fact, the strength of the DL may decrease because the collisionality of suprathermal electrons decreases as the relative drift velocity increases [92]. When the strength of DL has decreased to a point that it no longer dominates the RHS of Equation (5.31), we can retain an extra term from Equation (5.31):

$$E = \frac{R_{ei}}{nq_e} - \frac{m_e}{2|q_e|}\frac{\partial u_e^2}{\partial z}. \tag{5.34}$$

The newly included term on the RHS of Equation (5.34) is the leading order correction because the linearized form of this term is proportional to $k_z u_{e0}$, which is smaller than ν_{ei} but larger than other relevant characteristic frequencies according to Figure 5.3.

The new correction term is proportional to the partial z derivative of u_e^2. Across

the constricted region, the velocity profile in Figure 5.2(b) has a maximum, so the partial z derivative of u_e^2 will be positive on the LHS of the maximum and negative on the RHS of the maximum. Because the constant in front of the partial z derivative is negative, the second term should point away from constricted region. Since u_e can grow exponentially once the evacuation instability is triggered, this initially insignificant bidirectional electric field will also grow exponentially and possibly become stronger than the unidirectional DL eventually. Unlike a unidirectional DL, this bidirectional electric field cannot accelerate the bulk of the streaming electrons since the associated electric potential does not have a net jump (the integral of the bidirectional electric field across the constricted region equals 0). However, a small fraction of electrons can possibly be accelerated by this bidirectional electric field in two opposite directions. These fast electrons could possibly explain why localized X-ray sources near the electrode and far from the electrode have been observed simultaneously in the Caltech plasma jet experiment (see Figure 4.7).

5.4 Numerical Solution

A numerical solution of the problem is now presented to demonstrate the evacuation instability when the cross-sectional area of Caltech's plasma jet is significantly constricted by the RT instability. The evacuation instability manifests itself as a fast growth of electron drift velocity and a rapid depletion of density in the numerical solution. This numerical solution replicates and extends the linear analysis.

Dimensionless Equations and Discretization

For the numerical treatment, we use Caltech-experiment-relevant reference quantities defined in Table 5.1 to normalize the equations of our collisional two-fluid model. For the reference quantities in Table 5.1, the reference length z_{ref}, density n_{ref}, and electric current I_{ref} are experiment-specific independent quantities that need to be prescribed. Other reference quantities can be derived from these three prescribed quantities, the elementary charge e, and the electron mass m_e. With these reference quantities, the dimensionless form of Equations (5.17), (5.18), and (5.21) are

$$\bar{n}\bar{u}_e\bar{A} = -\bar{I} = \text{constant}, \tag{5.35}$$

$$\frac{\partial \bar{n}}{\partial \bar{t}} + \frac{\partial}{\partial \bar{z}}(\bar{n}\bar{u}_i) = 0, \tag{5.36}$$

$$\frac{1}{2}\frac{\partial \bar{u}_e^2}{\partial \bar{z}} + \bar{m}_i\left(\frac{\partial \bar{u}_i}{\partial \bar{t}} + \frac{1}{2}\frac{\partial \bar{u}_i^2}{\partial \bar{z}}\right) + \bar{T}_e\frac{\partial}{\partial \bar{z}}\ln \bar{n} = 0, \tag{5.37}$$

Table 5.1: Definitions of reference quantities relevant to the Caltech plasma jet experiment.

Symbol	Reference quantity	Value
z_{ref}	length	1 cm
n_{ref}	density	10^{22} m^{-3}
I_{ref}	current	100 kA
q_{ref}	charge	$e = 1.6021 \times 10^{-19}$ C
m_{ref}	mass	$m_e = 9.1094{\times}10^{-31}$ kg
$A_{\text{ref}} = z_{\text{ref}}^2$	cross-sectional area	1 cm^2
$u_{\text{ref}} = I_{\text{ref}}/A_{\text{ref}} n_{\text{ref}} q_{\text{ref}}$	velocity	6.2×10^5 m/s
$t_{\text{ref}} = z_{\text{ref}}/u_{\text{ref}}$	time	16 ns
$T_{\text{ref}} = m_{\text{ref}} u_{\text{ref}}^2$	Temperature	2.2 eV

where the barred (dimensionless) variables are the original (dimensioned) variables divided by their associated reference quantities.

The 3 dimensionless equations above are discretized with the Forward Time Centered Space (FTCS) method. The spatial dimension $\bar{z}$ is discretized over the interval $[-\pi, \pi]$ with a mesh width of $h = \pi/128$. The dimensionless time $\bar{t}$ is discretized with a discrete time step of $k = 0.5h$. For any variable f defined on the $\bar{z} - \bar{t}$ space-time plane, f_j^m denotes the pointwise value $f(\bar{z}_j, \bar{t}_m)$. All quantities are assumed to be periodic so that $f(-\pi, \bar{t}_m) = f(\pi, \bar{t}_m)$. The discretized equations read

$$\bar{u}_{e,j}^m = \frac{-\bar{I}}{\bar{n}_j^m \bar{A}_j^m}, \tag{5.38}$$

$$\bar{n}_j^{m+1} = \bar{n}_j^m - \frac{k}{2h}\left(\bar{n}_{j+1}^m \bar{u}_{i,j+1}^m - \bar{n}_{j-1}^m \bar{u}_{i,j-1}^m\right), \tag{5.39}$$

$$\begin{aligned}\bar{u}_{i,j}^{m+1} =& \bar{u}_{i,j}^m - \frac{k}{2h\bar{m}_i}\left[\frac{\left(\bar{u}_{e,j+1}^m\right)^2 - \left(\bar{u}_{e,j-1}^m\right)^2}{2} + \bar{T}_e\left(\ln \bar{n}_{j+1}^m - \ln \bar{n}_{j-1}^m\right)\right] \\ & - \frac{k}{4h}\left[\left(\bar{u}_{i,j+1}^m\right)^2 - \left(\bar{u}_{i,j-1}^m\right)^2\right].\end{aligned} \tag{5.40}$$

Numerical Results

Given an area function $\bar{A}$ and parameters $\bar{I}$, $\bar{T}_e$, and $\bar{m}_i$, Equations (5.38)–(5.40) can be solved recursively for unknowns $\bar{u}_e$, $\bar{n}$, and $\bar{u}_i$ from an initial ion velocity $\bar{u}_i^0$ and an initial density $\bar{n}^0$. For the numerical solution to be presented in this section, we choose the area function to be $\bar{A} = \pi\left[1 - 15/16 e^{\bar{t}/1000}\text{sech}(2\pi\bar{z})\right]$, so that the cross-sectional area $\bar{A}$ at $\bar{z} = 0$ has been exponentially reduced by RT instability to $\pi/16$ at $\bar{t} = 0$. A plot of this area function at $\bar{t} = 0$ is shown in Figure 5.5. The

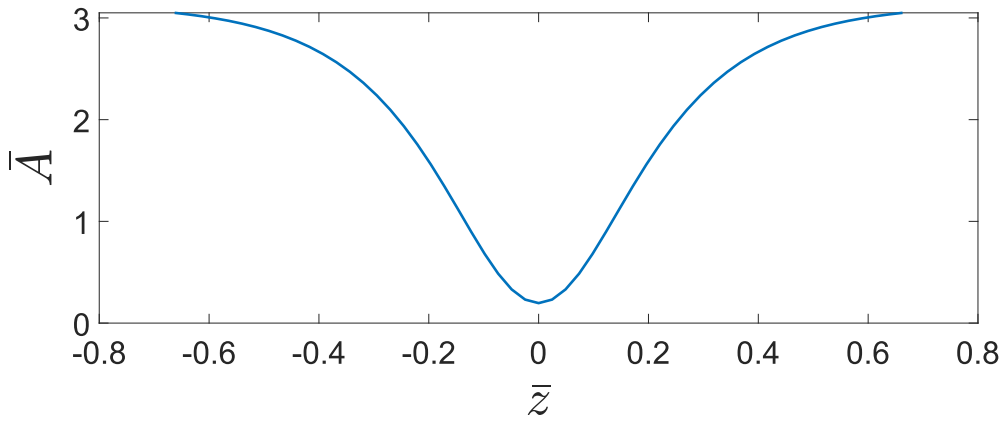

Figure 5.5: The area function used in the numerical calculation. The area near $\bar{z} = 0$ has been reduced significantly to trigger the evacuation instability.

e-folding time is chosen to be 1000, so that the area is essentially constant on the time scale of the evacuation instability. The dimensionless parameters $\bar{I}$, $\bar{T_e}$, and $\bar{m_i}$ are chosen to be 0.7, 1, and 70000 respectively to match the conditions in the plasma jet experiment. For the initial condition, we use an initially uniform density profile $\bar{n}_j^0 = 1$ and an initially stationary ion velocity profile $\bar{u}_{i,j}^0 = 0$.

Figure 5.6 shows the numerically calculated $|\bar{u}_e|$ and $\bar{n}$ around $\bar{z} = 0$ at different times. These numerical results agree with the apparent profiles illustrated in Figure 5.2(b) and (c) qualitatively. In Figure 5.6(a), the absolute value of $\bar{u}_e$ peaks at $\bar{z} = 0$ due to the constriction of the plasma jet. $|\bar{u}_e|$ then grows rapidly due to the evacuation instability. In order to conserve the current $\bar{I}$, a density dip starts developing as shown in Figure 5.6(b). As time increases, the density dip becomes deeper and deeper. This density dip is consistent with the dimming of visible light observed in the plasma jet experiment. In Figure 5.7, we compare the numerical growth of $|\bar{u}_e|$ to the exponential growth obtained from linear theory. The blue line represents the numerically calculated $\Delta|\bar{u}_e|$ indicated in Figure 5.6, and the red line is an exponential function that grows with a normalized growth rate calculated from Equation (5.30) using initial parameters from the numerical calculation . The numerical solution agrees well with the linear theory until $\bar{t} = 2.5$. After $\bar{t} = 2.5$, the numerical solution starts to grow faster than the growth obtained from linear theory.

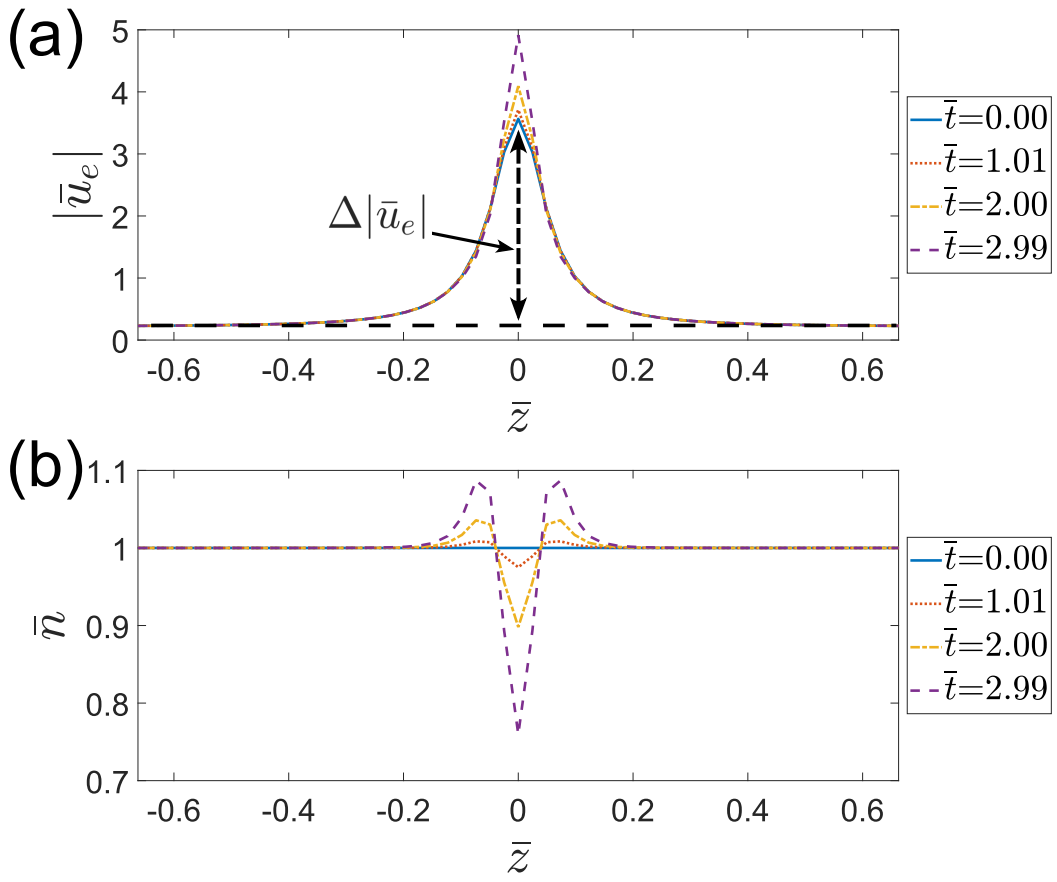

Figure 5.6: The numerically calculated (a) electron drift velocity and (b) density at different times around $\bar{z} = 0$. The electron drift velocity becomes faster and the density dip becomes deeper due to the evacuation instability triggered by the constriction of the plasma jet cross section. $\Delta|\bar{u}_e|$ in (a) denotes the change in electron drift velocity. Figure 5.7 shows how $\Delta|\bar{u}_e|$ grows exponentially with time due to the evacuation instability.

5.5 Discussion

Connection to the Two-Stream Instability

The growth rate γ of the evacuation instability is related to a very low-frequency approximate solution to the classic dispersion for the two-stream instability [78, 24]

$$1 - \frac{\omega_{pi}^2}{\omega^2} - \frac{\omega_{pe}^2}{(\omega - k_z u_{e0})^2} = 0, \tag{5.41}$$

where ω is the (complex) frequency of the two-stream instability and $u_{e0} \gg v_{Te}$ is implied since there is no mention of v_{Te}. To obtain the approximate low-frequency solution, ω_{pi}^2/ω^2 and $\omega_{pe}^2/(\omega - k_z u_{e0})^2$ are assumed to be much greater than 1 so that the 1 in Equation (5.41) can be ignored; this corresponds to assuming quasi-

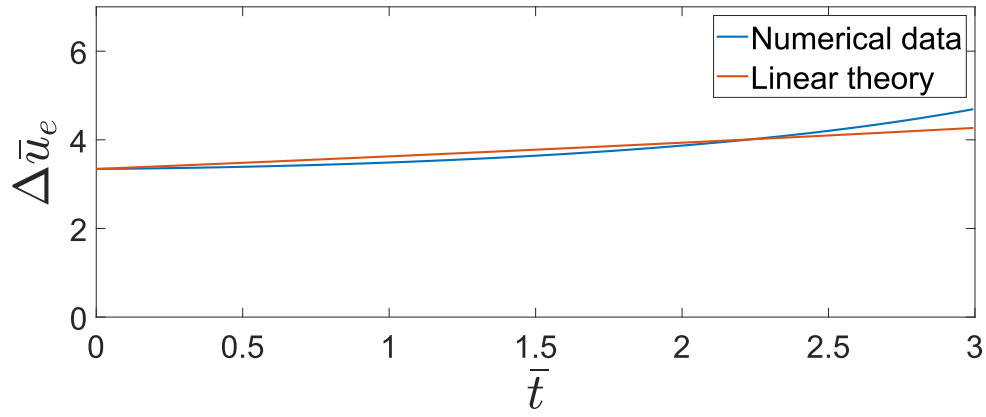

Figure 5.7: The change in electron drift velocity $\bar{z} = 0$ as a function of time is plotted in blue. The red line is the exponential function $3.6e^{0.082\bar{t}}$, where the 0.082 in the exponent is the normalized growth rate calculated from Equation 5.30. This normalized growth rate corresponds to a dimensioned growth rate of approximately 5×10^6 s^{-1}.

neutrality. In addition, ω in the denominator of the electron term in Equation (5.41) is neglected compared to $k_z u_{e0}$. The resulting simplified dispersion

$$\frac{\omega_{pi}^2}{\omega^2} + \frac{\omega_{pe}^2}{k_z^2 u_{e0}^2} = 0 \tag{5.42}$$

has a positive (unstable) imaginary solution $\omega = \mathrm{i} k_z u_{e0} \sqrt{m_e/m_i}$, which is similar to γ if v_{Te} is ignored in Equation (5.30).

However, there is a large difference between the evacuation instability derived here and the classic two-stream instability. The classic two-stream instability ignores collisions, and many studies have argued that including collisions would suppress the growth rate of the instability [26, 27, 28, 29, 30]. Contrarily, the derivation of the evacuation instability shows that the existence of the instability, i.e., its threshold and growth rate, is indifferent to collisions since the momentum lost by electrons as a result of collisions equals the momentum gained by ions as demonstrated here in adding Equations (5.19) and (5.20) to obtain Equation (5.21).

The evacuation instability's indifference to collisions might have a connection to a new kinetic theory [98], recently studied by Tigik, Ziebell, and Yoon, on collisional damping rates for plasma waves because this kinetic theory has predicted damping rates that are significantly weaker than those according to the traditional theory. However, the situation considered by Tigik, Ziebell, and Yoon has no initial electron

drift velocity, i.e., $u_{e0} = 0$ while the situation considered in this paper has a finite u_{e0}. More studies are needed to understand the effect of finite u_{e0} on the collisional damping rates calculated from the newly developed kinetic theory.

Difference from the Ion-Acoustic Instability

The ion-acoustic instability is a well-known instability that can be excited in a current-carrying plasma if the electron drift velocity u_{e0} relative to ions is faster than the ion-acoustic velocity $c_s = \sqrt{\kappa T_e/m_i}$. Readers who are familiar with this instability may recall that the standard expression for the ion-acoustic instability growth rate is roughly

$$\gamma_a \approx \frac{\pi^{1/2}}{2\sqrt{2}} k_z \left(u_{e0} - c_s\right) \sqrt{\frac{m_e}{m_i}}, \tag{5.43}$$

in the limit that $k_z\lambda_{De} \ll 1$ and $T_e \gg T_i$ [99].

The expression in Equation (5.43) is obtained by solving the equation $\epsilon(\omega) = 0$, where $\epsilon(\omega)$ is the plasma dielectric function, for the complex frequency $\omega = \omega_r + \mathrm{i}\gamma_a$ in the limit that $\gamma_a \ll \omega_r$, $|\omega/k_z| \gg v_{Ti}$, and $|\omega/k_z - u_{e0}| \ll v_{Te}$ [100]:

$$\epsilon(\omega) = 1 - \frac{\omega_{pi}^2}{\omega^2} + \frac{1}{k_z^2\lambda_{De}^2} + \mathrm{i}\frac{\pi^{1/2}}{\sqrt{2}k_z^2\lambda_{De}^2}\left[\frac{\omega - k_z u_{e0}}{k_z v_{Te}} + \frac{\omega}{k_z v_{Ti}}\frac{T_e}{T_i}\exp\left(-\frac{\omega^2}{2k_z^2 v_{Ti}^2}\right)\right] = 0. \tag{5.44}$$

The standard procedure to solve Equation (5.44) is to first split the equation into a part that does not explicitly depend on the imaginary unit i and a part that depends on i explicitly:

$$\epsilon(\omega_r + \mathrm{i}\gamma_a) = \epsilon_r(\omega_r + \mathrm{i}\gamma_a) + \mathrm{i}\epsilon_i(\omega_r + \mathrm{i}\gamma_a) = 0, \tag{5.45}$$

where

$$\epsilon_r(\omega) = 1 - \frac{\omega_{pi}^2}{\omega^2} + \frac{1}{k_z^2\lambda_{De}^2} \tag{5.46}$$

and

$$\epsilon_i(\omega) = \frac{\pi^{1/2}}{\sqrt{2}k_z^2\lambda_{De}^2}\left[\frac{\omega - k_z u_{e0}}{k_z v_{Te}} + \frac{\omega}{k_z v_{Ti}}\frac{T_e}{T_i}\exp\left(-\frac{\omega^2}{2k_z^2 v_{Ti}^2}\right)\right]. \tag{5.47}$$

Because $\gamma_a \ll \omega_r$ is assumed, Equation (5.45) can be Taylor expanded around $\omega = \omega_r$ as

$$\epsilon_r(\omega_r) + \mathrm{i}\gamma_a\left(\frac{\mathrm{d}\epsilon_r}{\mathrm{d}\omega}\right)_{\omega=\omega_r} + \mathrm{i}\epsilon_i(\omega_r) \approx 0. \tag{5.48}$$

The real part of Equation (5.48) can be readily solved for ω_r:

$$\omega_r = \frac{k_z c_s}{\sqrt{1 + k_z^2 \lambda_{De}^2}}. \tag{5.49}$$

In the limit that $k_z \lambda_{De} \ll 1$, $\omega_r \approx k_z c_s$.

The imaginary part of Equation (5.48) can be used to calculate γ_a:

$$\gamma_a = -\frac{\epsilon_i(\omega)}{\frac{\mathrm{d}\epsilon_r}{\mathrm{d}\omega}}\bigg|_{\omega=\omega_r} = -\frac{k_z^3 c_s^3}{2\omega_{pi}^2}\epsilon_i(k_z c_s). \tag{5.50}$$

In the limit that $T_e \gg T_i$, the exponential term in Equation (5.47) can be dropped, so Equation (5.50) simplifies to the expression in Equation (5.43).

If $u_{e0} \gg c_s$, then $\gamma_a \approx k_z u_{e0}\sqrt{m_e/m_i}$, which is seemingly similar in expression to the growth rate γ of the evacuation instability (see Equation [5.30]). However, γ_a is assumed to be much smaller than $k_z c_s$ in the calculation that leads to Equation (5.43). In other words, Equation (5.43) is only valid if γ_a is evaluated to be much smaller than $k_z c_s$. This requirement automatically makes γ_a much smaller than γ because $u_{e0} \gg v_{Te}$ is assumed in the derivation that leads to $\gamma \approx k_z u_{e0}\sqrt{m_e/m_i}$, so

$$\gamma \gg k_z v_{Te}\sqrt{m_e/m_i} = k_z c_s \gg \gamma_a. \tag{5.51}$$

5.6 Conclusion

In summary, the collisional two-fluid model presented here extends the well-known two-stream instability to a previously unknown high-collision regime, and this extension predicts an evacuation instability when the current channel cross section is constricted. Applying this model to the Caltech plasma jet experiment demonstrates that electron acceleration, density depletion, and an electric DL associated with localized plasma heating are developed when the plasma jet cross section is constricted by the RT instability. Therefore, the collisional two-fluid model is consistent with the visible light dimming and EUV radiation observed in the Caltech plasma jet experiment. This model is likely applicable to other collisional plasmas, both in nature and in the laboratory, that can develop constricted cross-sections of current channels. Examples include solar prominences and the formation of laboratory spheromaks.

Appendix A

BASIC PLASMA PHYSICS EQUATIONS

This appendix summarizes the key equations of three primary plasma physics models: the Vlasov model, the two-fluid model, and the magnetohydrodynamics (MHD) model. The equations are for a fully ionized plasma.

A.1 The Vlasov-Maxwell Equations

The Vlasov-Maxwell system of equations

$$\frac{\partial f_\sigma}{\partial t} + \mathbf{v} \cdot \frac{\partial f_\sigma}{\partial \mathbf{x}} + \frac{q_\sigma}{m_\sigma}(\mathbf{E} + \mathbf{v} \times \mathbf{B}) \cdot \frac{\partial f_\sigma}{\partial \mathbf{v}} = C_\sigma(f_\sigma) \tag{A.1}$$

$$\nabla \times \mathbf{E} = -\frac{\partial \mathbf{B}}{\partial t} \tag{A.2}$$

$$\nabla \times \mathbf{B} = \mu_0 \mathbf{J} + \mu_0 \varepsilon_0 \frac{\partial \mathbf{E}}{\partial t} \tag{A.3}$$

$$\nabla \cdot \mathbf{B} = 0 \tag{A.4}$$

$$\nabla \cdot \mathbf{E} = \frac{\sum_\sigma n_\sigma q_\sigma}{\varepsilon_0} \tag{A.5}$$

$$n_\sigma = \int f_\sigma \, \mathrm{d}\mathbf{v} \tag{A.6}$$

$$\mathbf{J} = \sum_\sigma n_\sigma q_\sigma \mathbf{u}_\sigma = \sum_\sigma q_\sigma \int \mathbf{v} f_\sigma \, \mathrm{d}\mathbf{v} \tag{A.7}$$

describes the evolution of the distribution function $f_\sigma(\mathbf{x}, \mathbf{v}, t)$ of particle species σ (electron or ion) under the effects of the electric field $\mathbf{E}$, the magnetic field $\mathbf{B}$, and collisions $C_\sigma(f_\sigma)$. The distribution function f_σ measures the number of particles of species σ within a small phase space volume near $(\mathbf{x}, \mathbf{v})$ at time t. The velocity-space integrals of f_σ determine the charge distribution and current density which affect $\mathbf{E}$ and $\mathbf{B}$.

The collision operator $C_\sigma(f_\sigma)$ in Equation (A.2) can be defined by the following

Fokker–Planck equations:

$$C_\sigma(f_\sigma) = \sum_{F=i,e} \frac{q_\sigma^2 q_F^2 \ln\Lambda}{4\pi\varepsilon_0^2 m_\sigma^2} \left[-\frac{\partial}{\partial \mathbf{v}} \cdot \left(f_\sigma \frac{\partial h_{\sigma F}}{\partial \mathbf{v}} \right) + \frac{1}{2} \frac{\partial}{\partial \mathbf{v}} \frac{\partial}{\partial \mathbf{v}} : \left(f_\sigma \frac{\partial^2 g_F}{\partial \mathbf{v} \partial \mathbf{v}} \right) \right] \tag{A.8}$$

$$g_F(\mathbf{v}) = \int |\mathbf{v} - \mathbf{v}'| f_F(\mathbf{v}') \, \mathrm{d}\mathbf{v}' \tag{A.9}$$

$$h_{\sigma F}(\mathbf{v}) = \left(1 + \frac{m_\sigma}{m_F} \right) \int \frac{f_F(\mathbf{v}')}{|\mathbf{v} - \mathbf{v}'|} \, \mathrm{d}\mathbf{v}', \tag{A.10}$$

where $\ln\Lambda$ in Equation (A.8) is the Coulomb logarithm (its value is approximately 10 for practical calculations).

A.2 The Two-Fluid Equations

The two-fluid equations mainly consist of a continuity equation

$$\frac{\partial n_\sigma}{\partial t} + \nabla \cdot (n_\sigma \mathbf{u}_\sigma) = 0 \tag{A.11}$$

and an equation of motion

$$\frac{\partial \mathbf{u}_\sigma}{\partial t} + \mathbf{u}_\sigma \cdot \nabla \mathbf{u}_\sigma = \frac{q_\sigma}{m_\sigma} (\mathbf{E} + \mathbf{u}_\sigma \times \mathbf{B}) - \frac{\nabla \cdot \mathbf{P}_\sigma}{n_\sigma m_\sigma} - \frac{\mathbf{R}_\sigma}{n_\sigma m_\sigma}. \tag{A.12}$$

The pressure tensor in Equation (A.12) is defined by

$$\mathbf{P}_\sigma = m_\sigma \int (\mathbf{v} - \mathbf{u}_\sigma)(\mathbf{v} - \mathbf{u}_\sigma) f_\sigma \, \mathrm{d}\mathbf{v}, \tag{A.13}$$

and the collisional drag force $\mathbf{R}_\sigma$ in Equation (A.12) is defined by

$$\mathbf{R}_\sigma = m_\sigma \int \mathbf{v} C_\sigma(f_\sigma) \, \mathrm{d}\mathbf{v}. \tag{A.14}$$

In particular, $\mathbf{R}_\sigma$ satisfies

$$\sum_\sigma \mathbf{R}_\sigma = 0 \tag{A.15}$$

in order to conserve total momentum of electrons and ions.

The continuity equation is obtained by integrating the Vlasov equation (Equation [A.2]) over the entire velocity space, and the equation of motion is obtained by multiplying the Vlasov equation by $\mathbf{v}$ and then integrating over the entire velocity space.

The two-fluid equations describe the evolution of particle density $n_\sigma(\mathbf{x}, t)$ and particle mean velocity $\mathbf{u}_\sigma(\mathbf{x}, t)$. In this description, a plasma essentially consists of an electron fluid and an ion fluid. These fluids interact via electromagnetic forces, pressure gradients, and collisions.

A.3 MHD equations

Multiplying the fluid continuity Equation (A.11) by m_σ and summing over σ give the MHD continuity equation

$$\frac{\partial \rho}{\partial t} + \nabla \cdot (\rho \mathbf{U}) = 0, \tag{A.16}$$

where the mass density ρ is defined as

$$\rho = \sum_\sigma m_\sigma n_\sigma, \tag{A.17}$$

and the center-of-mass velocity $\mathbf{U}$ is defined as

$$\mathbf{U} = \frac{1}{\rho} \sum_\sigma m_\sigma n_\sigma \mathbf{u}_\sigma. \tag{A.18}$$

Multiplying the Vlasov equation by $\mathbf{v}$ and then integrating over the velocity space, multiplying the resulting equation by m_σ, summing over σ, and assuming charge neutrality, $\sum_\sigma n_\sigma q_\sigma = 0$, give the MHD equation of motion

$$\rho \left(\frac{\partial \mathbf{U}}{\partial t} + \mathbf{U} \cdot \nabla \mathbf{U} \right) = \mathbf{J} \times \mathbf{B} - \nabla \cdot \mathbf{P}^{\mathrm{MHD}}, \tag{A.19}$$

where the MHD pressure tensor is defined as

$$\mathbf{P}^{\mathrm{MHD}} = \sum_\sigma \mathbf{P}_\sigma. \tag{A.20}$$

In the MHD description, a plasma is a single charge-neutral fluid that carries a current. The motion of this current-carrying fluid is driven by a magnetic force ($\mathbf{J} \times \mathbf{B}$ force) and a pressure gradient. The MHD model is the much simpler than the two-fluid model and the Vlasov model but can only describe plasma dynamics on a macroscopic level.

Appendix B

SEMICONDUCTOR PHYSICS RELEVANT TO THE CHARGE-SENSITIVE PREAMPLIFIER CIRCUIT

This appendix discusses some semiconductor physics and transistor circuits necessary for understanding how the PIN-diode-based X-ray sensor works. The charge-sensitive preamplifier (CSP) circuit is explained in detail at the end of this appendix. References for this appendix include *The Art of Electronics* by Horowitz and Hill [101] and a draft for *Analog: Inexact Science, Vibrant Art* by Professor Ali Hajimiri. The latest version of the draft can be downloaded from Caltech Holistic Integrated Circuits (CHIC) Resources Page for personal use.

B.1 PN Junction

A PN junction consists of a p-type semiconductor touching an n-type semiconductor. A p-type semiconductor is doped with a small amount chemical elements that have three valence electrons, such as Boron. P-type dopants are also known as acceptors because they can easily accept an electron to form a covalent bond with an adjacent atom. Once an acceptor accepts an electron, it becomes a negative ion and the original position of the electron becomes positively charged. This positively charged region is referred to as a hole, and it is considered as a free charge carrier that can contribute to a current. In general, considering holes as real particles with positive charge is preferred. On the other hand, n-type semiconductors are doped with a small amount elements that have five valence electrons, such as Phosphorus. The fifth electrons are only loosely bonded, so they can easily get excited to become free electrons. For this reason, the n-type dopants are also known as donors.

Depletion Region

Due to thermal diffusion, the free electrons near the PN interface diffuse from the n-side to the p-side, where the concentration of free electrons is significantly lower. Once there, the free electrons have a large probability to recombine with the large number of holes in the p-type material. As a result of this diffusion of free electrons, a positively charged layer of immobile donors is left behind on the n-side. Similarly, the holes on the p-side of the interface diffuse to the n-side and recombine with free electrons there, leaving behind a negatively charged layer of immobile acceptors

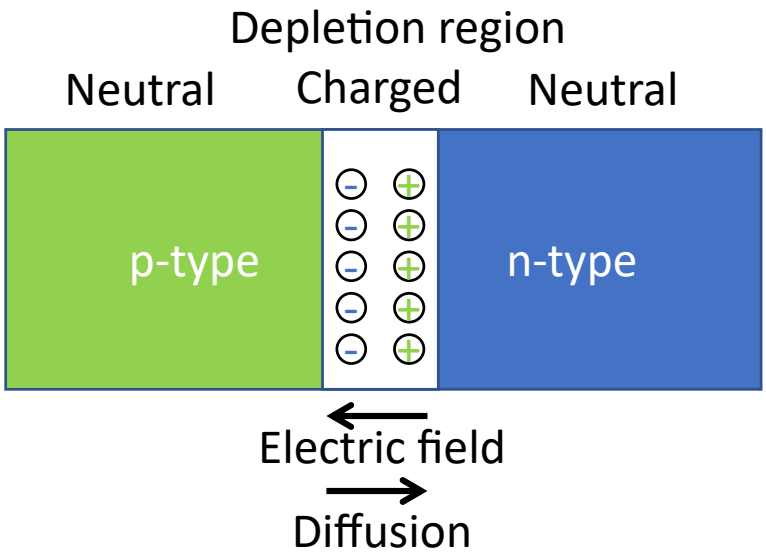

Figure B.1: A PN junction in thermal equilibrium. Due to thermal diffusion of free electrons and holes, oppositely charged layers formed by immobile donors and acceptors develop in the depletion region. These charged layers build up an electric field that balances the thermal diffusion.

on the p-side. This charged region between the p-type material and the n-type material is called the depletion region because free charge carriers are depleted due to recombination (see Figure B.1). An electric field pointing from the positively charged layer on the n-side to the negatively charge layer on the p-side develops. This electric field acts against the thermal diffusion. The width of the depletion region will continue to grow until the electric field balances the thermal diffusion.

The electric field in the depletion region enables the PN junction to be used as a photodetector. When a photon with sufficient energy hits the depletion region, the energy of the photo is absorbed and some electrons and holes are released. For silicon, the conversion efficiency is around 3.6 eV photon energy per electron-hole pair [71, 72]. These electron-hole pairs will be accelerated by the electric field in the depletion region. The movement of these free charge carriers corresponds to a photocurrent that is proportional to the intensity of incident light. By measuring the photocurrent with an external circuit, the intensity of incident light can be determined.

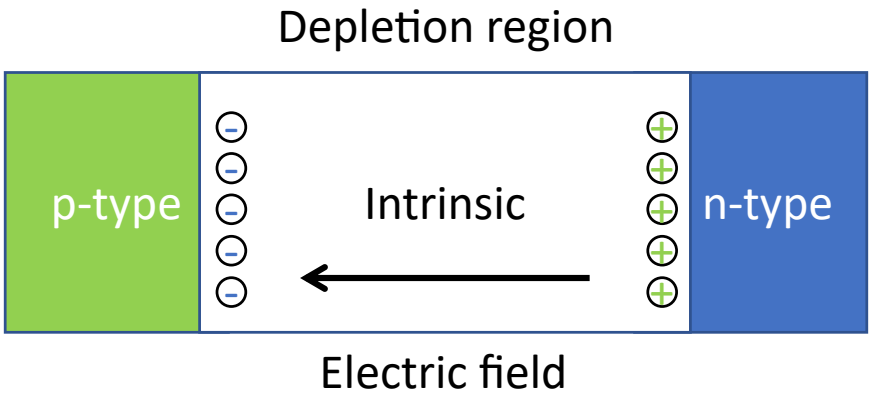

Figure B.2: The intrinsic (undoped) semiconductor effectively widens the depletion region of a PIN diode. This wide depletion region makes the PIN diode an efficient photodetector. Applying a reverse bias voltage can increase the width of the depletion region even more. The intrinsic semiconductor and the charged p-side and n-side boundaries effectively form a parallel plate capacitor.

PIN Diode

The discussion above shows that that the depletion region is important for conversion of light into photocurrent. A PIN diode has an undoped, intrinsic semiconductor between the p-type semiconductor and the n-type semiconductor. This undoped semiconductor effectively increases the width of the depletion region (see Figure B.2). This wide depletion region makes the PIN diode an efficient photodetector. However, a silicon PIN diode is inefficient at absorbing photons with $>$ 30 keV energy [51].

A reverse bias voltage is typically applied across a PIN diode to improve its performance. This reverse bias voltage extends the width of the depletion region to give a even wider photosensitive region. A wider depletion region also lowers the junction capacitance due to the parallel plate capacitor formed by the depletion region and its charged p-side and n-side boundaries. Because this junction capacitance acts as a unwanted low-impedance path for the photocurrent as illustrated in the photodiode equivalent circuit in Figure B.3, decreasing the junction capacitance improves the high-frequency response of a PIN diode.

B.2 Transistors

The CSPs used in the X-ray sensor array consist of discrete transistor circuits made with junction-gate field-effect transistors (JFETs) and bipolar junction transistors

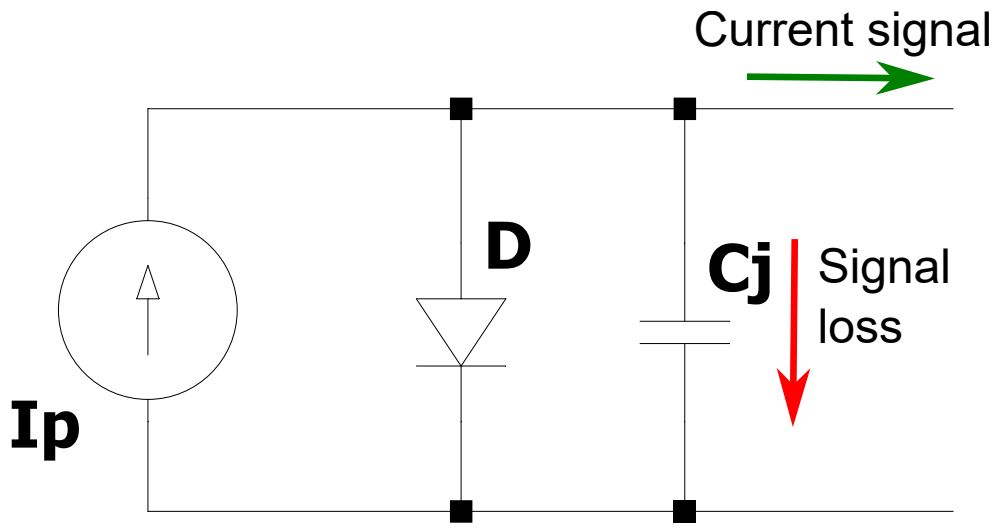

Figure B.3: The equivalent circuit of a PIN diode. The current source I_p represents the photocurrent generated by the PIN diode D. C_j represents the junction capacitance of the PIN diode. A large C_j creates an unwanted low-impedance path for the photocurrent to go through, so lowering this C_j by reverse biasing the PIN diode is desirable.

(BJTs). This section briefly describes how these transistor circuits work.

JFETs

A JFET is a three-terminal device in which the current flow between the source and drain terminals is controlled by a voltage applied to the gate terminal. The current channel between the source and drain terminals can be either an n-type or a p-type semiconductor. We will primarily discuss the n-channel JFETs since this type of JFET is used in the CSP circuit.

In an n-channel JFET, free electrons in the n-channel carry current from drain to source when a positive drain-source voltage V_{DS} is applied across the channel. Figure B.4 illustrates how the current channel of an n-channel JFET is constricted by a depletion region between the p-type semiconductor and the n-channel. Normally, the gate-source PN junction is reverse biased, and the depletion region between the gate and n-channel is wide. This wide depletion region reduces the cross-sectional area of the n-channel and impedes the electric current flow between the drain and source terminals. When gate-source voltage V_{GS} becomes more negative than a critical voltage called the pinch-off voltage V_P, the depletion region completely pinches off the n-channel and the drain-source current I_{DS} decreases to zero. It is worth noting that when the gate-source junction is slightly forward biased, e.g.,

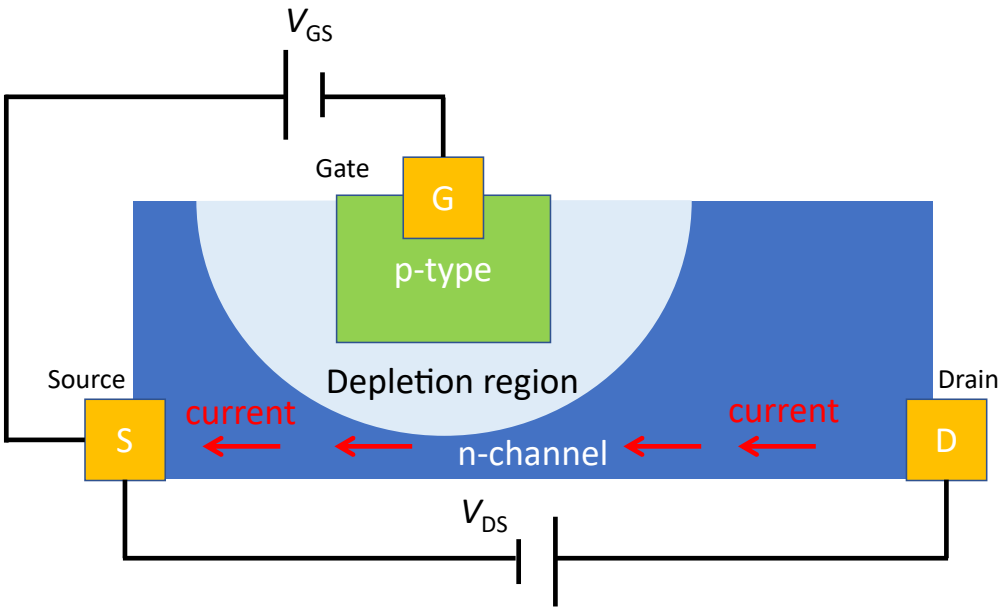

Figure B.4: The current channel of an n-channel JFET is constricted by a depletion region between the gate-source PN junction. This depletion region widens if the gate-source PN junction is reverse biased, and the current flow is impeded.

$V_{GS} \approx 0.2V$, a small current can flow through the gate-source junction.

In the CSP circuit, a feedback capacitor is used to convert the charge carriers generated from the PIN diode to a voltage. After the feedback capacitor is charged to saturation, a discharging path is needed for the CSP to work permanently. Conventionally, this path is provided by a large feedback resistor in parallel with the feedback capacitor. However, a large feedback resistor contributes to unwanted noise, and this noise is typically the main source that limits the signal-to-noise ratio of a CSP [102]. A simple and novel way to discharge the feedback capacitor, as suggested by Bertuccio, Rehak, and Xi [102], is to use a slightly forward biased gate-source junction as shown in Figure B.5. In this circuit, the gate-source junction is forward biased by the leakage current of the reverse biased PIN diode.

The relationships between the I_{DS}, V_{GS}, and V_{DS} of a JFET can be nicely illustrated with the I-V characteristic curves shown in Figure B.6. These curves show that at a given V_{GS} that is greater than the pinch-off voltage V_P, I_{DS} first increases linearly as V_{DS} increases. Once V_{DS} exceeds the saturation voltage V_{SAT}, I_{DS} plateaus despite of V_{DS} increasing. In this saturation region, the value of I_{DS} is determined by V_{GS}, which controls the width of the current channel.

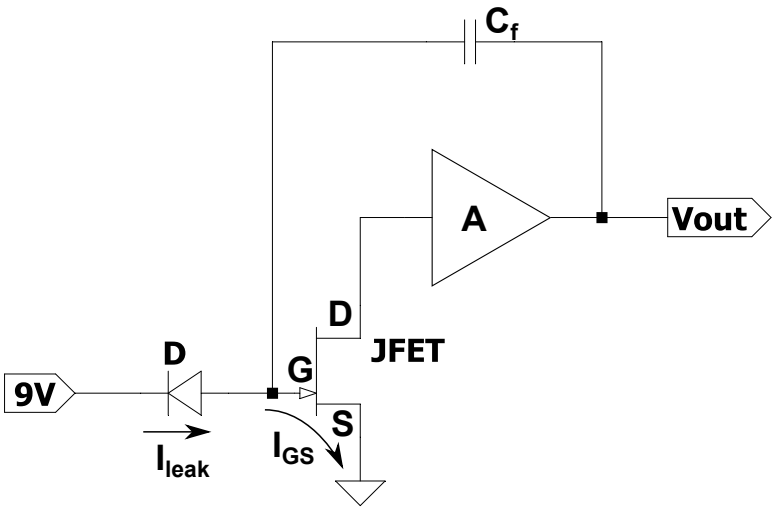

Figure B.5: A simplified charge-sensitive preamplifier circuit without the feedback resistor. The gate-source junction of the JFET is forward biased by the leakage current of the reverse biased PIN diode. This forward biased gate-source junction acts as a discharging path for the feedback capacitor.

Common Source JFET Amplifier

JFETs have very small input current noise because their gate terminals draw little current. This property makes JFETs the ideal transistors for amplifying signals from high-impedance sources, such as a PIN diode. A JFET amplifier operates in the saturation region where I_{DS} is independent of V_{DS}. A JFET amplifier configuration that is used in the CSP circuit is the common source JFET amplifier configuration shown in Figure B.7. The input voltage V_{in} is connected to the gate terminal via a coupling capacitor that separates the input signal from the DC bias source. The output voltage V_{out} is delivered from the drain terminal. V_{out} equals the supply voltage V_+ minus the voltage drop across R_D:

$$V_{out} = V_+ - I_{DS}R_D, \tag{B.1}$$

where I_{DS} is determined by V_{GS} according to Figure B.6. V_{GS} equals the sum of V_{in} and V_{bias}, so a small change in input voltage causes a small change in V_{GS} which modifies I_{DS}. This modification in I_{DS} is then converted to a change in the output voltage by R_D according to Equation (B.1). If R_D is large, then the small change in V_{in} is amplified.

The small-signal gain of the common source JFET amplifier can be derived by

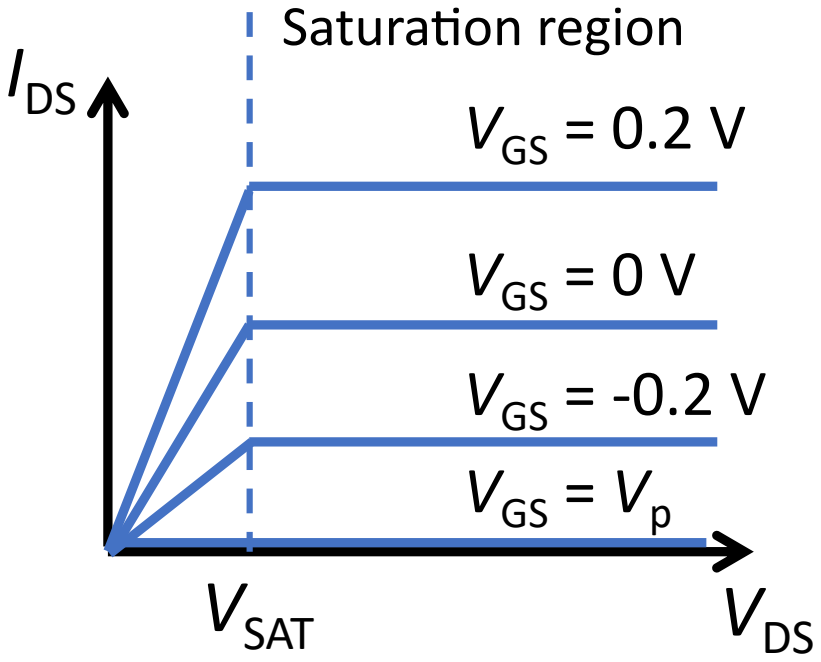

Figure B.6: I-V characteristics of an n-channel JFET. For a given V_{GS} that is greater than the pinch-off voltage V_P, I_{DS} first increases linearly as V_{DS} increases. Once V_{DS} exceeds the saturation voltage V_{SAT}, I_{DS} plateaus despite of V_{DS} increasing. In this saturation region, the value of I_{DS} is determined by V_{GS}, which controls the width of the current channel.

linearizing Equation (B.1) as

$$\frac{\partial V_{out}}{\partial V_{in}} = \frac{\partial V_{out}}{\partial I_{DS}} \frac{\partial I_{DS}}{\partial V_{GS}} \frac{\partial V_{GS}}{\partial V_{in}} = -g_m R_D, \tag{B.2}$$

where

$$g_m = \frac{\partial I_{DS}}{\partial V_{GS}} \tag{B.3}$$

is called the transconductance and

$$\frac{\partial V_{GS}}{\partial V_{in}} = 1. \tag{B.4}$$

An expression for g_m can be derived using the standard JFET model for I_{DS} in the saturation region [101], namely,

$$I_{DS} = I_{DSS} \left(1 - \frac{V_{GS}}{V_P}\right)^2, \tag{B.5}$$

where I_{DSS} is the drain source current when $V_{GS} = 0$. Direct differentiation of Equation (B.5) gives

$$g_m = \frac{\partial I_{DS}}{\partial V_{GS}} = \frac{2\sqrt{I_{DSS}}}{|V_P|} \sqrt{I_{DS}}. \tag{B.6}$$

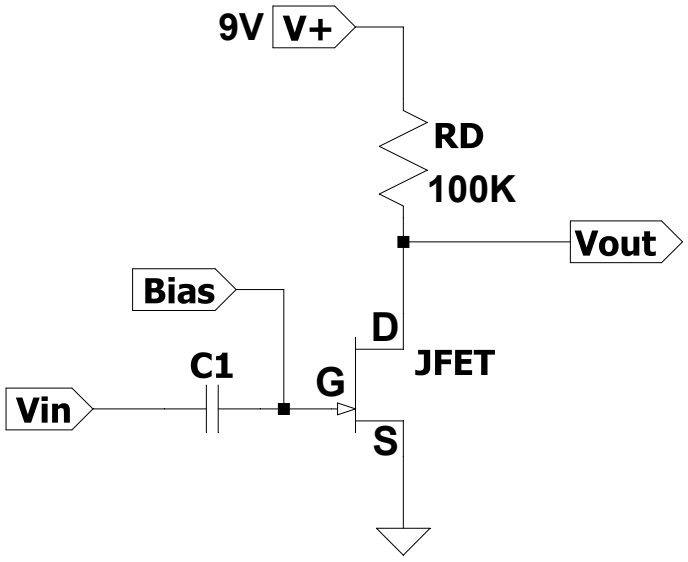

Figure B.7: A common source JFET amplifier circuit. C_1 is a coupling capacitor that separates the AC input voltage from the DC bias source. When the input voltage is zero, the bias source controls V_{GS}, which determines I_{DS} according to Figure B.6. An input voltage modifies V_{GS} which then changes I_{DS}. This change in I_{DS} is then converted to a change in the output voltage by R_D via the formula $V_{out} = V_+ - I_{DS}R_D$.

Thus, the gain of the common source JFET amplifier is proportional to $R_D\sqrt{I_{DS}}$.

BJTs

A BJT is a three-terminal device in which a small current injected into the base terminal controls a much larger current that flows between the collector and emitter terminals. BJTs can be either NPN or PNP types. We will mainly discuss the NPN type transistor here.

In an NPN transistor, a thin p-type layer is sandwiched between two n-type layers. Figure B.8 illustrates different components of current flow in an NPN transistor when it is active. When the base-emitter junction is forward biased, the built-in electric field in the depletion region is weakened, and a current flows from the base to emitter due to thermal diffusion. By design, the emitter is more heavily doped than the base, so the base-emitter current is mainly carried by electrons emitted from the emitter to the base. Once these electrons arrive at the base, they become the minority carrier and start recombining with the holes there. To reduce the chance of recombination, the base layer is designed to be thin, so that, due to thermal motion, most of the electrons will reach the depletion region between the base and the collector without undergoing recombination. The built-in electric field in the

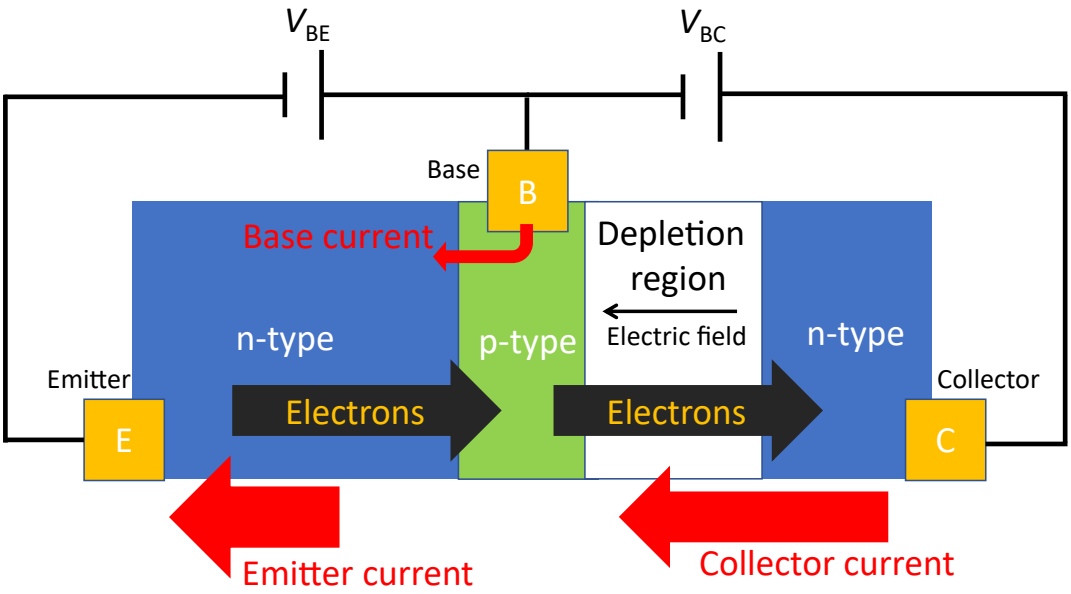

Figure B.8: An NPN transistor with a forward biased base-emitter junction and a reverse biased base-collector junction. The emitter is doped more heavily than the base so that the current across the forward biased base-emitter junction is mainly carried by electrons emitted from the emitter to the base. The base width is designed to be thin, so that most of these current-carrying electrons, with thermal motion, can easily reach the depletion region at the reverse biased base-collector junction without recombining. The built-in electric field in that depletion region accelerates electrons into the collector, where they are the majority carriers and will not recombine.This collector current is that output current that gets delivered to an external circuit.

depletion region accelerates electrons toward the n-type collector where electrons are the majority carrier. This collector current will not be lost due to recombination and can be delivered to an external circuit.

In a way similar to the JFET, I-V characteristic curves in Figure B.9 can nicely illustrate the relationship between the base current I_{B}, the collector current I_{C}, and the collector-emitter voltage V_{CE}. When V_{CE} is large enough to forward bias the NPN transistor into the active region, I_C becomes roughly proportional to I_{B}. This proportionality constant is typically denoted as β. β is typically on the order of 100, but different individual transistors can have large variations in their βs. I_{C} still increases slowly as V_{CE} increases because a larger V_{CE} increases the width of depletion region between the base and the collector, making it easier for electrons in the base to reach the depletion region. This weak dependence of I_{C} on V_{CE} is called the Early effect.

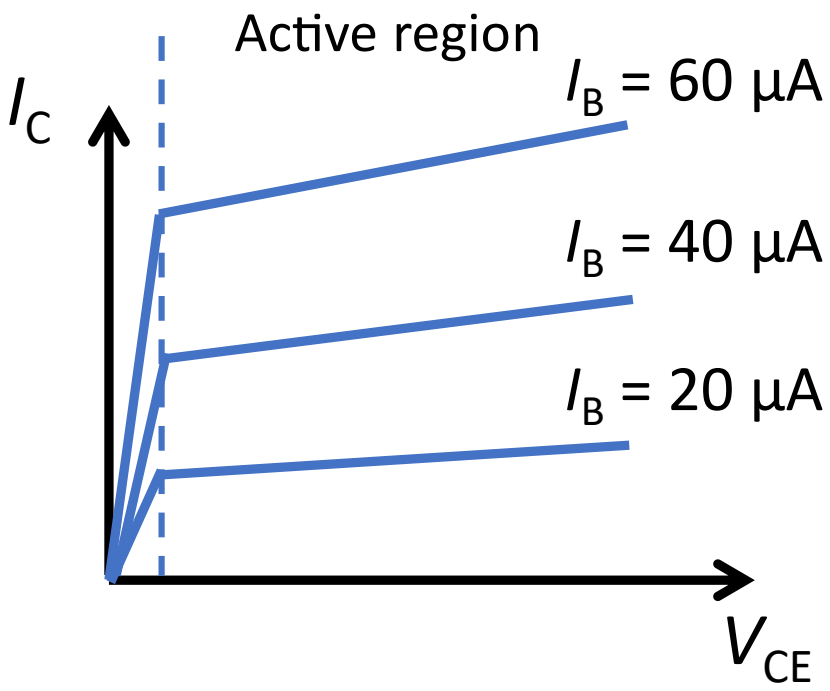

Figure B.9: I-V characteristics of an NPN transistor. For a given base current I_B, the collector current first increases quickly as the collector-emitter voltage V_{CE} increases. Once V_{CE} exceeds a critical voltage such that the collector-base junction is reverse biased, I_C depends weakly on V_{CE}. The small increase in I_C is due to the increase in the width of the depletion region between the base and the collector (this is called the Early effect).

To be precise, it is worth noting that the emitter current I_E is equal to the collector current I_C plus the base current I_B (see Figure B.8). However, in most cases, I_C is several orders of magnitude larger than I_B. Therefore, it is a good approximation to assume that I_C equals the I_E.

Common Emitter BJT Amplifier

Similar to a JFET, an NPN transistor can be used as an amplifier in the common emitter configuration as shown in B.10.

Similar to the common source JFET amplifier, the output voltage is related to the input voltage through the dependence of I_C on V_{in}, which simply differs from V_{BE} by a constant bias voltage:

$$V_{out} = V_+ - I_C(V_{in})R_C. \tag{B.7}$$

The small-signal gain of this amplifier is derived from Equation (B.7) using the

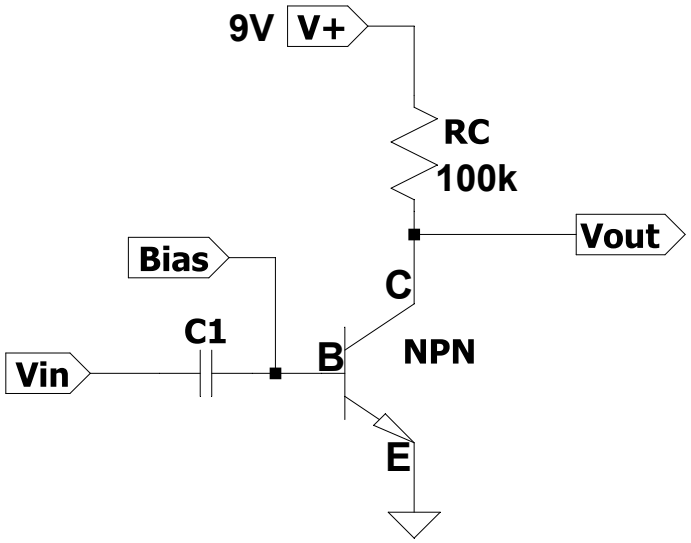

Figure B.10: A common emitter NPN amplifier circuit. C_1 is a coupling capacitor that separates the AC input voltage V_{in} from the DC bias source. When V_{in} is zero, the bias source controls I_{C} via setting I_{B} (Figure B.9 shows how I_{C} depends on I_{B}). An input voltage modifies I_{C} by changing the base current. This modification in I_{C} is then converted to a change in the output voltage by R_{C} via the formula $V_{\text{out}} = V_{+} - I_{\text{C}}R_{\text{C}}$.

chain rule:

$$\frac{\partial V_{\text{out}}}{\partial V_{\text{in}}} = \frac{\partial V_{\text{out}}}{\partial I_{\text{C}}} \frac{\partial I_{\text{C}}}{\partial V_{\text{BE}}} \frac{\partial V_{\text{BE}}}{\partial V_{\text{in}}} = -g_m R_{\text{C}}, \tag{B.8}$$

where, similar to a JFET,

$$g_m = \frac{\partial I_{\text{C}}}{\partial V_{\text{BE}}} \tag{B.9}$$

is called the transconductance and

$$\frac{\partial V_{\text{BE}}}{\partial V_{\text{in}}} = 1. \tag{B.10}$$

When the base-emitter junction is forward biased, the relationship between I_{C} and V_{BE} is roughly [101]

$$I_{\text{C}} = I_{\text{S}} e^{V_{\text{BE}}/V_{\text{T}}}, \tag{B.11}$$

where I_{S} is the saturation current of the PN junction and V_T represents $\kappa T/q_e$, which is a voltage that depends on temperature. Therefore, a simple expression for g_m is

$$g_m = \frac{I_{\text{C}}}{V_{\text{T}}}. \tag{B.12}$$

Assuming V_{T} is roughly constant, g_m is proportional to I_{C}. Thus, the overall linear gain of the common source BJT amplifier is proportional to $R_{\text{C}}I_{\text{C}}$.

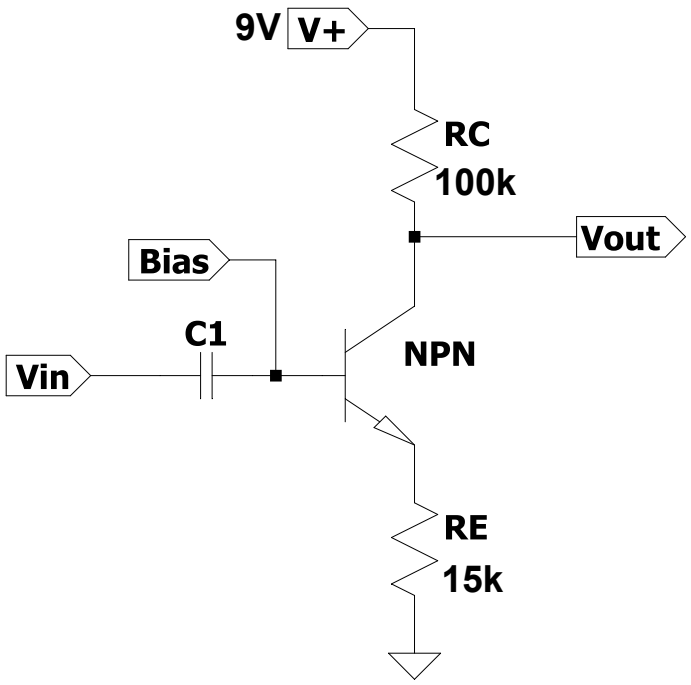

Figure B.11: A common emitter NPN amplifier with emitter degeneration. The large emitter resistor R_E improves the linearity between V_{out} and V_{in} and keeps the base-emitter voltage to be roughly a constant since most of the base voltage will be dropped across the emitter resistor.

Emitter Degeneration

The common emitter amplifier has two problems: (i) it can only function properly for a limited range of input voltages because, for example, a large AC input voltage may reverse bias the base-emitter junction and switch off the transistor; (ii) the output voltage's dependence on the input voltage is highly nonlinear as can be seen from equations (B.7) and (B.11). This non-linearity can lead to distortion of the input signal.

One effective way, as shown in Figure B.11, to mitigate these two problems is to introduce an emitter resister R_E that is much larger than $1/g_m$. This configuration is used in the CSP circuit. The resistance $1/g_m$ is typically denoted as r_m. The value of r_m can be estimated using $r_m = V_T/I_C$. At room temperature, $V_T \approx 25$ mV. I_C is typically between 1 and 10 mA. Therefore, r_m is typically between 2.5 and 25 Ω. If R_E is much larger than r_m, the input voltage will be mostly dropped across R_E. As a result, V_{BE} will stay close to a constant so that the base-emitter junction remains to be properly biased; I_C, which roughly equals the current that flows across R_E, will be mostly proportional to V_{in}, so the linearity of Equation (B.7) is improved. The

gain of this amplifier circuit can be calculated in a way similar to Equation (B.8):

$$\frac{\partial V_{\text{out}}}{\partial V_{\text{in}}} = \frac{\partial V_{\text{out}}}{\partial I_{\text{C}}} \frac{\partial I_{\text{C}}}{\partial V_{\text{BE}}} \frac{\partial V_{\text{BE}}}{\partial V_{\text{in}}} = -g_m R_{\text{C}} \frac{\partial V_{\text{BE}}}{\partial V_{\text{in}}}; \tag{B.13}$$

$\partial V_{\text{BE}}/\partial V_{\text{in}}$ is no longer 1 because V_{in} is also dropped across R_{E}. To get an expression for $\partial V_{\text{BE}}/\partial V_{\text{in}}$, we notice that the base voltage either equals the input voltage plus the bias voltage or V_{BE} plus the voltage drop across R_{E}. Thus,

$$V_{\text{in}} + V_{\text{bias}} = V_{\text{BE}} + I_{\text{C}} R_{\text{E}}. \tag{B.14}$$

Differentiating both sides with respect to V_{in} gives

$$1 = \frac{\partial V_{\text{BE}}}{\partial V_{\text{in}}} + g_m R_{\text{E}} \frac{\partial V_{\text{BE}}}{\partial V_{\text{in}}}, \tag{B.15}$$

which can be solved for $\partial V_{\text{BE}}/\partial V_{\text{in}}$:

$$\frac{\partial V_{\text{BE}}}{\partial V_{\text{in}}} = \frac{1}{1 + g_m R_{\text{E}}}. \tag{B.16}$$

Therefore, the gain of the amplifier with emitter degeneration is

$$\frac{\partial V_{\text{out}}}{\partial V_{\text{in}}} = -\frac{g_m R_{\text{C}}}{1 + g_m R_{\text{E}}} \approx -\frac{R_{\text{C}}}{R_{\text{E}}}, \tag{B.17}$$

where $g_m R_{\text{E}} \gg 1$ has been used to get the approximate expression. This gain expression shows that the gain of the amplifier is approximately determined by the ratio of the collector resistance to the emitter resistance. This desirable property isolates the gain from the characteristics of individual transistors and allows us to control the gain of the amplifier.

Emitter Follower

An emitter follower is a circuit that has a near-unity voltage gain, a high input impedance, and a low output impedance. A typical emitter follower circuit is shown in Figure B.12. The output voltage of this circuit simply equals the input voltage minus V_{BE}. Because V_{BE} depends on I_{C} logarithmically as

$$V_{\text{BE}} = V_{\text{T}} \ln\left(\frac{I_{\text{C}}}{I_{\text{S}}}\right) = V_{\text{T}} \ln\left(\frac{V_{\text{out}}}{R_{\text{E}} I_{\text{S}}}\right), \tag{B.18}$$

V_{BE} is roughly a constant between 0.6 and 0.7 V in most cases.

The usefulness of this circuit relies on its high input impedance and low output impedance: it will not load a high-impedance source and can drive a low-impedance

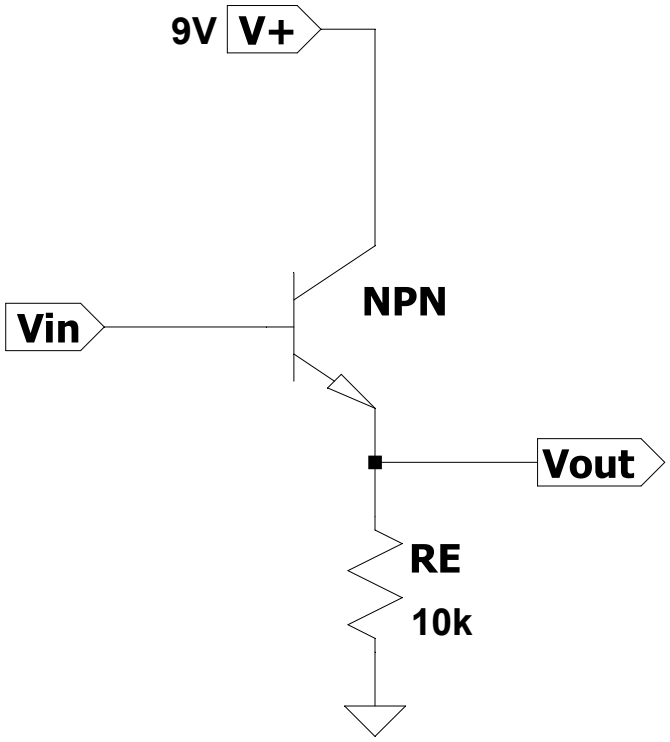

Figure B.12: An emitter follower circuit. The output voltage of this circuit roughly equals the input voltage minus one diode drop (~0.6–0.7 V). This circuit has a high input impedance and a low output impedance.

load. Therefore, it makes an ideal buffer for delivering signal from an amplifier with high output impedance to a standard 50 Ω load. The emitter followers are used in the CSP circuit as buffers to drive the 50 Ω load of a digitizer input channel.

To be clear, the input (or output) impedance of a circuit refers to the input (or output) port's opposition to current flow. It can be found by applying a a small voltage or current perturbation to the port of interest, and finding the ratio of the change in voltage at that port to the change in current flowing into that port.

To see why the input impedance of the emitter follower is high, consider applying a small voltage change ΔV_{in} at the input. This small voltage change will change the base-emitter voltage ΔV_{BE} slightly, so the emitter current will also change accordingly as

$$\Delta I_{\text{E}} = g_m \Delta V_{\text{BE}}. \tag{B.19}$$

This change in emitter current is experienced by the R_{E}, so

$$\Delta I_{\text{E}} = \frac{\Delta V_{\text{E}}}{R_{\text{E}}}. \tag{B.20}$$

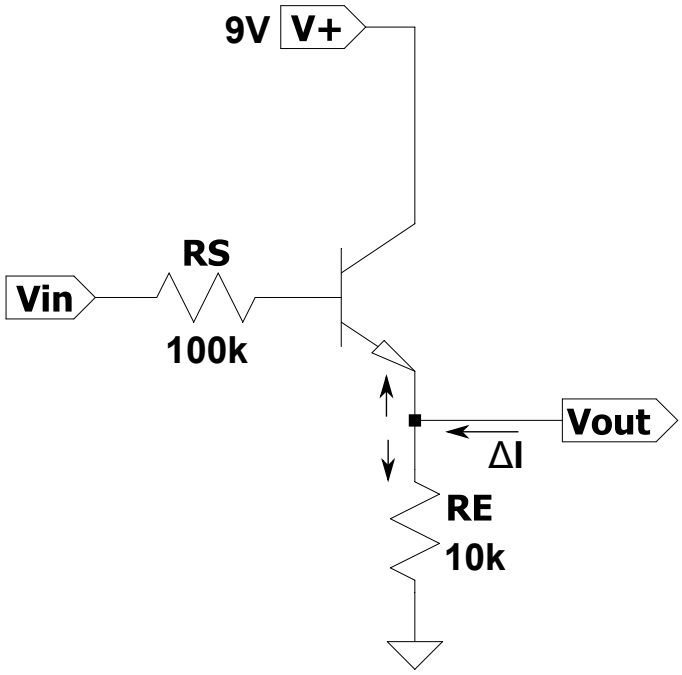

Figure B.13: An emitter follower circuit with source impedance included. The arrows near the output port indicate the directions of small current perturbations for output impedance calculation.

Since $\Delta V_{\mathrm{BE}} = \Delta V_{\mathrm{B}} - \Delta V_{\mathrm{E}}$, we can use equations (B.19) and (B.20) to eliminate ΔV_{E} to get

$$\Delta I_{\mathrm{E}} = \frac{g_m \Delta V_{\mathrm{B}}}{1 + g_m R_{\mathrm{E}}}. \tag{B.21}$$

Reflecting this change in I_{E} back to the input, the change in the input current will be $\Delta I_{\mathrm{in}} = \Delta I_{\mathrm{E}}/\beta$. Therefore, the input impedance of the emitter follower is

$$\frac{\Delta V_{\mathrm{in}}}{\Delta I_{\mathrm{in}}} = \beta \frac{\Delta V_{\mathrm{B}}}{\Delta I_{\mathrm{E}}} = \beta(R_E + r_m), \tag{B.22}$$

where Equation (B.21) has been used to calculate the ratio $\Delta V_{\mathrm{B}}/\Delta I_{\mathrm{E}}$. Equation (B.22) shows that the input impedance of an emitter follower is roughly 100 times greater than R_{E} assuming $R_E \gg r_m$. Typically, R_{E} is between 1 kΩ and 10 kΩ, so the input impedance is typically between 100 kΩ and 1 MΩ.

To calculate the output impedance, we include the source impedance R_{S} as shown in Figure B.13. If we apply a perturbation ΔV_{out} at the output port, the current flowing through R_E to ground will change by $\Delta V_{\mathrm{out}}/R_{\mathrm{E}}$. In addition, the current flowing into the emitter will change too. This current change is roughly β times the change in current flowing from the base to R_{S}, i.e., $\beta \Delta V_{\mathrm{B}}/R_{\mathrm{S}}$. For simplicity, we assume

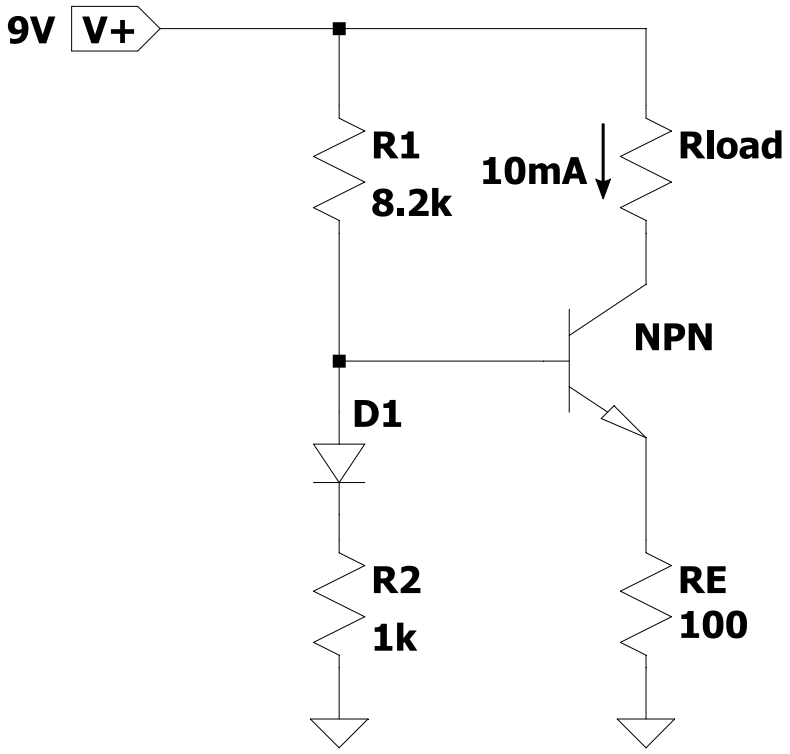

Figure B.14: A transistor current source. The current through R_{load} is always close to 10 mA as long as R_{load} is not too big to cause improper biasing of the transistor. The 10 mA current is determined by the current flowing through R_{E}.

$\Delta V_{\text{B}} \approx \Delta V_{\text{out}}$ because of the unity gain of the follower circuit. Thus, the total change in current flowing into the output port (from V_{out} to the node between the transistor and R_{E}) is $\beta \Delta V_{\text{out}}/R_{\text{S}} + \Delta V_{\text{out}}/R_{\text{E}}$. The output impedance is therefore

$$\frac{\Delta V_{\text{out}}}{\Delta I_{\text{out}}} = \frac{1}{\beta/R_{\text{S}} + 1/R_{\text{E}}} \approx \frac{R_{\text{S}}}{\beta}, \tag{B.23}$$

where the approximation is justified when $R_{\text{S}}/\beta \ll R_{\text{E}}$. This calculation shows that adding one emitter follower as a buffer between a source and a load can effectively reduce the source impedance by a factor of 100. If more reduction is desired, one can simply use an additional emitter follower.

Transistor Current Source

If the base of a transistor is biased to a fixed voltage, the emitter voltage will be roughly constant because the base-emitter voltage V_{BE} does not vary significantly. We can use this transistor property to make a decent current source. Figure B.14 shows a transistor current source that is used in the CSP circuit to provide currents that properly biased other transistors. The current flowing through R_{load} is nearly 10

mA as long as $R_{\text{load}} < 8$ kΩ. A larger R_{load} will drop the collector voltage too low and cause the base-collector junction to be forward-biased. This circuit is a current source because the current through R_{load} is independent of the resistance of R_{load}.

The 10 mA current value is determined like this: the voltage divider formed by R_1, D_1, and R_2 sets the base voltage V_{B}, which sets the emitter voltage V_{E} to be $V_{\text{B}} - V_{\text{BE}}$ Since the voltage drop across diode D_1 compensates the voltage drop across the base-emitter junction, the emitter voltage V_{E} is roughly given by

$$V_{\text{E}} = V_{+}\frac{R_2}{R_1 + R_2} \approx 1V. \tag{B.24}$$

The emitter current I_{E} is therefore $V_{\text{E}}/R_{\text{E}} = 10$ mA, which roughly equals the collector current I_{C} through R_{load}.

B.3 Charge-Sensitive Preamplifier

In this section, we describe the full CSP circuit shown in Figure B.15. The green numbers in the orange boxes are the DC bias voltages measured by a multimeter. Measuring these bias voltages is necessary for verifying that the transistors in the circuit are properly biased. These bias voltages also show the directions of DC currents.

The amplitude of the output voltage of this circuit is proportional to the input charge Q_{in} and inversely proportional to the feedback capacitance C_{f}. The red dots in Figure B.16 show how the amplitude of the output voltage pulse varies as a function of C_{f}. These measurements were done on an early breadboard version of the CSP circuit. The test input charge was simulated by a pulse generator in series with a capacitor. The green crosses in Figure B.16 represent the expected voltage amplitudes that strictly follow the $1/C_{\text{f}}$ scaling. The red dots and green crosses agree with each other until C_{f} becomes smaller 20 pF. The difference between the red dots and green crosses at low feedback capacitance is likely due to the feedback capacitance becoming comparable to the parasitic capacitance. To achieve a large voltage pulse, an unconventional part in the CSP circuit is a < 1 pF feedback capacitor. This small capacitor is made with two 0.059 in $\times$ 0.051 in metal pads separated by 0.025 inches on the printed circuit board (PCB) of the CSP. A photo of the PCB is shown in Figure B.17 for reference. The small feedback capacitor is indicated by a red arrow.

The full CSP circuit is simulated using the AC analysis in LTspice. Figure B.18 shows the overall voltage gain of the simulated CSP circuit as a function of frequency.

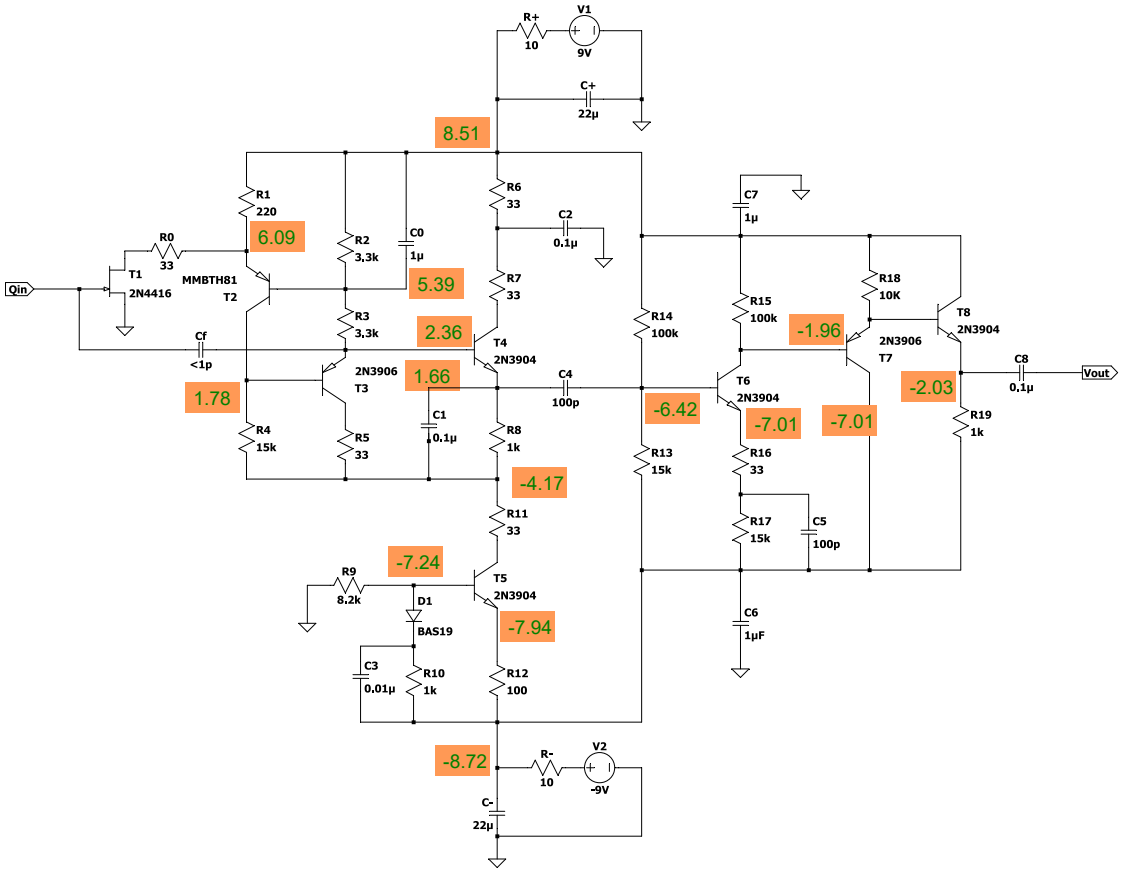

Figure B.15: Full circuit of the charge-sensitive preamplifier. The green numbers in the orange boxes are the DC bias voltages measured by a multimeter. These bias voltages indicate the directions of DC currents and verify that the transistors are properly biased. The output voltage of this circuit is proportional to the input charge Q_{in} and inversely proportional to the feedback capacitance C_{f}. The < 1 pF feedback capacitance is the parasitic capacitance of two small metal pads (the area of each is 0.059 in $\times$ 0.051 in, and the distance between them is 0.025 in) on a printed circuit board.

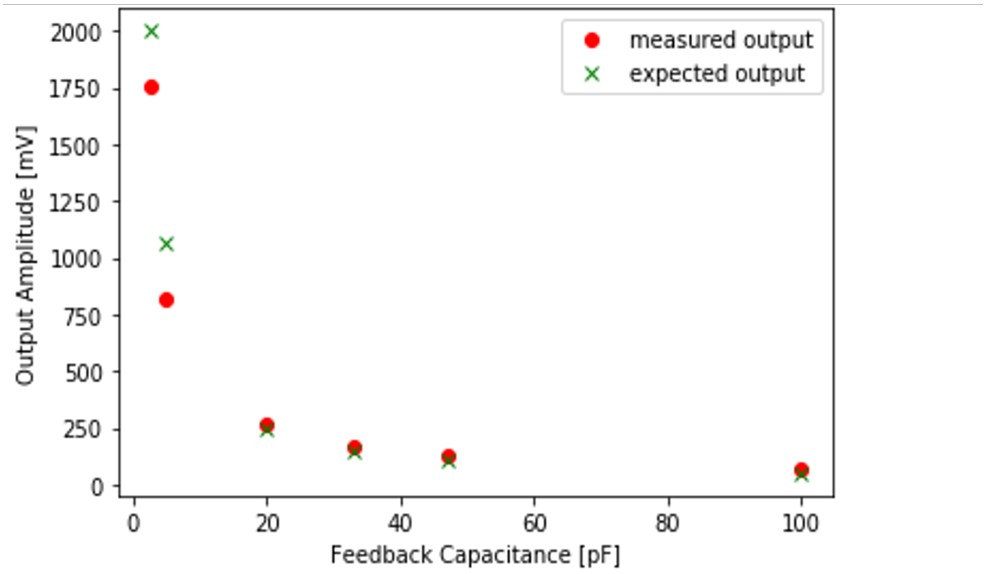

Figure B.16: The red dots show the output voltage amplitudes of an early breadboard version of the charge-sensitive preamplifier circuit with different values of feedback capacitance. The input charge, which was simulated by sending a voltage pulse through a capacitor, is fixed in these measurements. The green crosses represent the expected output voltage amplitude that strictly follows the $1/C_{\mathrm{f}}$ scaling. The difference between the red dots and the green crosses at < 20 pF feedback capacitance is possibly caused by parasitic capacitance on the breadboard.

The simulated voltage gain peaks around 300 kHz. This frequency corresponds to a characteristic time of 3 µs, which is somewhat slower than the 1 µs duration of X-ray emissions in the plasma jet experiment. One can conceivably increase the time resolution of the CSP circuit by modifying the circuit such that the gain peaks at a higher frequency.

First-Stage Cascode Amplifier

The first half of the circuit consisting of T_1–T_5 is adapted from a circuit designed by Bertuccio, Rehak, and Xi [102], and we will describe this part of the circuit in detail in the following paragraphs.

T_1, T_2, and R_4 form a cascode amplifier that amplifies the input signal. T_3 and T_4 form 2 emitter followers that lower the output impedance of the cascode amplifier. T_5 makes a current source that sinks currents from T_2, T_3, and T_4 so that they can be properly biased.

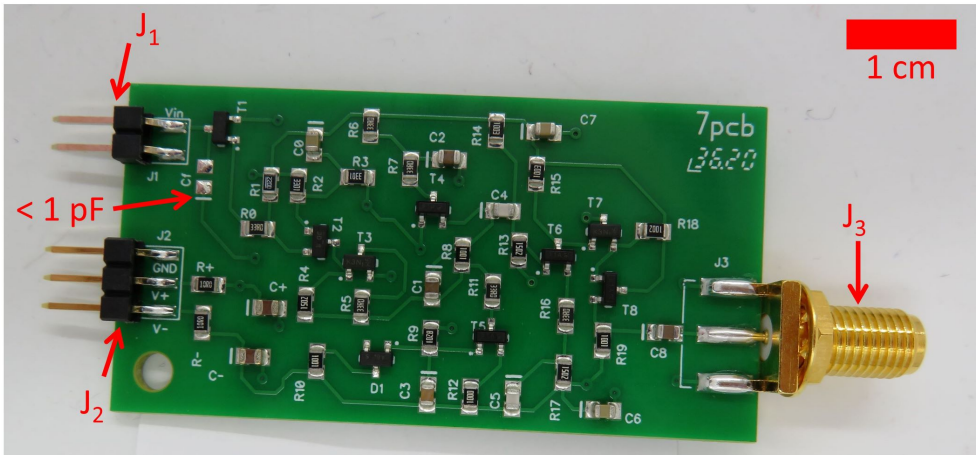

Figure B.17: A photo of the printed circuit board of the charge-sensitive preamplifier. J_1 connector near the top-left corner receives an input signal from a PIN diode. J_3 connector near the bottom-right corner delivers an output signal to the digitizer. Power supplies are connected to the J_2 connector near the bottom-left corner. The metal pads indicated by the red arrow make a < 1 pF feedback capacitor to increase the amplitude of the output voltage pulse.

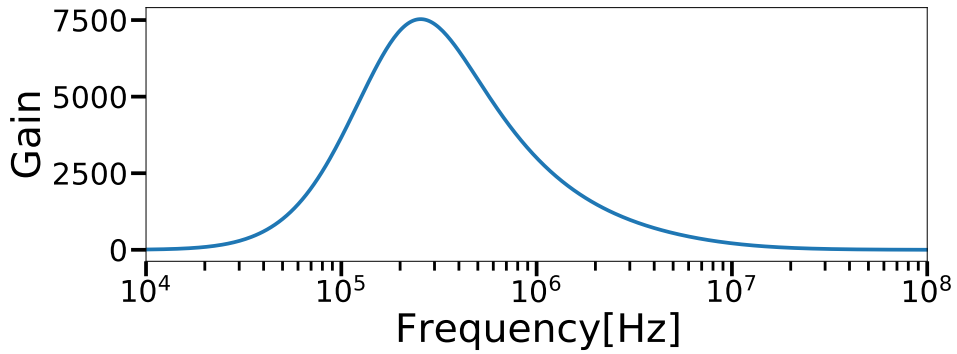

Figure B.18: The voltage gain of the charge-sensitive preamplifier as a function of frequency. This curve is obtained by running a simulation in LTspice. The maximum gain occurs around 300 kHz. Shifting maximum gain to a higher frequency can potentially improve the time resolution of the charge-sensitive preamplifier.

The cascode configuration is similar to the common source configuration, but an extra PNP transistor T_2 is added in between the resistor R_4 and the drain of T_1. Adding this PNP transistor effectively mitigates the Miller effect, which describes an increase in the equivalent input capacitance of an inverting amplifier due to the amplification of (parasitic) capacitance between the input and output terminals. The Miller effect amplification factor is $(1 + A_v)$, where $-A_v < 0$ is the voltage gain of the inverting amplifier [101]. The cascode configuration mitigates the Miller effect by reducing the gain of the inverting amplifier formed by T_1.

The suppression in the gain of T_1 works like this: T_2's base is biased to a fixed voltage by the voltage divider formed by R_2 and R_3. This fixed voltage prevents the emitter voltage of T_2 from changing significantly. Because the drain voltage of T_1 only differs from the emitter voltage of T_2 by a constant voltage drop across R_0, the drain voltage of T_1 will not change significantly either. Since the gain of T_1 in the common source configuration is, by definition, proportional to the change in drain voltage, the gain of T_1 must be small when the drain voltage is prevented from changing significantly.

It is worth noting that the base voltage of T_2 is set to be between the power supply voltage (~ 9 V) and the output voltage of the cascode amplifier by a voltage divider. Because of this base voltage's dependence on the output voltage, the inverting cascode amplifier effectively has a negative feedback loop that lowers the overall gain. Because the bypass capacitor C_0 shorts R_2 at frequency much greater than $1/2\pi R_2 C_0 \approx 50$ Hz, the feedback loop is only effective at frequency lower than 50 Hz. This negative feedback loop prevents the cascode amplifier from amplifying low-frequency fluctuation of the input signal due to, for instance, variation of the PIN diode leakage current, which is sensitive to the reverse bias voltage and the temperature of the PIN diode itself. Since the negative feedback loop is not effective at a frequency much greater than 50 Hz, the gain of the cascode amplifier will be close to its large open-loop gain for transient X-ray signals.

The small gain of this cascode amplifier when the negative feedback loop is active is roughly

$$G_{\text{small}} = -g_m R_1 \left(1 + \frac{R_3}{R_2}\right), \tag{B.25}$$

where g_m is the transconductance of T_1. The large open-loop gain when the feedback loop is inactive is roughly

$$G_{\text{open}} = -g_m R, \tag{B.26}$$

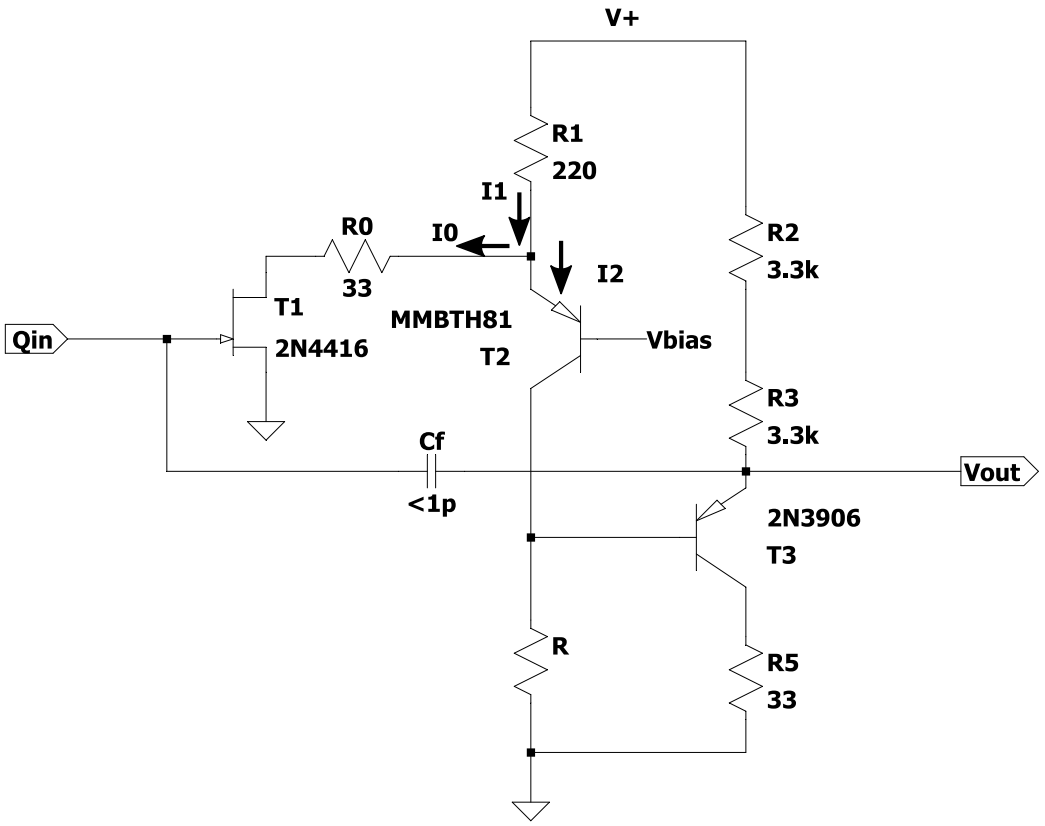

Figure B.19: This circuit shows a simplified first-stage cascode amplifier circuit without the negative feedback loop between V_{out} and T_2. The negative feedback loop is not effective at frequency because of the bypass capacitor C_0 shown in Figure B.15. Without the feedback loop, the amplifier has a voltage gain that is proportional to R in the bottom.

where R is the total equivalent resistance presented at the collector of T_2 and $R \gg R_1(1 + R_3/R_2)$ has been implied so that $G_{\text{open}} \gg G_{\text{small}}$.

Derivations of G_{small} and G_{open}

We now present simple derivations for equations (B.25) and (B.26) for more mathematical readers. Deriving the large open-loop gain is easier: consider the simplified cascode amplifier shown in Figure B.19, where the base of T_2 is fixed by V_{bias}. Applying Kirchhoff's law to the node between R_1, R_0, and T_2, we obtain

$$I_1 = I_0 + I_2. \tag{B.27}$$

The current flowing through R_1 is given by

$$I_1 = \frac{V_+ - V_{\text{E2}}}{R_1}, \tag{B.28}$$

where V_{E2} is the emitter voltage of the transistor T_2. Since the base voltage of T_2 is fixed, the V_{E2} is roughly a constant. As a result, I_1 is roughly independent of V_{in}. Similarly, we can calculate the current flowing through the transistor T_2 as

$$I_2 = \frac{V_{out} - V_{EB3}}{R}, \tag{B.29}$$

where V_{EB3} is the voltage drop across the emitter-base junction of the PNP transistor T_3. Because of the emitter transistors R_2 and R_3, V_{EB3} can be considered as a constant as well. Therefore, I_2 is roughly linear in V_{out}. Given how I_1 and I_2 depend on V_{in}, the derivative of Equation (B.27) with respect to V_{in} is

$$0 = g_m + \frac{1}{R}\frac{\partial V_{out}}{\partial V_{in}}, \tag{B.30}$$

where the transconductance g_m is defined in Equation (B.3). Equation (B.30) can be rearranged to give the large open-loop gain as

$$G_{open} = \frac{\partial V_{out}}{\partial V_{in}} = -g_m R. \tag{B.31}$$

To derive G_{small} when the negative feedback loop is active, we consider a simplified circuit shown in Figure B.20 . The base voltage of T_2 is set by the voltage divider formed by R_2 and R_3 to be

$$V_{B2} = \frac{(V_+ - V_{out})R_3}{R_2 + R_3} + V_{out}. \tag{B.32}$$

Since

$$I_1 = \frac{V_+ - V_{E2}}{R_1} = \frac{V_+ - V_{B2} - V_{EB2}}{R_1}, \tag{B.33}$$

where $V_{EB2} = V_{E2} - V_{B2}$ has been used. Because V_{EB2} is roughly a constant, the derivative of I_1 with respect to V_{in} is roughly

$$\frac{\partial I_1}{\partial V_{in}} = -\frac{1}{R_1}\frac{\partial V_{B2}}{\partial V_{out}}\frac{\partial V_{out}}{\partial V_{in}} = -\frac{1}{R_1}\left(\frac{R_2}{R_2 + R_3}\right)\frac{\partial V_{out}}{\partial V_{in}}, \tag{B.34}$$

where Equation (B.32) has been used to calculate $\partial V_{B2}/\partial V_{out}$. Putting this derivative on the left-hand side of Equation (B.30) gives

$$-\frac{1}{R_1}\left(\frac{R_2}{R_2 + R_3}\right)\frac{\partial V_{out}}{\partial V_{in}} = g_m + \frac{1}{R}\frac{\partial V_{out}}{\partial V_{in}}. \tag{B.35}$$

Since $R \gg R_1(1+R_3/R_2)$, the second term on the right-hand side of Equation (B.35) can be ignored. Thus, the small gain is roughly

$$\frac{\partial V_{out}}{\partial V_{in}} = -g_m R_1\left(1 + \frac{R_3}{R_2}\right). \tag{B.36}$$

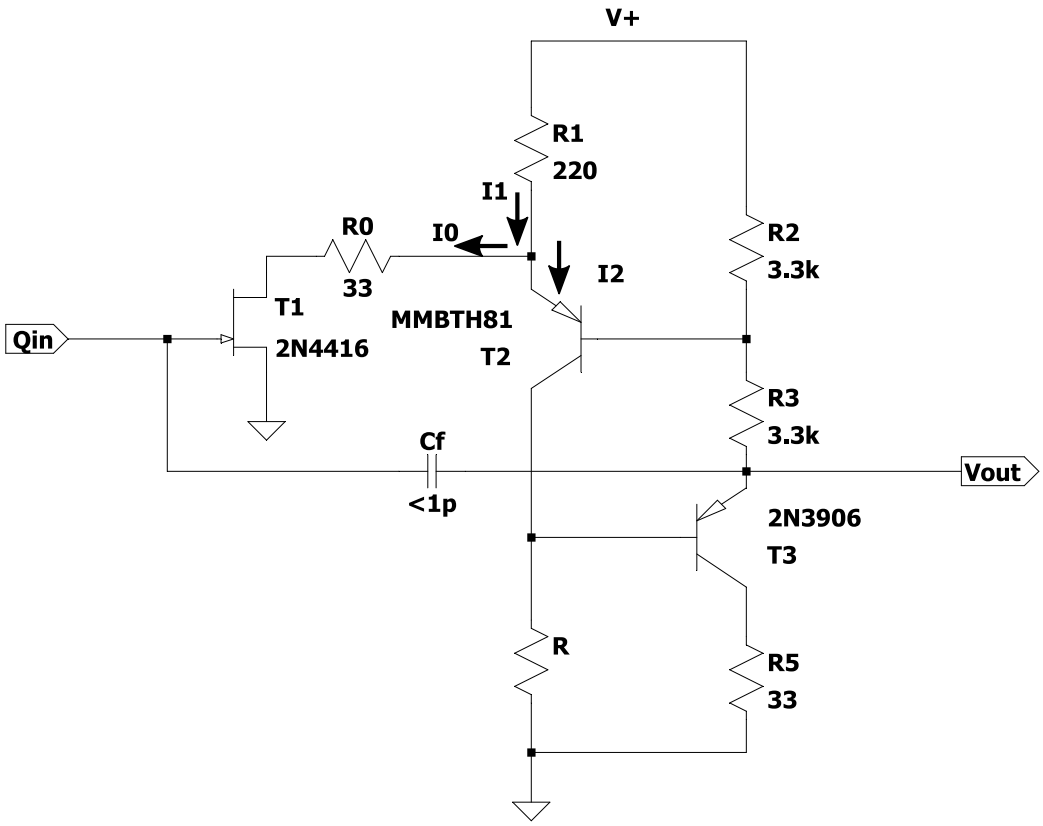

Figure B.20: A cascode amplifier with with a negative feedback loop that suppresses the gain of the amplifier. This cascode amplifier will not amplify low-frequency input fluctuation significantly.

Second-Stage Shaping Amplifier

The second half the circuit formed by T_6, T_7, and T_8 is a second-stage shaping amplifier. This amplifier is AC coupled to the first-stage cascode amplifier to further amplify the voltage signal and reshape the signal to a fast voltage pulse with a width that is < 1 μs. For the convenience of referencing, we show the second half of the CSP circuit alone in Figure B.21. T_6 makes an common emitter amplifier with emitter degeneration. T_7 and T_8 form two emitter followers that lower the output impedance of the CSP circuit, so the CSP circuit can drive a 50 Ω load.

We have seen previously that the gain of the common emitter amplifier with emitter degeneration is roughly $-R_{15}/R_{17} \approx 7$. This is only a moderate gain. However, the bypass capacitor C_5 shorts the emitter resistor R_{17} at frequency much greater than $1/2\pi R_{17}C_5 \approx 100$ kHz, so that the gain is much larger than 7 for transient signals that are faster than 100 kHz.

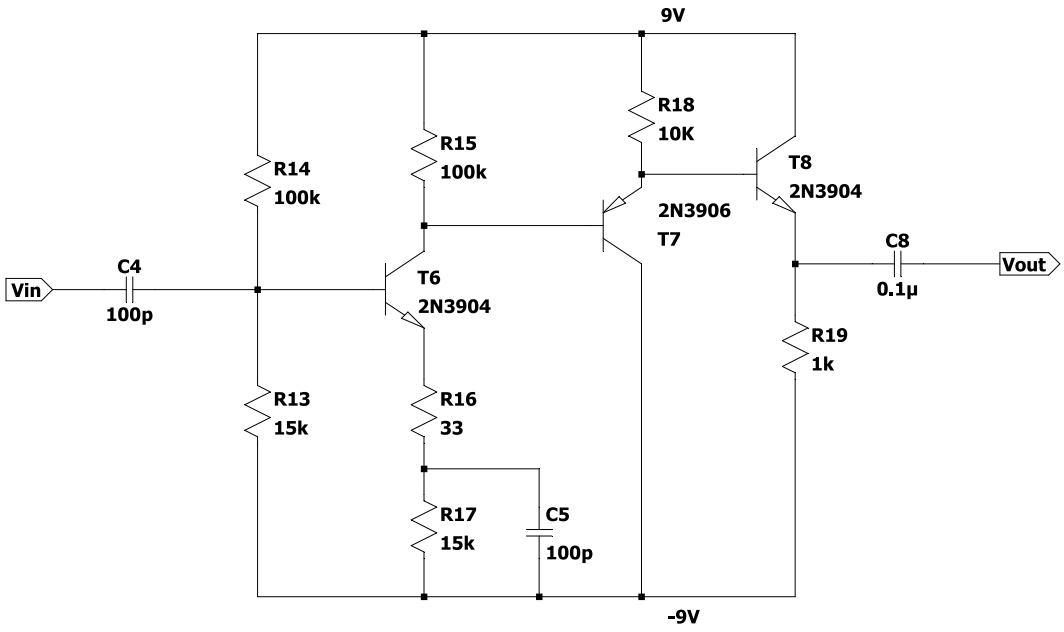

Figure B.21: The second-stage shaping amplifier of the charge-sensitive preamplifier circuit shown in B.15. T_6 is wired up in the common emitter configuration with emitter degeneration. A bypass capacitor C_5 is used to increase the high frequency gain by shorting the emitter resistor R_{17}. T_7 and T_8 form two emitter followers that enable the output to drive a 50 Ω load.

The output capacitor C_8 and the presumable 50 Ω load (not shown in the circuit) form a high-pass RC filter with a 30 kHz cutoff frequency. This filter suppresses output signals that are on a time scale that is much slower than 3×10^{-5}s.

BIBLIOGRAPHY

[1] A. A. Vlasov. “The vibrational properties of an electron gas”. In: *Soviet Physics Uspekhi* 10 (1968), pp. 721–733. DOI: 10.1070/PU1968v010n06ABEH003709.

[2] L. D. Landau. “61–On the vibrations of the electronic plasma”. In: *The Collected Papers of L. D. Landau* (1965), pp. 445–460. URL: http://www-thphys.physics.ox.ac.uk/people/AlexanderSchekochihin/notes/PlasmaClassics/landau_damping.pdf.

[3] O. Buneman. “Dissipation of Currents in Ionized Media”. In: *Physical Review* 115 (1959), pp. 503–517. DOI: 10.1103/PhysRev.115.503.

[4] T. H. Stix. *The theory of plasma waves*. McGraw-Hill, 1962.

[5] H. Alfvén. “Existence of electromagnetic-hydrodynamic waves”. In: *Nature* 150 (1942), pp. 405–406. DOI: 10.1038/150405d0.

[6] L. Woltjer. “A theorem on force-free magnetic fields”. In: *Proceedings of the National Academy of Sciences* 44 (1958), pp. 489–491. DOI: 10.1073/pnas.44.6.489.

[7] J. B. Taylor. “Relaxation of Toroidal Plasma and Generation of Reverse Magnetic Fields”. In: *Physics Review Letters* 33 (1974), pp. 1139–1141. DOI: 10.1103/PhysRevLett.33.1139.

[8] T. R. Jarboe. “Review of spheromak research”. In: *Plasma Physics and Controlled Fusion* 36 (1994), pp. 945–990. DOI: 10.1088/0741-3335/36/6/002.

[9] P. M. Bellan. *Spheromaks: a practical application of magnetohydrodynamic dynamos and plasma self-organization*. Imperial College Press, 2000.

[10] R. S. Marshall and P. M. Bellan. “Acceleration of charged particles to extremely large energies by a sub-Dreicer electric field”. In: *Physics of Plasmas* 26 (2019), p. 042102. DOI: 10.1063/1.5081716.

[11] P. M. Bellan. “Experiments relevant to astrophysical jets”. In: *Journal of Plasma Physics* 84 (2018), p. 755840501. DOI: 10.1017/s002237781800079x.

[12] D. D. Ryutov, R. P. Drake, and B. A. Remington. “Criteria for scaled laboratory simulations of astrophysical MHD phenomena”. In: *The Astrophysical Journal Supplement Series* 127 (2000), pp. 465–468. DOI: 10.1086/313320.

[13] D. D. Ryutov et al. “Magnetohydrodynamic scaling: From astrophysics to the laboratory”. In: *Physics of Plasmas* 8 (2001), pp. 1804–1816. DOI: 10.1063/1.1344562.

[14] S. C. Hsu and P. M. Bellan. "Experimental Identification of the Kink Instability as a Poloidal Flux Amplification Mechanism for Coaxial Gun Spheromak Formation". In: *Physical Review Letters* 90 (2003), p. 215002. DOI: 10.1103/PhysRevLett.90.215002.

[15] A. L. Moser and P. M. Bellan. "Magnetic reconnection from a multiscale instability cascade". In: *Nature* 482 (2012), pp. 379–381. DOI: 10.1038/nature10827.

[16] B. Seo et al. "Determination of a macro-to micro-scale progression leading to a magnetized plasma disruption". In: *Physics of Plasmas* 27.2 (2020), p. 022109. DOI: 10.1063/1.5140348.

[17] Y. D. Yoon and P. M. Bellan. "An intuitive two-fluid picture of spontaneous 2D collisionless magnetic reconnection and whistler wave generation". In: *Physics of Plasmas* 25 (2018), p. 055704. DOI: 10.1063/1.5016345.

[18] R. S. Marshall, M. J. Flynn, and P. M. Bellan. "Hard x-ray bursts observed in association with Rayleigh-Taylor instigated current disruption in a solar-relevant lab experiment". In: *Physics of Plasmas* 25 (2018), p. 112101. DOI: 10.1063/1.5054927.

[19] K. Chai, X. Zhai, and P. M. Bellan. "Extreme ultra-violet burst, particle heating, and whistler wave emission in fast magnetic reconnection induced by kink-driven Rayleigh-Taylor instability". In: *Physics of Plasmas* 23 (2016), p. 032122. DOI: 10.1063/1.4944390.

[20] M. A. Haw, B. Seo, and P. M. Bellan. "Laboratory measurement of large-amplitude whistler pulses generated by fast magnetic reconnection". In: *Geophysical Research Letters* 46 (2019), pp. 7105–7112. DOI: 10.1029/2019GL082621.

[21] P. C. Thonemann et al. "Controlled Release of Thermonuclear Energy: Production of High Temperatures and Nuclear Reactions in a Gas Discharge". In: *Nature* 181 (1958), pp. 217–220. DOI: 10.1038/181217a0.

[22] I. Liodakis et al. "Polarized blazar X-rays imply particle acceleration in shocks". In: *Nature* 611 (2022), pp. 677–681. DOI: 10.1038/s41586-022-05338-0.

[23] S. L. Mandel'Stam. "X-ray emission of the Sun". In: *Space Science Reviews* 4 (1965), pp. 587–665. URL: https://adsabs.harvard.edu/full/1965SSRv....4..587M.

[24] O. Buneman. "Instability, Turbulence, and Conductivity in Current-Carrying Plasma". In: *Physical Review Letters* 1 (1958), pp. 8–9. DOI: 10.1103/PhysRevLett.1.8.

[25] D. Anderson, R. Fedele, and M. Lisak. "A tutorial presentation of the two stream instability and Landau damping". In: *American Journal of Physics* 69 (2001), pp. 1262–1266. DOI: 10.1119/1.1407252.

[26] L. A. Cottrill et al. “Kinetic and collisional effects on the linear evolution of fast ignition relevant beam instabilities”. In: *Physics of Plasmas* 15 (2008), p. 082108. DOI: 10.1063/1.2953816.

[27] H. E. Singhaus. “Beam-Temperature Effects on the Electrostatic Instability for an Electron Beam Penetrating a Plasma”. In: *The Physics of Fluids* 7 (1964), pp. 1534–1540. DOI: 10.1063/1.1711408.

[28] B. Hao et al. “Relativistic collisional current-filamentation instability and two-stream instability in dense plasma”. In: *Physical Review E* 79 (2009), p. 046409. DOI: 10.1103/PhysRevE.79.046409.

[29] S. A. Self, M. M. Shoucri, and F. W. Crawford. “Growth Rates and Stability Limits for Beam-Plasma Interaction”. In: *Journal of Applied Physics* 42 (1971), pp. 704–713. DOI: 10.1063/1.1660084.

[30] D. Sydorenko et al. “Effect of collisions on the two-stream instability in a finite length plasma”. In: *Physics of Plasmas* 23 (2016), p. 122119. DOI: 10.1063/1.4972543.

[31] E. V. Rostomyan. “Influence of electron-ion collisions on Buneman instability in fully ionized plasma”. In: *Physics of Plasmas* 23.10 (2016), p. 102115. DOI: 10.1063/1.4964917.

[32] D. Kumar and P. M. Bellan. “Heterodyne interferometer with unequal path lengths”. In: *Review of Scientific Instruments* 77 (2006), p. 083503. DOI: 10.1063/1.2336769.

[33] B. Seo and P. M. Bellan. “Spatially translatable optical fiber-coupled heterodyne interferometer”. In: *Review of Scientific Instruments* 88 (2017), p. 123504. DOI: 10.1063/1.5007070.

[34] G. S. Yun and P. M. Bellan. “Plasma tubes becoming collimated as a result of magnetohydrodynamic pumping”. In: *Physics of Plasmas* 17 (2010), p. 062108. DOI: 10.1063/1.3437075.

[35] C. A. Romero-Talamás, P. M. Bellan, and S. C. Hsu. “Multielement magnetic probe using commercial chip inductors”. In: *Review of Scientific Instruments* 75 (2004), pp. 2664–2667. DOI: 10.1063/1.1771483.

[36] R. D. Blandford. “Astrophysical jets”. In: *Perspectives in Fluid Mechanics: Proceedings of a Symposium Held on the Occasion of the 70th Birthday of Hans Wolfgang Liepmann Pasadena, California, 10–12 January, 1985*. Springer. 2005, pp. 14–30. DOI: 10.1007/BFb0021115.

[37] R. E. Pudritz, M. J. Hardcastle, and D. C. Gabuzda. “Magnetic Fields in Astrophysical Jets: From Launch to Termination”. In: *Space Science Reviews* 169 (2012), pp. 27–72. DOI: 10.1007/s11214-012-9895-z.

[38] V. S. Beskin. “Magnetohydrodynamic models of astrophysical jets”. In: *Physics-Uspekhi* 53 (2010), pp. 1199–1233. DOI: 10.3367/UFNe.0180.201012b.1241.

[39] H. Li et al. “Modeling the large-scale structures of astrophysical jets in the magnetically dominated limit”. In: *The Astrophysical Journal* 643 (2006), pp. 92–100. DOI: 10.1086/501499.

[40] X. Zhai et al. “Three-dimensional MHD simulation of the Caltech plasma jet experiment: first results”. In: *The Astrophysical Journal* 791 (2014), p. 40. DOI: 10.1088/0004-637X/791/1/40.

[41] S. You, G. S. Yun, and P. M. Bellan. “Dynamic and Stagnating Plasma Flow Leading to Magnetic-Flux-Tube Collimation”. In: *Physical Review Letters* 95 (2005), p. 045002. DOI: 10.1103/PhysRevLett.95.045002.

[42] D. Kumar and P. M. Bellan. “Nonequilibrium Alfvénic Plasma Jets Associated with Spheromak Formation”. In: *Physical Review Letters* 103 (2009), p. 105003. DOI: 10.1103/PhysRevLett.103.105003.

[43] Y. Zhou, S. Pree, and P. M. Bellan. “Imaging suprathermal x-rays from a laboratory plasma jet using PIN-diode-based and scintillator-based 1D pinhole/coded aperture cameras”. In: *Review of Scientific Instruments* 94 (2023), p. 013504. DOI: 10.1063/5.0122760.

[44] A. L. Moser. “Dynamics of Magnetically Driven Plasma Jets: An Instability of an Instability, Gas Cloud Impacts, Shocks, and Other Deformations”. PhD thesis. California Institute of Technology, 2012. DOI: 10.7907/V7P0-AW84.

[45] D. Kumar. “Experimental Investigations of Magnetohydrodynamic Plasma Jets”. PhD thesis. 2009. DOI: 10.7907/ENZ7-QV92.

[46] G. S. Yun. “Dynamics of Plasma Structures Interacting with External and Self-generated Magnetic Fields”. PhD thesis. California Institute of Technology, 2008. DOI: 10.7907/9CMD-C377.

[47] R. S. Marshall. “Developing Plasma Spectroscopy and Imaging Diagnostics to Understand Astrophysically-Relevant Plasma Experiments: Megameters, Femtometers, and Everything in Between”. PhD thesis. California Institute of Technology, 2020. DOI: 10.7907/gfcd-4q50.

[48] K. Chai and P. M. Bellan. “Extreme ultra-violet movie camera for imaging microsecond time scale magnetic reconnection”. In: *Review of Scientific Instruments* 84 (2013), p. 123504. DOI: 10.1063/1.4841915.

[49] M. A. Haw. “Experimental and Numerical Studies of Cavities, Flows, and Waves in Arched Flux Ropes”. PhD thesis. California Institute of Technology, 2018. DOI: 10.7907/3AX5-EN61.

[50] A. Nassalski et al. “Comparative Study of Scintillators for PET/CT Detectors”. In: *IEEE Transactions on Nuclear Science* 54 (2007), pp. 3–10. DOI: 10.1109/TNS.2006.890013.

[51] F. J. Ramírez-Jiménez. “X-Ray Spectroscopy with PIN diodes”. In: *AIP Conference Proceedings*. Vol. 857. American Institute of Physics. 2006, pp. 121–133. DOI: 10.1063/1.2359248.

[52] P. Kirkpatrick and A. V. Baez. “Formation of Optical Images by X-Rays”. In: *Journal of the Optical Society of America* 38 (1948), pp. 766–774. DOI: 10.1364/JOSA.38.000766.

[53] D. B. Sinars et al. “Monochromatic x-ray imaging experiments on the Sandia National Laboratories Z facility (invited)”. In: *Review of Scientific Instruments* 75 (2004), pp. 3672–3677. DOI: 10.1063/1.1779607.

[54] A. V. Baez. “ Fresnel Zone Plate for Optical Image Formation Using Extreme Ultraviolet and Soft X Radiation”. In: *Journal of the Optical Society of America* 51 (1961), pp. 405–412. DOI: 10.1364/JOSA.51.000405.

[55] L. Pina et al. “X-ray imaging with compound refractive lens and microfocus x-ray tube”. In: *Advances in X-Ray/EUV Optics and Components III*. Vol. 7077. SPIE. 2008, 70770H. DOI: 10.1117/12.798306.

[56] L. F. Delgado-Aparicio et al. “Simulation, design, and first test of a multi-energy soft x-ray (SXR) pinhole camera in the Madison Symmetric Torus (MST)”. In: *Review of Scientific Instruments* 89 (2018), 10G116. DOI: 10.1063/1.5038798.

[57] J. S. Hong et al. “Laboratory coded-aperture imaging experiments: radial hole coded masks and depth-sensitive CZT detectors”. In: *Hard X-Ray and Gamma-Ray Detector Physics VI*. Vol. 5540. SPIE. 2004, pp. 63–72. DOI: 10.1117/12.559650.

[58] T. M. Cannon and E. E. Fenimore. “Coded Aperture Imaging: Many Holes Make Light Work”. In: *Optical Engineering* 19 (1980), p. 193283. DOI: 10.1117/12.7972511.

[59] S. Miyamoto. “Hadamard transform X-ray telescope”. In: *Space Science Instrumentation* 3 (1977), pp. 473–481. URL: https://ui.adsabs.harvard.edu/abs/1977SSI.....3..473M/abstract.

[60] R. H. Dicke. “Scatter-Hole Cameras for X-Rays and Gamma Rays”. In: *The Astrophysical Journal* 153 (1968), p. L101. DOI: 10.1086/180230.

[61] M. Haw and P. Bellan. “1D fast coded aperture camera”. In: *Review of Scientific Instruments* 86 (2015), p. 043506. DOI: 10.1063/1.4917345.

[62] E. Del Monte et al. “An X-ray imager based on silicon microstrip detector and coded mask”. In: *Nuclear Instruments and Methods in Physics Research Section A: Accelerators, Spectrometers, Detectors and Associated Equipment* 576 (2007), pp. 191–193. DOI: 10.1016/j.nima.2007.01.150.

[63] N. Gehrels et al. “The *Swift* Gamma-ray Burst Mission”. In: *The Astrophysical Journal* 611 (2004), pp. 1005–1020. DOI: 10.1086/422091.

[64] G. Bélanger et al. “Detection of Hard X-Ray Emission from the Galactic Nuclear Region with *INTEGRAL*”. In: *The Astrophysical Journal* 601 (2004), p. L163. DOI: 10.1086/381738.

[65] O. P. Ivanov et al. “Portable X-ray and gamma-ray imager with coded mask: performance characteristics and methods of image reconstruction”. In: *Nuclear Instruments and Methods in Physics Research Section A: Accelerators, Spectrometers, Detectors and Associated Equipment* 422 (1999), pp. 729–734. DOI: 10.1016/S0168-9002(98)01026-2.

[66] M. Gmar et al. “GAMPIX: A new generation of gamma camera”. In: *Nuclear Instruments and Methods in Physics Research Section A: Accelerators, Spectrometers, Detectors and Associated Equipment* 652 (2011), pp. 638–640. DOI: 10.1016/j.nima.2010.09.003.

[67] M. Antimonov et al. “Large-area Kapton x-ray windows”. In: *Advances in X-Ray/EUV Optics and Components X*. Vol. 9588. International Society for Optics and Photonics. SPIE, 2015, 95880F. DOI: 10.1117/12.2193680.

[68] E. D. Nelson and M. L. Fredman. “Hadamard spectroscopy”. In: *Journal of the Optical Society of America* 60 (1970), pp. 1664–1669. DOI: 10.1364/JOSA.60.001664.

[69] N. J. A. Sloane and M. Harwit. “Masks for Hadamard transform optics, and weighing designs”. In: *Applied Optics* 15 (1976), pp. 107–114. DOI: 10.1364/AO.15.000107.

[70] E. J. Watson. “Primitive Polynomials (Mod2)”. In: *Mathematics of Computation* 16 (1962), pp. 368–369. DOI: 10.1090/S0025-5718-1962-0148256-1.

[71] R. C. Alig and S. Bloom. “Electron-Hole-Pair Creation Energies in Semiconductors”. In: *Physical Review Letters* 35 (1975), pp. 1522–1525. DOI: 10.1103/PhysRevLett.35.1522.

[72] F. Scholze et al. “Determination of the electron–hole pair creation energy for semiconductors from the spectral responsivity of photodiodes”. In: *Nuclear Instruments and Methods in Physics Research Section A: Accelerators, Spectrometers, Detectors and Associated Equipment* 439 (2000), pp. 208–215. DOI: 10.1016/S0168-9002(99)00937-7.

[73] W. H. Richardson. “Bayesian-Based Iterative Method of Image Restoration*”. In: *Journal of the Optical Society of America* 62 (1972), pp. 55–59. DOI: 10.1364/JOSA.62.000055.

[74] L. B. Lucy. “An iterative technique for the rectification of observed distributions”. In: *The astronomical journal* 79 (1974), pp. 745–754. DOI: 10.1086/111605.

[75] B. L. Henke, E. M. Gullikson, and J. C. Davis. “X-ray interactions: Photoabsorption, Scattering, Transmission, and Reflection at E= 50-30,000 eV, Z= 1-92”. In: *Atomic Data and Nuclear Data Tables* 54 (1993), pp. 181–342. DOI: 10.1006/adnd.1993.1013.

[76] G. Hölzer et al. "$K\alpha_{1,2}$ and $K\beta_{1,3}$ x-ray emission lines of the $3d$ transition metals". In: *Physical Review A* 56 (1997), pp. 4554–4568. DOI: 10.1103/PhysRevA.56.4554.

[77] S. Kraft et al. "High resolution x-ray absorption spectroscopy with absolute energy calibration for the determination of absorption edge energies". In: *Review of Scientific Instruments* 67 (1996), pp. 681–687. DOI: 10.1063/1.1146657.

[78] P. Carlqvist. *Double layers and two-stream instability in solar flares*. Tech. rep. TRITA-EPP–73-05. Royal Institute of Technology, 1973. URL: https://inis.iaea.org/collection/NCLCollectionStore/_Public/04/072/4072482.pdf.

[79] L. P. Block. "A double layer review". In: *Astrophysics and Space Science* 55 (1978), pp. 59–83. DOI: 10.1007/BF00642580.

[80] B. H. Quon and A. Y. Wong. "Formation of Potential Double Layers in Plasmas". In: *Physical Review Letters* 37 (1976), pp. 1393–1396. DOI: 10.1103/PhysRevLett.37.1393.

[81] S. Iizuka et al. "Buneman Instability, Pierce Instability, and Double-Layer Formation in a Collisionless Plasma". In: *Physical Review Letters* 43 (1979), pp. 1404–1407. URL: 10.1103/PhysRevLett.43.1404.

[82] R. E. Ergun et al. "Parallel electric fields in the upward current region of the aurora: Indirect and direct observations". In: *Physics of Plasmas* 9 (2002), pp. 3685–3694. DOI: 10.1063/1.1499120.

[83] C. Charles. "A review of recent laboratory double layer experiments". In: *Plasma Sources Science and Technology* 16 (2007), R1. DOI: 10.1088/0963-0252/16/4/R01.

[84] F. S. Mozer et al. "Megavolt Parallel Potentials Arising from Double-Layer Streams in the Earth's Outer Radiation Belt". In: *Physical Review Letters* 111 (2013), p. 235002. DOI: 10.1103/PhysRevLett.111.235002.

[85] H. Alfvén. "Double Layers and Circuits in Astrophysics". In: *IEEE Transactions on Plasma Science* 14 (1986), pp. 779–793. DOI: 10.1109/TPS.1986.4316626.

[86] C. Charles. "Plasmas for spacecraft propulsion". In: *Journal of Physics D: Applied Physics* 42 (2009), p. 163001. DOI: 10.1088/0022-3727/42/16/163001.

[87] Y. Takeda and K. Yamagiwa. "Observations of a Buneman double layer and associated electron heating in a high-voltage straight plasma discharge". In: *Physics of Fluids B: Plasma Physics* 3 (1991), pp. 288–299. DOI: 10.1063/1.859737.

[88] Y. Zhang, S. Pree, and P. M. Bellan. "Generation of laboratory nanoflares from multiple braided plasma loops". In: *Nature Astronomy* (2023), pp. 1–7. DOI: 10.1038/s41550-023-01941-x.

[89] H. Alfvén and P. Carlqvist. "Currents in the solar atmosphere and a theory of solar flares". In: *Solar Physics* 1 (1967), pp. 220–228. DOI: 10.1007/BF00150857.

[90] P. Carlqvist. "On the formation of double layers in plasmas". In: *Cosmic Electrodynamics* 3 (1972), pp. 377–388. URL: https://ui.adsabs.harvard.edu/abs/1972CosEl...3..377C/abstract.

[91] W. A. Newcomb. "Hydromagnetic stability of a diffuse linear pinch". In: *Annals of Physics* 10 (1960), pp. 232–267. DOI: 10.1016/0003-4916(60)90023-3.

[92] H. Dreicer. "Electron and Ion Runaway in a Fully Ionized Gas. I". In: *Physical Review* 115 (1959), pp. 238–249. DOI: 10.1103/PhysRev.115.238.

[93] P. M. Bellan. *Fundamentals of Plasma Physics*. Cambridge University Press, 2008.

[94] D. R. Nicholson. *Introduction to Plasma Theory*. Wiley New York, 1983.

[95] R. Fitzpatrick. *Plasma Physics: An Introduction*. CRC Press, 2015.

[96] A. A. Galeev et al. "The nonlinear theory of the Buneman instability". In: *Soviet Physics-JETP* 54.2 (1981), pp. 306–309. URL: https://ui.adsabs.harvard.edu/abs/1981ZhETF..81..572G/abstract.

[97] S. V. Bulanov and P. V. Sasorov. "Ion acceleration it the nonlinear stage of the Buneman instability". In: *Soviet Journal of Plasma Physics* 12 (1986), pp. 29–31. URL: https://ui.adsabs.harvard.edu/abs/1986FizPl..12...54B/abstract.

[98] S. F. Tigik, L. F. Ziebell, and P. H. Yoon. "Collisional damping rates for plasma waves". In: *Physics of Plasmas* 23 (2016), p. 064504. DOI: 10.1063/1.4953802.

[99] S. Ichimaru. *Basic Principles Of Plasma Physics A Statistical Approach*. W. A. Benjamin, 1973.

[100] Masami Fujiwara, M Raether, and Masaaki Yamada. "Influence of Collisions on the Ion-Acoustic Instability in a Weakly Ionized Plasma". In: *Journal of the Physical Society of Japan* 27.3 (1969), pp. 758–763. URL: https://doi.org/10.1143/JPSJ.27.758.

[101] P. Horowitz and W. Hill. *The art of electronics*. Cambridge: Cambridge University Press.

[102] G. Bertuccio, P. Rehak, and D. Xi. “A novel charge sensitive preamplifier without the feedback resistor”. In: *Nuclear Instruments and Methods in Physics Research Section A: Accelerators, Spectrometers, Detectors and Associated Equipment* 326 (1993), pp. 71–76. DOI: 10.1016/0168-9002(93)90334-E.